



universität
wien

DIPLOMARBEIT

Titel der Diplomarbeit

Development and evaluation of a
proton induced gamma emission (PIGE)-setup at VERA

angestrebter akademischer Grad

Magister der Naturwissenschaften (Mag. rer. nat.)

| | |
|------------------|-------------------------------------|
| Verfasser: | Fabienne Eder |
| Matrikel-Nummer: | 0203153 |
| Studienrichtung: | 411 Physik |
| Betreuer: | Ao. Univ.-Prof. Dr. Harry Friedmann |

Wien, am 22. Nov 2008

Abstract

Proton induced gamma-emission (PIGE) is a non-destructive, isotope-sensitive analytical technique to determine the elemental composition of target samples. The PIGE method is based on the determination of γ -lines from reactions, which depend on the incident proton energy and the isotope of the element in the target.

Generally, PIGE is an ideal complementary technique to proton induced X-ray emission (PIXE) analysis, because it is mainly used to determine light element concentrations not detectable with PIXE.

Therefore, the existing PIXE-ART facility was extended by establishing a PIGE setup. The shielding of the proton induced γ -ray background in construction materials comes out to be difficult. A reduction was possible due to purposeful modifications, especially the mounting of a new collimator system.

It is intended to analyze primarily art objects by investigation of light element concentrations which can be detected well by PIGE. For that purpose calibration lines for fluorine, lithium, aluminum, sodium and boron were determined by use of reference materials.

The present PIGE setup, in combination with a 3 MeV proton beam (proton current in order of some nA), allows to measure the concentrations of F, Li, Al, Na and B in the range of mg per g with uncertainties of 6 - 24 %.

Zusammenfassung

Protonen-induzierte Gamma Emission (PIGE) ermöglicht mit Hilfe eines MeV-Protonenstrahls einen zerstörungsfreien isotoopen-sensitiven Nachweis von chemischen Elementen. Die PIGE-Methode beruht auf der Bestimmung von γ -Emissionslinien in Folge von Kernreaktionen. Diese sind von der Einschussenergie der Protonen und von dem Isotop des Elements in der Probe abhängig.

PIGE wird zur Bestimmung von Konzentrationen leichter Elemente verwendet und ist daher eine ideale Ergänzung zur Protonen-induzierten Röntgen Emissions (PIXE)-Analyse, die vor allem zum Nachweis schwererer Elemente geeignet ist.

Aus diesem Grund wurde der bestehenden PIXE-ART Anlage bei VERA (Vienna Environment Research Accelerator) ein PIGE-Aufbau hinzugefügt. Als besondere Schwierigkeit hat sich die Abschirmung des strahlinduzierten γ -Untergrunds in Konstruktionsmaterialien des Aufbaus erwiesen. Dieser konnte durch gezielte Umbauten, insbesondere durch den Einbau von zusätzlichen Kollimatoren, reduziert werden.

Vor allem in Kunstgegenständen müssen häufig Elementkonzentrationen bestimmt werden, die gut mit PIGE nachzuweisen sind. Mit Hilfe von Referenzmaterialien wurden Kalibriergeraden für die Elemente Fluor, Lithium, Aluminium, Natrium und Bor ermittelt.

Unter Verwendung von 3 MeV Protonen bei einem Strom von einigen nA erlaubt der derzeitige PIGE-Aufbau eine Bestimmung von F, Li, Al, Na und B im Konzentrationsbereich von mg pro g Probenmaterial mit Unsicherheiten von 6 - 24 %.

Contents

| | |
|---|-----------|
| 1. Motivation and Overview | 1 |
| 2. PIGE | 3 |
| 2.1. Ion beam analysis | 3 |
| 2.2. Charged particles in matter | 3 |
| 2.3. Electromagnetic radiation in matter | 4 |
| 2.4. Methods of analysis with accelerated proton beams | 9 |
| 2.5. Principle of PIGE | 9 |
| 2.6. PIGE method: detection and limitation | 10 |
| 3. Experimental Setup | 13 |
| 3.1. PIGE facility at the VERA laboratory | 13 |
| 3.2. PIGE setup | 15 |
| 4. Background | 19 |
| 4.1. Natural background | 19 |
| 4.2. Influence of the PIXE-ART modification on the proton induced back- ground | 22 |
| 4.2.1. Primary proton induced background | 22 |
| 4.2.2. PIXE-ART modification | 26 |
| 4.2.3. Present proton induced background | 27 |
| 5. Measurements | 33 |
| 5.1. Experimental conditions | 33 |
| 5.1.1. Current measurement | 33 |
| 5.1.2. Samples | 35 |
| 5.1.3. Detector efficiency | 37 |
| 5.2. Experimental realization | 42 |
| 5.2.1. Energy calibration | 44 |
| 5.2.2. PIGE spectra | 45 |
| 6. Experimental Results | 51 |
| 6.1. Current calibration and background correction | 51 |
| 6.1.1. Correlation of Ar counts with current in FC L5 | 51 |
| 6.1.2. Background correction | 53 |

| | |
|--|-----------|
| 6.2. Calibration and uncertainties | 62 |
| 6.2.1. Evaluation | 62 |
| 6.2.2. Sodium | 64 |
| 6.2.3. Aluminum | 66 |
| 6.2.4. Fluorine | 69 |
| 6.2.5. Boron | 72 |
| 6.2.6. Lithium | 72 |
| 7. Conclusion and Outlook | 75 |
| Appendix | 77 |
| A. Measurement of an iron standard at FZD | 77 |
| B. Determination of the beam width | 79 |
| C. Chemical composition of standards used for evaluation | 86 |
| D. Natural decay series | 91 |
| Bibliography | 93 |
| Acknowledgments | 95 |
| Curriculum vitae | 97 |
| Lebenslauf | 99 |

List of Tables

| | | |
|------|--|----|
| 2.1. | List of Z and E_γ dependences of photon absorption processes | 6 |
| 2.2. | List of nuclear reactions commonly used in PIGE analysis. | 11 |
| 4.1. | List of natural background γ -lines at VERA. | 20 |
| 4.2. | List of observed proton induced γ -rays of the "old" PIXE-ART setup. | 23 |
| 4.3. | List of absolute thick target γ -ray yields for Al, Si and P. | 23 |
| 4.4. | List of observed proton induced γ -rays of the "new" PIXE-ART setup. | 27 |
| 4.5. | List of observed proton induced γ -rays of the "new" PIXE-ART setup with PIXE-slits. | 30 |
| 5.1. | List of Al, F and Na concentrations of metrological standards. | 35 |
| 5.2. | List of Na concentrations of glass standards from Academy of Fine Arts Vienna. | 36 |
| 5.3. | List of light element-iron-mixture concentrations. | 37 |
| 5.4. | List of relative efficiency data. | 38 |
| 5.5. | List of absolute efficiency data. | 40 |
| 5.6. | List no.1 of irradiated samples used for evaluation. | 42 |
| 5.7. | List no.2 of irradiated samples used for evaluation. | 43 |
| 5.8. | List of energy calibration points. | 44 |
| 5.9. | List of nuclear reactions for ^7Li and ^{19}F commonly used in PIGE analysis. | 49 |
| 6.1. | List of current data and acquired counts of Ar K_α and ^{56}Fe used for dose investigation. | 51 |
| 6.2. | List of summarized data for normalized peak area determination for fluorine. | 58 |
| 6.3. | List of summarized data for normalized peak area determination for aluminum. | 59 |
| 6.4. | List of summarized data for normalized peak area determination for sodium. | 60 |
| 6.5. | List of summarized data for normalized peak area determination for lithium and boron. | 61 |
| 6.6. | List of data used for determination of sodium concentrations in metro- logical standards. | 62 |
| 6.7. | List of data used for determination of sodium concentrations in glass standards. | 64 |

| | |
|---|----|
| 6.8. List of data used for determination of aluminum concentrations in metrological standards. | 67 |
| 6.9. List of data used for determination of aluminum concentrations in glass standards. | 68 |
| 6.10. List of data used for determination of fluorine concentrations in metrological standards. | 69 |
| 6.11. List of data used for determination of fluorine concentrations in LiF-iron-mixtures. | 69 |
| 6.12. List of data used for determination of boron concentrations in boron-iron-mixtures. | 72 |
| 6.13. List of data used for determination of lithium concentrations in LiF-iron-mixtures. | 72 |
| 7.1. Summary of evaluated uncertainties of the calibration curves for light element concentrations. | 75 |
| B.1. List of calculated FWHM of the proton beam. | 79 |
| B.2. List of proton beam width data no.1.a. | 82 |
| B.3. List of proton beam width data no.1.b. | 83 |
| B.4. List of proton beam width data no.2.a. | 84 |
| B.5. List of proton beam width data no.2.b. | 85 |

List of Figures

| | | |
|-------|--|----|
| 2.1. | TRIM simulation for 3 MeV protons in air. | 5 |
| 2.2. | Illustration of the three major quanta-material-interactions. | 6 |
| 2.3. | Illustration of the absorption coefficient in lead as a function of photon energy. | 7 |
| 2.4. | Illustration of the Compton continuum | 8 |
| 3.1. | Schematic layout of the VERA facility | 14 |
| 3.2. | Drawing of the PIXE-ART facility. | 16 |
| 3.3. | Photograph of the present PIXE-ART facility. | 17 |
| 4.1. | Spectrum of the natural background at VERA. | 19 |
| 4.2. | Spectrum of the lead-shielded natural background at VERA. | 21 |
| 4.3. | Spectrum of the proton induced background. | 22 |
| 4.4. | Illustration of the $^{56}\text{Fe}(\text{n},\text{n}\gamma)^{56}\text{Fe}$ cross section as a function of neutron energy. | 24 |
| 4.5. | Illustration of the level scheme of ^{56}Fe | 25 |
| 4.6. | COSY simulation of the new PIXE-ART setup. | 26 |
| 4.7. | Spectrum of the proton induced background before and after the PIXE-ART modification. | 28 |
| 4.8. | Spectrum of the proton induced background with and without PIXE slits. | 29 |
| 4.9. | Spectrum of the proton induced background accumulated in June and August. | 31 |
| 5.1. | Illustration of the PIXE-ART facility at the end of the beamline. | 33 |
| 5.2. | PIXE spectrum of 3 MeV protons in air. | 34 |
| 5.3. | Photograph of a target holder containing pulverized standard material. | 35 |
| 5.4. | Photograph of glass standards from the Academy of Fine Arts Vienna. | 36 |
| 5.5. | Plot of the relative efficiency. | 39 |
| 5.6. | Plot of the absolute efficiency. | 41 |
| 5.7. | Illustration of a linear fit used for energy calibration. | 44 |
| 5.8. | PIGE spectrum for a sample containing sodium. | 45 |
| 5.9. | Detailed illustration of a PIGE spectrum for a sample containing aluminum. | 46 |
| 5.10. | Detailed illustration of a PIGE spectrum for a sample containing boron. | 47 |

| | |
|---|----|
| 5.11. PIGE spectrum for a sample containing lithium and fluorine. | 48 |
| 6.1. Illustration of the correlation between the Ar K_{α} peak area and the current in FC L5. | 52 |
| 6.2. Illustration of the correlation between the ^{56}Fe γ -ray peak area and the current in FC L5. | 52 |
| 6.3. Illustration of the correlation between the ^{23}Na γ -ray peak area and the current in FC L5. | 54 |
| 6.4. Illustration of the fit for background correction for ^{23}Na | 55 |
| 6.5. Illustration of the fit for background correction for ^{19}F | 56 |
| 6.6. Illustration of the fit for background correction for ^{27}Al | 57 |
| 6.7. Illustration of the calibration line for sodium concentrations for metrological samples. | 63 |
| 6.8. Illustration of the calibration line for sodium concentrations in glass standards. | 65 |
| 6.9. Illustration of the calibration line for aluminum concentrations in metrological samples. | 67 |
| 6.10. Illustration of the calibration line for aluminum concentrations in glass samples. | 68 |
| 6.11. Illustration of the calibration line for fluorine concentrations in metrological samples. | 70 |
| 6.12. Illustration of the calibration line for fluorine concentrations in glass samples. | 71 |
| 6.13. Illustration of the calibration line for boron concentrations in boron-iron-mixture. | 73 |
| 6.14. Illustration of the calibration line for lithium concentrations in LiF-iron-mixture. | 74 |
| A.1. Illustration of an iron γ -ray spectrum, accumulated at the IBA facility at FZD. | 78 |
| B.1. Plot of horizontal beam width. | 80 |
| B.2. Plot of vertical beam width. | 81 |
| C.1. Data sheet of chemical composition of glass standards used for evaluation. | 86 |
| C.2. Data sheet of certified composition of fly ash, BCR 038. | 87 |
| C.3. Data sheet of certified composition of natural Moroccan phosphate rock, BCR 032. | 88 |
| C.4. Data sheet of chemical composition of opal glass, NBS 91. | 89 |
| C.5. Data sheet of certified composition of iron ore, EZRM 681. | 90 |
| D.1. Thorium series | 91 |
| D.2. Uranium-Radium series | 91 |
| D.3. Actinium series | 92 |

1. Motivation and Overview

The motivation for this work was to extend the PIXE-ART facility at VERA by establishing a PIGE setup with the intention to detect a number of possible isotopes which can not be seen with PIXE.

Protons with an energy more than the Coulomb barrier can undergo nuclear reactions with the atoms of the sample material. The emitted γ -rays are characteristic for isotopes contained in the target material. Since the PIGE technique is used to determine light element concentrations it is an ideal complementary method to PIXE, which is usually applied to detect heavier elements.

Before any element concentrations can be determined, the natural background as well as the proton induced background has been analyzed. The latter one is produced through nuclear reactions of protons hitting construction material inside the beam-line. This gives rise to the emission of γ -rays which appear in the acquired PIGE spectrum. Therefore, a number of so called "proton on air" spectra without sample were investigated.

Finally, several reference materials with different elemental contents were irradiated and used to deduced calibration lines for light element concentrations.

2. PIGE

Proton induced γ -ray emission (PIGE) is a nondestructive technique for material analysis with ion accelerators.

When charged particles, such as MeV protons, hit matter nuclear reactions can be induced and characteristic γ -radiation is emitted. These γ -rays allow to identify the elemental composition of the sample.

2.1. Ion beam analysis

Accelerator-based ion beam analysis (IBA) using high energy ions is an important method to investigate and analyze various elements in samples. This kind of material analysis is based on the interaction between the accelerated (in the order of MeV) charged particles (H^+ , He^+ , H_2^+) and the bombarded material.

When an ion beam is passing through a sample, different interactions with either the electrons of the shell or the nuclei can take place. These reactions lead to emissions of radiation or particles whose energy is characteristic of the chemical elements contained in the material.

Some ion-matter interactions are discussed in the following.

2.2. Charged particles in matter

Two basic phenomena can occur, when a charged particle is penetrating matter: The ion loses kinetic energy due to the Coulomb interaction with mainly the electrons and the projectile may scatter by the Coulomb field of the nuclei [Golser, 1995],[Steinbauer, 1995].

A classical non-relativistic description is possible for protons with energies (in the range of several MeV) which are typical for PIGE. Electronic stopping is more effective than nuclear stopping for the proton-target material reactions.

The energy loss caused of the proton in the target material is caused mainly by excitation, ionization electronic stopping and (with low projectile velocity) electron capture. This type of energy loss can be calculated with the Bethe-Bloch equation.

2. PIGE

The relevant quantity is the $S(E)$, i.e. the mean energy loss per unit pathlength:

$$S(E) = -\frac{dE_1}{dx} = \frac{4\pi Z_1^2 e^4}{m_e v_1^2 (4\pi\epsilon_0)^2} \cdot Z_2 \cdot \left(\ln \frac{2m_e v_1^2}{I} \right) \quad (2.1)$$

where

Z_1, E_1, v_1 ... atomic number, energy, velocity of the projectile

Z_2 ... atomic number of the target atom

x ... pathlength of the projectile

m_e ... rest mass of the electron

e ... elemental charge

I ... mean excitation potential of the target

Reduction of energy is largely determined by v_1^{-2} term of the Bethe-Bloch formula. The energy loss as a function of penetration depth in a sample is called Bragg curve. For protons, this curve follows an almost straight line until near the end of the track where a sudden maximum appears. This maximum of ionization is called Bragg Peak.

The range of particles in matter, depending on the matrix of the target material and the projectile itself, can be determined by the following formula:

$$R(E) = \int_{E_0}^0 \frac{1}{\frac{dE}{dx}} dE \quad (2.2)$$

with E_0 as the bombarding energy.

Thus, in air, 3 MeV protons lose their hole energy in about 150 mm.

Figure 2.1 shows a simulation made with TRIM (Transport of Ions in Matter), a computer program for the determination of the range and the stopping power of ions in matter [Ziegler and Biersack, 2008].

One has to distinguish between thick and thin samples, if either the incident particle is stopped in matter or not. The PIGE technique usually uses thick samples since the strong energy dependence of the prompt γ -reaction cross-section is not a problem because the yield is integrated over the whole energy range [Calastrini et al., 1998].

2.3. Electromagnetic radiation in matter

Contrary to charged particles, which continuously lose energy in matter and therefore have a definite range, the interactions of photons occur in one point.

A photon can only be removed from the incident beam which implies an exponential

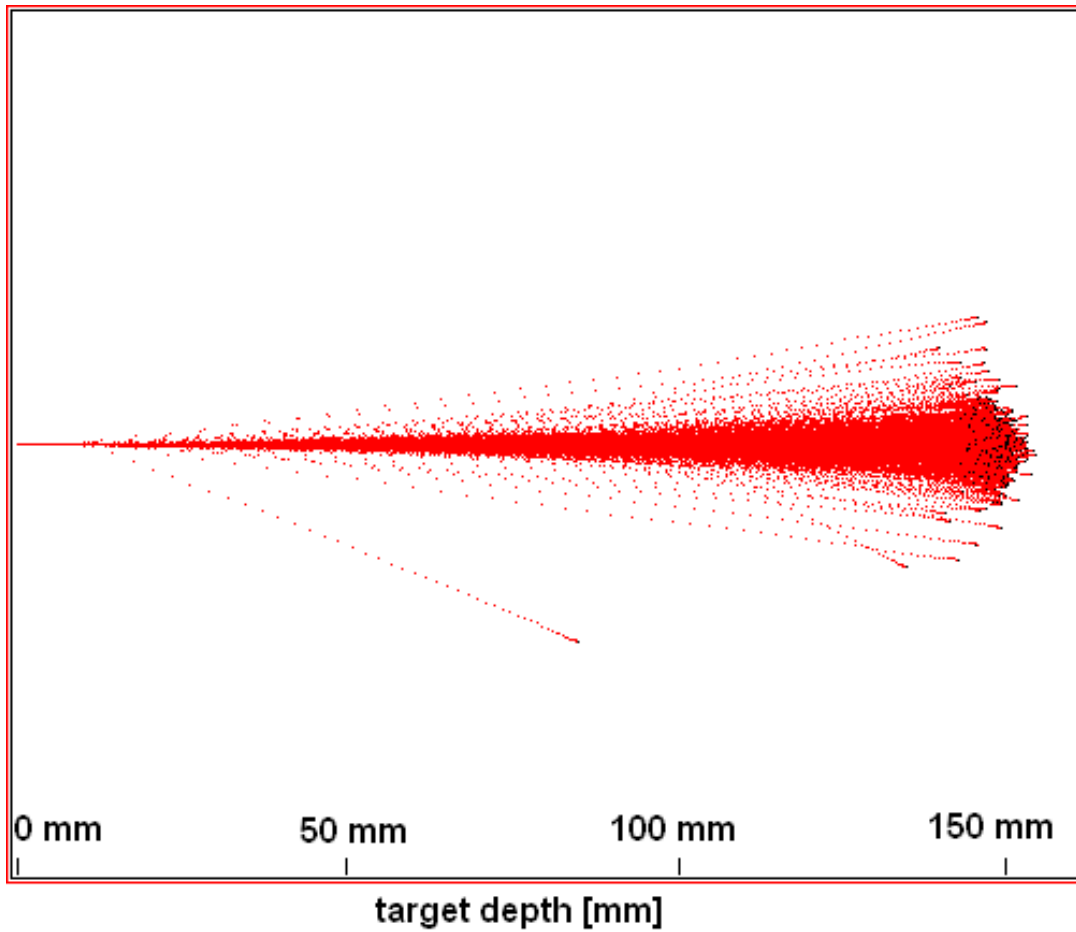


Figure 2.1.: TRIM-simulation for 3 MeV protons. Most of the projectiles are stopped at about 150 mm.

intensity loss. The Lambert's law characterizes the size of energy absorption per unit length:

$$I(x) = I_0 e^{-\mu x} \quad (2.3)$$

The absorption coefficient μ defines the scale to which a material absorbs energy.

In general, the loss of intensity is depended on three major quanta phenomena:

- Compton effect
- photoelectric effect
- pair production

which are illustrated in figure 2.2.

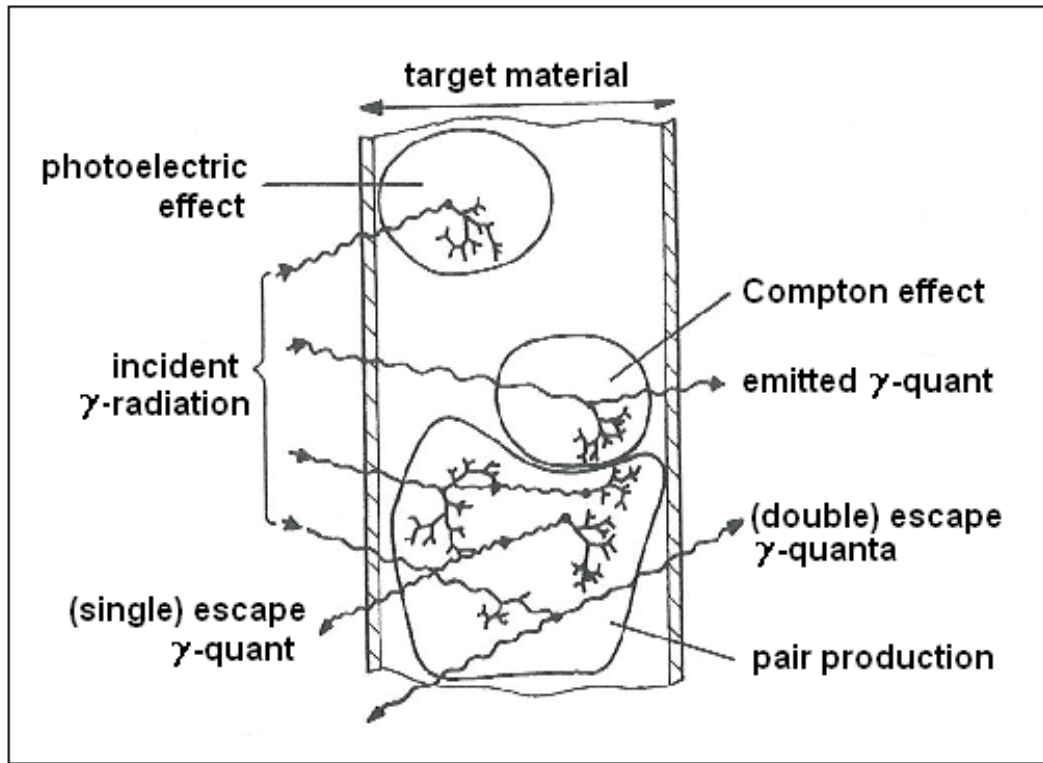


Figure 2.2.: A schematic layout of the three main absorption processes. The branchings at the end of the trace belong to electrons, the waved lines illustrate γ -quanta [Klaus Bethge, 2001].

For lead as absorber element the particular absorption processes and their energy dependences are shown in figure 2.3.

The table 2.1 gives a review over their characteristic dependence on the atomic number Z of the target and on the photon energy E_γ .

| absorption process | Z dependence | energy dependence |
|----------------------|-----------------------|-------------------|
| photoelectric effect | $Z^{4 \text{ to } 5}$ | E_γ^{-3} |
| Compton effect | Z | E_γ^{-1} |
| pair production | Z^2 | $\ln E_\gamma$ |

Table 2.1.: Z and E_γ dependence of the three main photon interactions

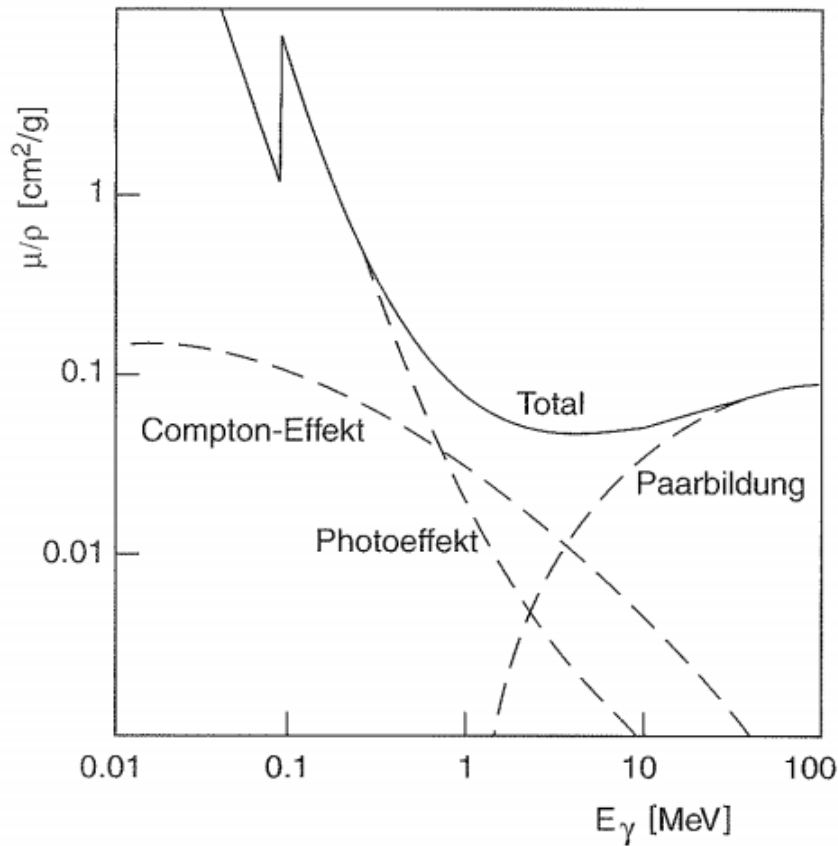


Figure 2.3.: Absorption coefficient μ for γ -rays in lead, normalized on density ρ , as a function of photon energy. The total absorption coefficient is determined as the sum of the three single contributions shown as dashed lines [Povh et al., 2004].

Compton effect

The Compton effect is dominant in the range of several keV up to a few MeV.

If the binding energy E_{bin} of an outer shell electron of the target atom is smaller than the energy $h\nu$ of an incident photon, the quantum transfers a part of its energy E_{kin} to the electron (Compton scattering).

According to the conservation of energy it applies:

$$h\nu = E_{kin} + h\nu' \quad (2.4)$$

with $h\nu'$ as the energy of the scattered photon.

The scattering angle θ determines the energy transfer, which has its maximum at $\theta=180^\circ$. Figure 2.4 shows the sharp cutoff at this energy, which gives rise to the name Compton edge.

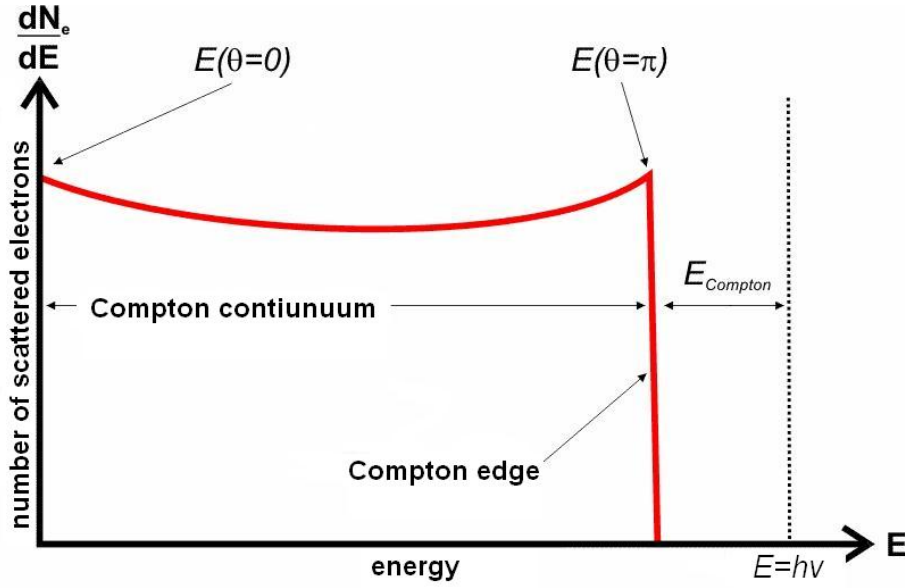


Figure 2.4.: An ideal energy γ -ray spectrum caused by electrons without pair production. The Compton continuum, created by the electrons scattered into different angles, drops off sharply at $\theta=180^\circ$, the so called Compton edge.

The spotted line characterizes the photoelectric effect.

Photoelectric effect

This process is mainly important for low photon energies up to some hundred keV. The ionization of an inner shell electron through total absorption of an incident photon ($h\nu > E_{bin}$) is called photoelectric effect.

An electron from a higher level refills the inner-shell vacancy whereupon a characteristic X-ray photon or an Auger electron with the released binding energy will be emitted.

Pair production

The creation of an elementary particle and its antiparticle, in particular an electron-positron-pair, is referred to as pair production. This interaction process requires at least the rest mass energy $m_e c^2$ of the two particles, i.e. $h\nu \geq 1.022 \text{ MeV}$ ($2m_e c^2$).

Annihilation is the inversed process of pair production.

When a positron produced due to pair production had lost almost its kinetic energy and annihilates with an electron of the absorber, two 511 keV γ -quanta are emitted. These two electromagnetic rays can both either be absorbed again through Compton effect or photoelectric effect or can leave the material without interactions. Thus, in a γ -spectrum, the single escape peak can be found 511 keV below the photo peak and the double escape peak another 511 keV beneath.

2.4. Methods of analysis with accelerated proton beams

To understand the advantage and limitation of the PIGE technique, it is beneficial to know other techniques used in IBA.

Some of the most established methods are listed below:

- Proton induced X-ray emission (**PIXE**) is a more often used complementary technique to PIGE. It is essentially used to determine heavy elements by their characteristic X-rays as a result of inner-shell ionization.
- In Rutherford backscattering (**RBS**), elastically backscattered protons are detected. This method is applied for heavy elements in light target materials.
- Recoiled target atoms can be detected after ejection from the sample. This technique, complementary to RBS, is called elastic recoil detection analysis (**ERDA**). Basically it is used to measure hydrogen in a thin layers and in near-surface regions of materials.
- In the nuclear reaction analysis (**NRA**) charged particle reaction products are detected. This surface-sensitive method provides informations about light elements in a target material.
- The detection of emitted Auger electrons is called Auger electron spectrometry (**AES**).

2.5. Principle of PIGE

In nuclear reaction analysis as well as in PIGE nuclear forces are of importance while in PIXE and RBS only electromagnetic and electrostatic forces are involved.

The PIGE method is less frequently applied than PIXE and RBS since first a nuclear reaction has to be induced. Therefore, the repulsive Coulomb barrier E_c has to be overcome. For protons with energy in the range of 1 - 4 MeV, E_c can be calculated with the following equation [Verma, 2007]:

$$E_c \cong \frac{Z_t}{A_p^{1/3} A_t^{1/3}} \text{MeV} \quad (2.5)$$

where A_p is the proton mass number and Z_t is the atomic number of the target atom with mass number A_t . If an incident proton has enough energy to penetrate into the nucleus of the target atom, a nuclear reaction may occur.

2. PIGE

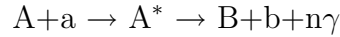
In principle, a compound nucleus in an excited state is generated and rearranges under emission of γ -rays and, if possible, of other nuclear particles. The detected γ -energies are characteristic of the nuclei emitting the radiation.

Furthermore, the corresponding rate of the γ -ray yields of the induced reactions allows to determine the concentrations of elements in the sample material.

Usually such a nuclear reaction is written in the form:



In particular:



where A is the target atom, a the projectile, A^* the compound nucleus, B the reaction product, b the ejected particle and $n\gamma$ the numbers of γ -rays emitted during the de-excitation.

The conservation of energy is given by:

$$E_a + Q = E_b + E_B + E_\gamma \quad (2.6)$$

where E_a , E_b and E_B are the kinetic energies of the involved particles and ejectiles, E_γ is the energy of the emitted γ -ray and Q is the Q-value of the reaction.

The Q-value is defined as the amount of energy released or absorbed by a nuclear reaction. It classifies exothermic ($Q > 0$) and endothermic ($Q < 0$) reactions. If $Q > 0$, energy is released but for $Q < 0$ a minimum energy higher than the Q-value is necessary to initiate a nuclear reaction.

Most of the nuclei have sharp, proton energy dependent resonances in their (γ,x) excitation functions. However, in the PIGE analysis often Coulomb excitation $(p,p'\gamma)$ is the dominant reaction.

The most important reactions for 3 MeV protons are listed in table 2.2.

2.6. PIGE method: detection and limitation

Elements in a target are classified on a quantity basis. The main elements in a sample in the order of tens of percent are considered "matrix". "Minor" elements are in the range of a few percent and those which are in the order of a thousandth part to parts per million (ppm) are called "trace" elements. The detection limit for PIGE varies from one element to another and could reach down to ppm.

Problems with the application of the PIGE method are mostly caused by following reasons:

- The sensitivity for specific elements is limited to the range of $3 < Z < 20$ due to the increase of the Coulomb repulsion with the atomic number Z .

| element | reaction | E_γ [keV] |
|---------|---|-----------------------------|
| Li | ${}^7\text{Li}(\text{p}, \text{n}\gamma){}^7\text{Be}$ | 429 |
| | ${}^7\text{Li}(\text{p}, \text{p}'\gamma){}^7\text{Li}$ | 478 |
| B | ${}^{10}\text{B}(\text{p}, \alpha\gamma){}^7\text{Be}$ | 429 |
| | ${}^{10}\text{B}(\text{p}, \text{p}'\gamma){}^{10}\text{B}$ | 718 |
| | ${}^{11}\text{B}(\text{p}, \text{p}'\gamma){}^{11}\text{B}$ | 2125 |
| F | ${}^{19}\text{F}(\text{p}, \text{p}'\gamma){}^{19}\text{F}$ { | 110 |
| | ${}^{19}\text{F}(\text{p}, \alpha\gamma){}^{16}\text{O}$ | 197 1236 1357 6129 |
| Na | ${}^{23}\text{Na}(\text{p}, \text{p}'\gamma){}^{23}\text{Na}$ | 440 |
| | ${}^{23}\text{Na}(\text{p}, \alpha\gamma){}^{20}\text{Ne}$ | 1634 |
| | ${}^{23}\text{Na}(\text{p}, \text{p}\gamma){}^{23}\text{Na}$ | 1636 |
| Al | ${}^{27}\text{Al}(\text{p}, \text{p}'\gamma){}^{27}\text{Al}$ { | 844 |
| | ${}^{27}\text{Al}(\text{p}, \alpha\gamma){}^{24}\text{Mg}$ | 1014 |
| | ${}^{27}\text{Al}(\text{p}, \gamma){}^{28}\text{Si}$ | 1369 1779 |
| Si | ${}^{28}\text{Si}(\text{p}, \text{p}'\gamma){}^{28}\text{Si}$ | 1779 |
| | ${}^{29}\text{Si}(\text{p}, \text{p}'\gamma){}^{29}\text{Si}$ { | 755 |
| | ${}^{30}\text{Si}(\text{p}, \text{p}'\gamma){}^{30}\text{Si}$ | 1273 |
| | ${}^{30}\text{Si}(\text{p}, \gamma){}^{31}\text{P}$ | 2028 2235 2233 |
| P | ${}^{31}\text{P}(\text{p}, \alpha\gamma){}^{28}\text{Si}$ | 1779 |
| | ${}^{31}\text{P}(\text{p}, \gamma){}^{32}\text{S}$ | 2230 |
| | ${}^{31}\text{P}(\text{p}, \text{p}'\gamma){}^{31}\text{P}$ { | 1266 2233 |

Table 2.2.: Typical nuclear reactions and the emitted γ -ray-energies of light elements used in PIGE analysis [Tesmer and Nastasi, 1995].

2. PIGE

- The intensity of the proton induced γ -rays increases with the proton energy which makes the PIGE technique strongly energy dependent.
- PIGE is isotope-sensitive.
Generally, different isotopes of the same element have different nuclear reactions. For this reason, every possible reaction in the sample matrix, with its yield and its γ -energy must be known.

In summary, the PIGE technique cannot be used as easily as PIXE and RBS but in some cases it is a powerful unique tool. To cover the most important elements in ion beam analysis, the PIGE technique is most often run in combination with PIXE and RBS.

For the detection of γ -radiation between 50 keV and 10 MeV a Ge(Li) or a high-purity germanium (HPGe) detector is commonly used. Both detectors are semi conducting and have a typical energy resolution of about 2-3 keV at 1.173 MeV γ -ray of the ^{60}Co photon. The detectors require liquid nitrogen for cooling to reduce the thermal leakage current and the electronic noise.

The detector efficiency at high energies is only a function of the detector volume, hence, the thickness of the detector window is negligible. For low-energy γ -ray measurement the detector is provided with a beryllium window to take the full advantage of the semi conducting property.

PIGE measurements can be efficiently performed in vacuum and in air.

Since MeV protons lose almost no energy by penetrating thin layers (exit window of the proton beam) and small distance in air (between the target and the exit window), an external PIGE setup is possible. This is often advantageous or even necessary, e.g. investigation of art objects.

Instead of free atmospheric air sometimes a helium flush is used for cooling the sample surface and for avoiding the appearance of the atmospheric argon lines.

At our PIGE setup at VERA, measurements without helium flush were performed, because the argon peak (observed by an X-ray detector) was required for the current calibration, see chapter 5.

3. Experimental Setup

3.1. PIGE facility at the VERA laboratory

The Vienna Environment Research Accelerator (VERA) was built by National Electrostatics Corporation (NEC) in Wisconsin, USA, and was put on operation in 1996 [Kutschera et al., 1997][Priller et al., 1997]. The facility consists of a 3 MV Pelletron tandem accelerator and was basically established to perform Accelerator Mass Spectrometry (AMS) experiments. In 2001, a VERA upgrade provides to span its range to almost "all" isotopes [Steier et al., 2004].

VERA extended its performance to PIXE measurements in 2004. The first step of ion beam analysis was made.

To enable flexible working processes, a second cesium-sputter ion source was constructed in autumn 2007. A current version of the VERA scheme is shown in figure 3.1.

To produce an ion beam, a sample wheel is installed into one of two cesium-sputter ion source. Both sources are MC-SNICS (Multi Cathode - Source for Negative Ions by Cesium Sputtering), which means that up to 40 samples can be loaded into the target wheel [Vockenhuber et al., 2003]. After extracting the negative ions from the source, they are preaccelerated to 75 keV.

The low-energy injection system consists of two parameter: the 45° electrostatic analyzer (ESA) for ion source #1 (two 45° ESA for ion source #2) and the 90° bending magnet (BM).

The ESA selects the ions according to their energy:

$$\epsilon \cdot \rho_{ESA} = \frac{2E}{qe} \quad (3.1)$$

with

ϵ ...electric field strength of maximum 6 kV/cm

ρ_{ESA} ...bending radius about 0.3 m

E ...energy of the ions

q ...charge state of the ions (for protons: $q = -1$)

e ...elemental charge

3. Experimental Setup

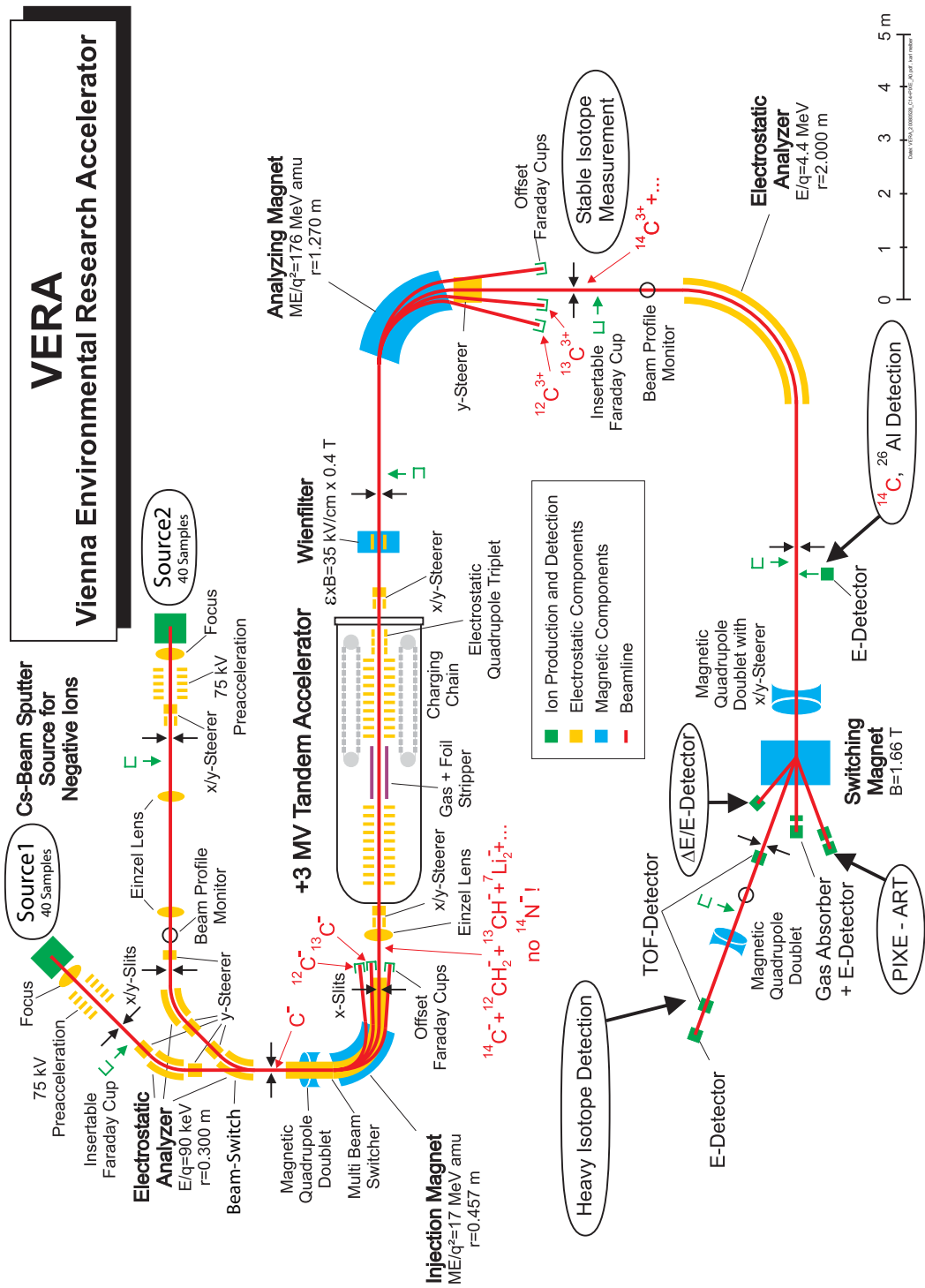


Figure 3.1.: A schematic layout of the VERA facility at the university of Vienna. The PIGE and PIXE experiments were performed at same location, indicated as (PIXE-ART).

For a fixed magnetic field $B = 1.25$ T and a bending radius of $\rho_{BM} = 0.457$ m only particles with mass m and therefore, with a certain magnetic rigidity $B\rho_{BM}$ can reach the accelerator.

$$B \cdot \rho_{BM} = \frac{\sqrt{2mE}}{q} \quad (3.2)$$

In the tandem accelerator the injected negative ions are accelerated by the high positive voltage of the terminal which runs with maximum 3 MV. Two charging chains transport the positive charge onto the terminal. The negative ions are accelerated towards the terminal and undergo a charge exchange in the terminal due to the stripping process. Several outer-shell electrons are stripped off through a thin foil or a gas and the generated positive charged ions are accelerated again from the terminal to the high energy side of the beamline.

On the high-energy side the ions are selected a second time by a 90° analyzing magnet (maximum field $B = 1.53$ T and a radius $\rho_{BM} = 1.27$ m) and a 90° electrostatic analyzer (maximum electric field strength of $E = 55$ kV/cm and a radius $\rho_{ESA} = 2$ m) before they reach the end of the beamline. PIGE and PIXE experiments were performed simultaneously at same location: the so called PIXE-ART.

Depending on the source, TiH_2 ("old" source #1) or HfH_2 ("new" source #2) is used to produce H^- ions. PIGE measurements are in principle performed with 3 MeV protons, thus, the terminal voltage is set about 1.5 MV. To obtain a typical proton current in the region of 1-10 nA, the x/y-slits after the tandem accelerator are varied in the spacing. A magnetic quadrupole doublet after the second ESA allows to focus the H^+ beam to the PIXE-ART location (for details see chapter 4.3).

The protons leave the vacuum (10^{-6} mbar), by passing through the nozzle, a $150 \mu\text{m}$ carbon collimator sealed with a 100 nm thick Si_3N_4 foil [Milota et al., 2008]. The sample is positioned in 1 cm distance from the exit window.

To determine the energy loss of the protons from vacuum to target position, a calculation with TRIM was performed. The H^+ -energy inside the beamline is 3.12 MeV according to the exactly terminal voltage of 1.56 MV. The protons lose about 2.95 keV by penetrating the 100 nm thick Si_3N_4 foil, which is negligible. The absorption in air is about 0.12 MeV. Therefore, 3 MeV protons hit the sample.

3.2. PIGE setup

A HPGe detector (GMX series) was placed, at 45° with respect to the beam axis, 7 cm from the target to collect the proton induced γ -rays. The nominal efficiency and the resolution of the detector are 20% and 1.9 keV respectively for the 1.33 MeV γ -peak of a ^{60}Co source. During the measurements the HPGe detector was shielded by means of a lead cylinder.

3. Experimental Setup

A 30 mm² Si(Li) detector, set at an angle of 45° to external proton beam, recorded simultaneously the produced X-rays (in particular the Ar K_α line). For the backscattered protons a RBS detector was installed at an angle of 45° beneath.

A drawing of the whole PIXE-ART facility is illustrated in figure 3.2.

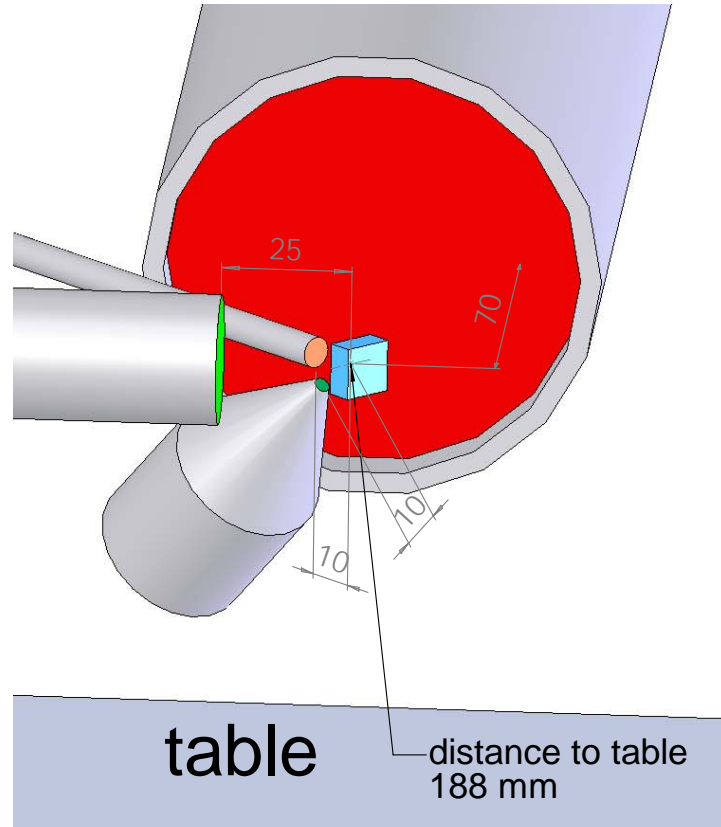


Figure 3.2.: Drawing of the PIXE-ART facility. Distances to the sample on the scale of mm are indicated.

A laser positioning system consisting of two lasers was used. A green laser, collinear with the proton beam, defines the impact position on the sample. The second one, a red laser (cross shaped), was mounted above the nozzle at an angle of 45°. To guarantee the same geometry for each measurement, the interaction point of both lasers was adjusted at 1 cm distance from the nozzle exit window.

Besides, a TV-camera was directed at the investigated object to improve and control the laser position.

The target sample was moved in XYZ-axis to the laser cross-over point in front of the exit window by means of the "PIXE-manipulator", a motor-driven positioning table (EP1090 from ISEL).

A photograph of the current PIGE setup is shown in figure 3.3.

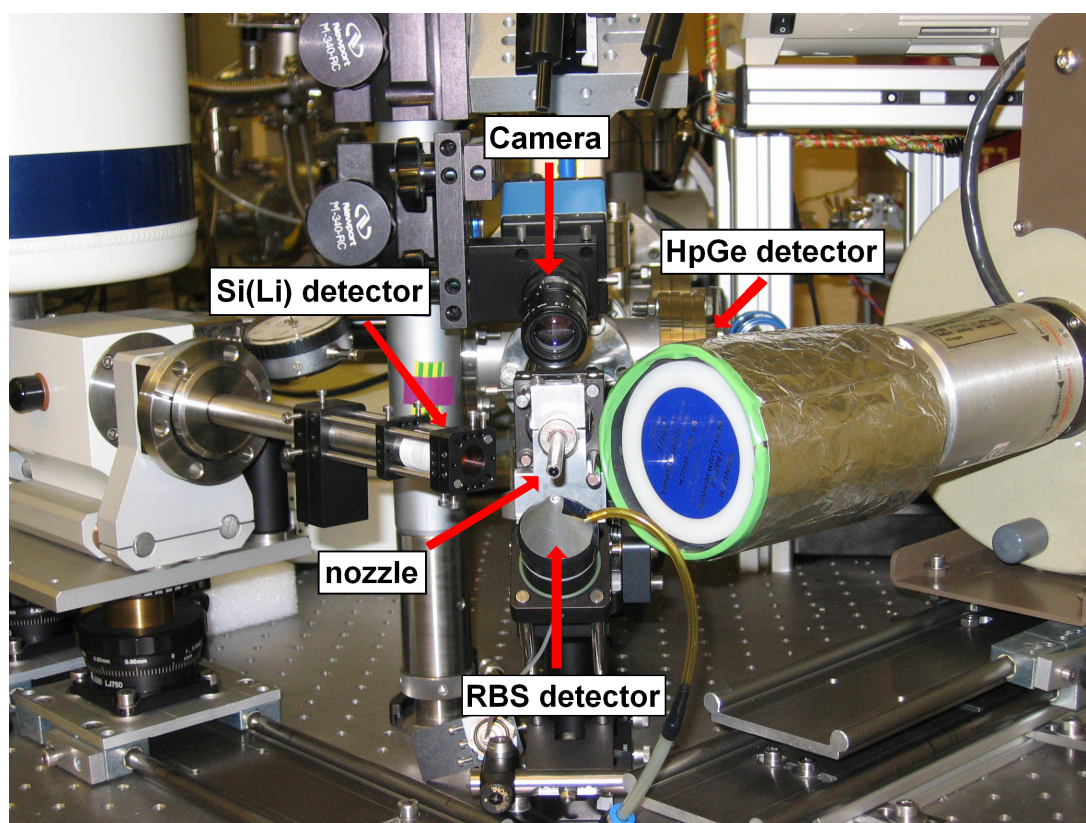


Figure 3.3.: A photograph of the present PIXE-ART facility.

3. *Experimental Setup*

4. Background

4.1. Natural background

Before any measurements with samples were performed, the background radiation had to be known. Figure 4.1 shows a typical background spectrum accumulated at the PIXE-ART facility.

Unfortunately the background radiation is relative high since the bricks of building contain an elevated concentration of radionuclides of the natural decay series.

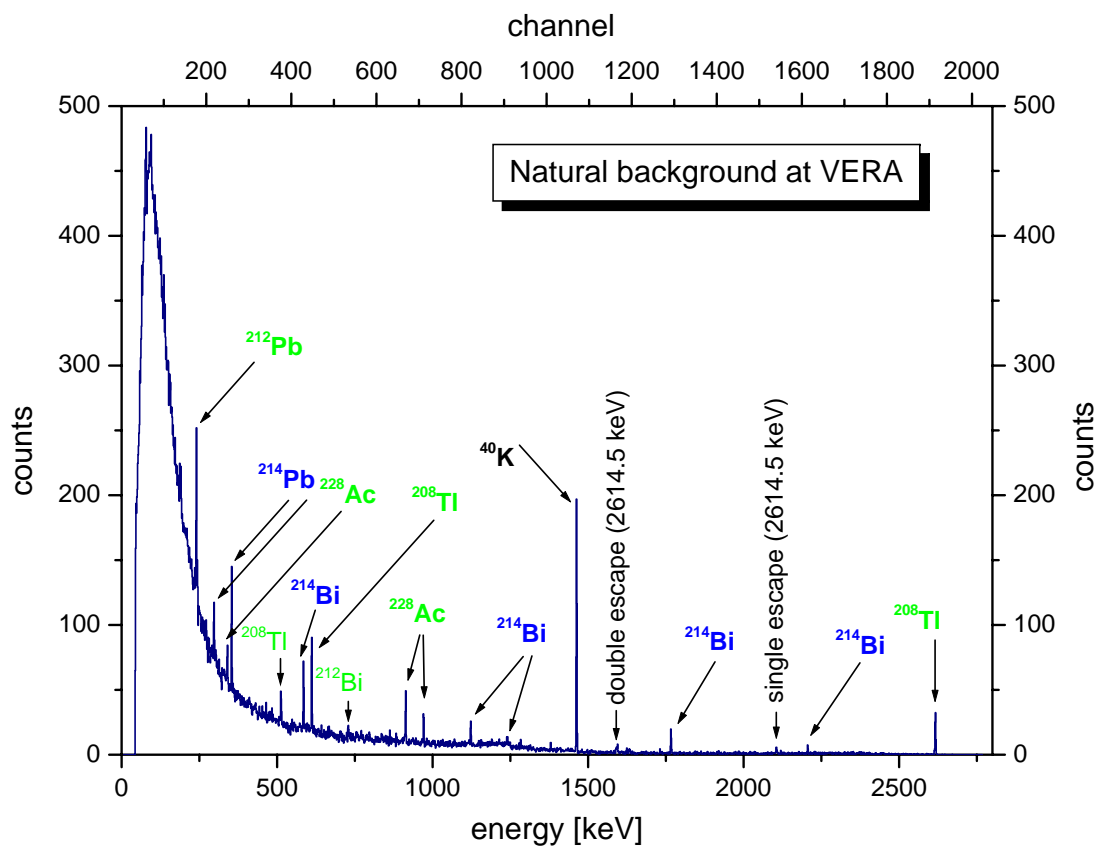


Figure 4.1.: Background spectrum at VERA accumulated without lead shielding. The γ -lines belonging to the radioactive series are distinguished by color. (^{232}Th -green, ^{238}U -blue)

4. Background

An energy calibration of the background spectrum was determined by the mean of ^{137}Cs and ^{60}Co sources, but according to the strong intensity of the natural background lines ^{40}K and ^{208}Tl (shown in figure 4.1), a calibration without radioactive sources is possible. The uncertainties of the energy calibration is in the range of 0.5-1 keV, while the FWHM (full width at half maximum) of the γ -lines is in the order of 1.4 %.

With WIRUK, a program to perform γ -spectrum analysis, and NuDat [National Nuclear Data Center, 2008], a software product that allows to search and plot nuclear structure and nuclear decay data, the decay radiation was identified. Moreover, the WIRUK program considers the background and provides the net peak area which is abbreviated during the whole work as P.A. (peak area).

All γ -lines of the spectrum could be assigned to the natural decay series ^{232}Th and ^{238}U , which are illustrated in figure D.1 and D.2 in appendix D.

The determined γ -lines are listed in table 4.1.

| decay product | E_γ [keV] | I [%] | decay series |
|---------------------|------------------|-------|-------------------|
| ^{212}Pb | 238.63 | 43.6 | ^{232}Th |
| ^{212}Bi | 727.33 | 6.7 | |
| ^{228}Ac { | 338.32 | 11.3 | |
| | 911.20 | 25.8 | |
| | 968.97 | 15.8 | |
| ^{208}Tl { | 510.77 | 22.6 | |
| | 583.19 | 85 | |
| | 2614.51 | 99.8 | |
| ^{214}Pb { | 295.22 | 19.3 | ^{238}U |
| | 351.93 | 37.6 | |
| ^{214}Bi { | 609.31 | 46.1 | |
| | 1120.29 | 15.1 | |
| | 1238.11 | 5.79 | |
| | 1764.94 | 15.4 | |
| | 2204.21 | 5.08 | |
| ^{40}K | 1460.82 | 10.66 | |

Table 4.1.: The identified natural background γ -lines at VERA, with corresponding γ -energies and γ -intensities.

A lot of light elements have γ -ray energies in the low energy region, where our background is too high to determine trace elements. Therefore, a cylindrical, 4 mm thick lead shielding was constructed around the HPGe detector to reduce the natural background. A reduction of about 70 % (in the energy range up to 400-500 keV) could be achieved. The difference between a shielded and an unshielded γ -ray spectrum is illustrated in figure 4.2.

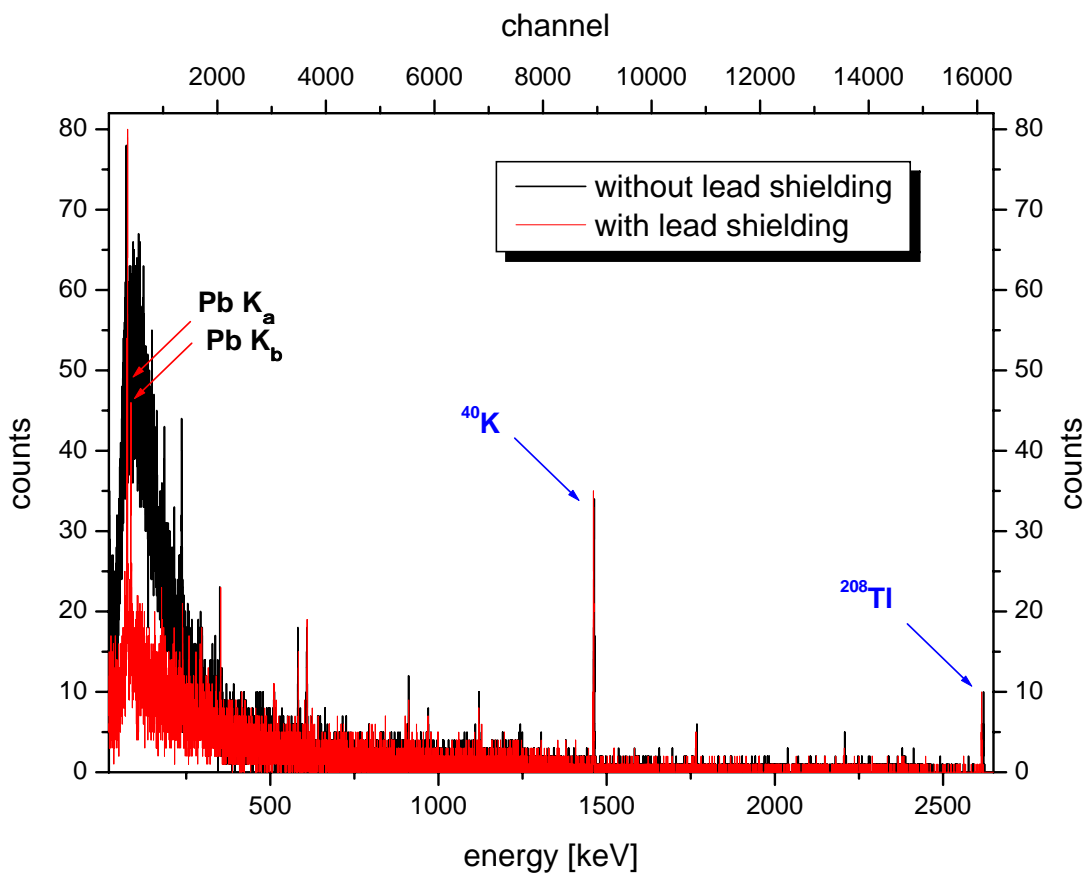


Figure 4.2.: Comparison of a background spectrum at VERA with and without lead shielding.

Remark: The lead X-rays $\text{Pb } K_{\alpha}$ at 74.97 keV and $\text{Pb } K_{\beta}$ at 84.94 keV appear in the spectrum with the lead shielding.

4.2. Influence of the PIXE-ART modification on the proton induced background

4.2.1. Primary proton induced background

Accelerated protons can induce nuclear reactions inside the beamline especially at the collimator. For this reason, a "proton on air" background spectrum (without sample) was compared to a natural background spectrum, see figure 4.3.

Irradiation was performed with 3 MeV protons for 300 s.

The recorded proton induced γ -rays are listed in table 4.2. Characterizations of γ -lines are described in column "comment".

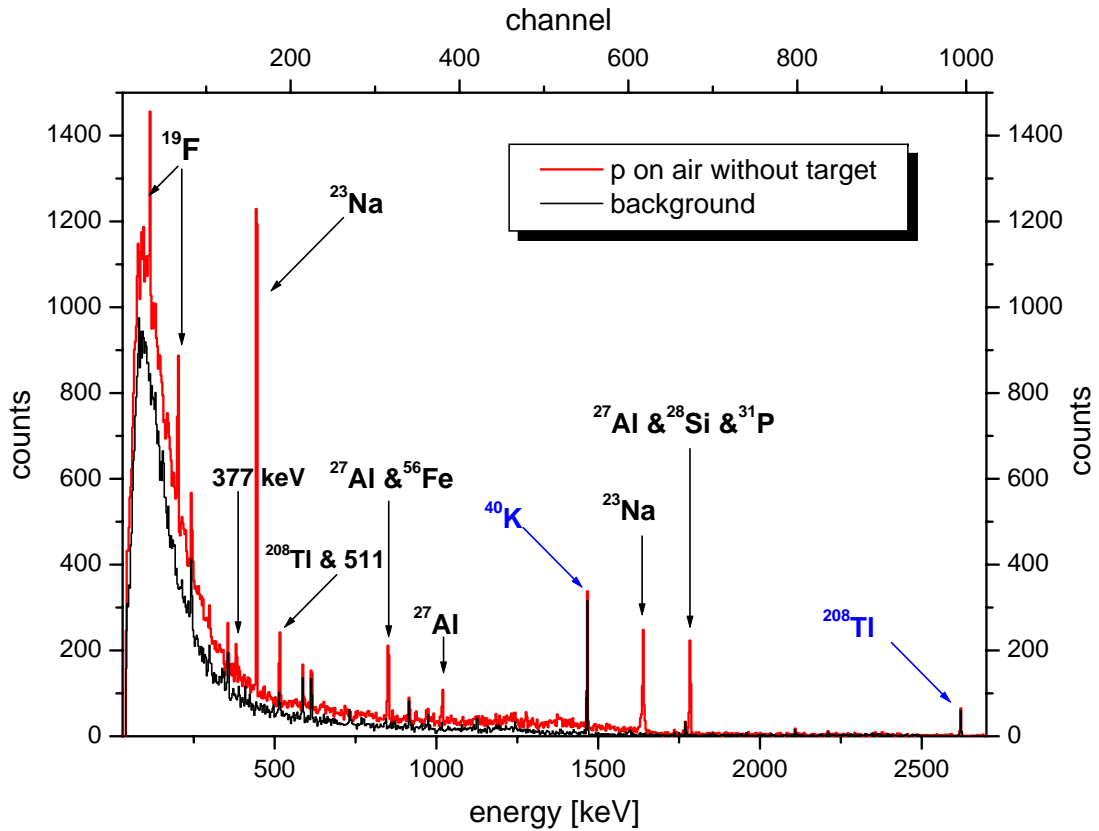


Figure 4.3.: Comparison: background and proton induced background without sample. Both spectra recorded by an unshielded HPGe-detector. The plot shows proton induced γ -ray lines, illustrated black. The calibration lines ^{40}K and ^{208}Tl are labeled blue.

This spectrum shows an overlap of the 511 keV line due to the annihilation of positrons with the 510.8 keV line of ^{208}Tl of the natural background.

Besides the peaks corresponding to the $^{19}\text{F}(\text{p},\text{p}'\gamma)^{19}\text{F}$ reaction, the characteristic γ -

4.2. Influence of the PIXE-ART modification on the proton induced background

rays of ^{23}Na are observed. The high-energy peak of ^{23}Na could be an overlapping of both the 1634 keV line and 1636 keV line, since the FWHM of about 4.3 keV is relative wide compared to other lines .

In the case of ^{27}Al , two γ -ray lines overlap with those of other elements. To distinguish between these nuclides, the corresponding non-overlapping 1014 keV line was used for identification. Since these lines are produced inside the beamline the data of table 4.3, which show the absolute thick target γ -ray yields, can be used for comparison. A detailed description can be found in [Tesmer and Nastasi, 1995].

| energy [keV] | reaction | comment |
|--------------|---|--|
| 110 | $\left. \begin{array}{l} \\ \end{array} \right\} ^{19}\text{F}(\text{p},\text{p}'\gamma)^{19}\text{F}$ | |
| 197 | | |
| 440 | $^{23}\text{Na}(\text{p},\text{p}'\gamma)^{23}\text{Na}$ | |
| 511 | annihilation | overlap: ^{208}Tl |
| 844 | $\left. \begin{array}{l} ^{27}\text{Al}(\text{p},\text{p}'\gamma)^{27}\text{Al} \\ ^{56}\text{Fe}(\text{n},\text{n}'\gamma)^{56}\text{Fe} \end{array} \right\}$ | overlap |
| 846.8 | | |
| 1014 | $^{27}\text{Al}(\text{p},\text{p}'\gamma)^{27}\text{Al}$ | |
| 1634 | $\left. \begin{array}{l} ^{23}\text{Na}(\text{p},\alpha\gamma)^{20}\text{Ne} \\ ^{23}\text{Na}(\text{p},\text{p}'\gamma)^{23}\text{Na} \end{array} \right\}$ | overlap |
| 1636 | | |
| 1779 | $^{27}\text{Al}(\text{p},\text{p}'\gamma)^{27}\text{Al}$ | overlap: $^{28}\text{Si}, ^{31}\text{P}$ |

Table 4.2.: By energy listed proton induced γ -rays of the "old" PIXE-ART setup.

| element | energy [keV] | yield $\left[\frac{N_\gamma}{\mu\text{Csr}} \right]$ | reaction |
|------------------|--------------|---|--|
| ^{27}Al | 844 | $2.3 \cdot 10^6$ | $^{27}\text{Al}(\text{p},\text{p}'\gamma)^{27}\text{Al}$ |
| ^{27}Al | 1014 | $4.6 \cdot 10^6$ | $^{27}\text{Al}(\text{p},\text{p}'\gamma)^{27}\text{Al}$ |
| ^{27}Al | 1779 | $1 \cdot 10^4$ | $^{27}\text{Al}(\text{p},\gamma)^{28}\text{Si}$ |
| ^{28}Si | 1273 | $1.2 \cdot 10^5$ | $^{29}\text{Si}(\text{p},\text{p}'\gamma)^{29}\text{Si}$ |
| ^{28}Si | 1779 | $1.2 \cdot 10^6$ | $^{28}\text{Si}(\text{p},\text{p}'\gamma)^{28}\text{Si}$ |
| ^{31}P | 1266 | $1.6 \cdot 10^6$ | $^{31}\text{P}(\text{p},\text{p}'\gamma)^{31}\text{P}$ |
| ^{31}P | 1779 | $2.1 \cdot 10^5$ | $^{31}\text{P}(\text{p},\alpha\gamma)^{28}\text{Si}$ |

Table 4.3.: The absolute thick target γ -ray yield values for Al, Si and P bombarded with 3.1 MeV protons. The yield unit is the number of γ -rays (N_γ) per solid angle (sr) and total accumulated charge (μC).

4. Background

The ratios of the 844 keV line and the other ^{27}Al γ -ray lines do not fit to the literature. Hence, the 844 keV line and the 1779 keV line must be an overlapping of other γ -lines from other nuclear reaction. Since the 1779 keV line can be caused by nuclear reactions with ^{28}Si and ^{31}P , these reactions will also contribute to the peak area. By the reason that no other ^{28}Si - and ^{31}P -lines were observed, the amount of each nuclide is unclear.

The analysis identified an other line at 846.8 keV. In this spectrum this line could not be separated from the 844 keV line, due to the limited number of channels. As shown in the level scheme in figure 4.5 the 846.8 keV line is probably emitted by ^{56}Fe .

Apart from Coulomb excitation, neutron induced nuclear reactions can feed the excited state in ^{56}Fe . Neutrons can be produced inside the beamline.

By mean of EXFOR, an experimental nuclear reaction database, the cross section for the $^{56}\text{Fe}(n,n\gamma)^{56}\text{Fe}$ nuclear reaction was determined, see figure 4.4 [IAEA, 2008], [F.G. Perey et al., 2008].

The plot shows that the cross section is high enough to expect γ -rays from the $^{56}\text{Fe}(n,n\gamma)^{56}\text{Fe}$ reaction in the spectrum.

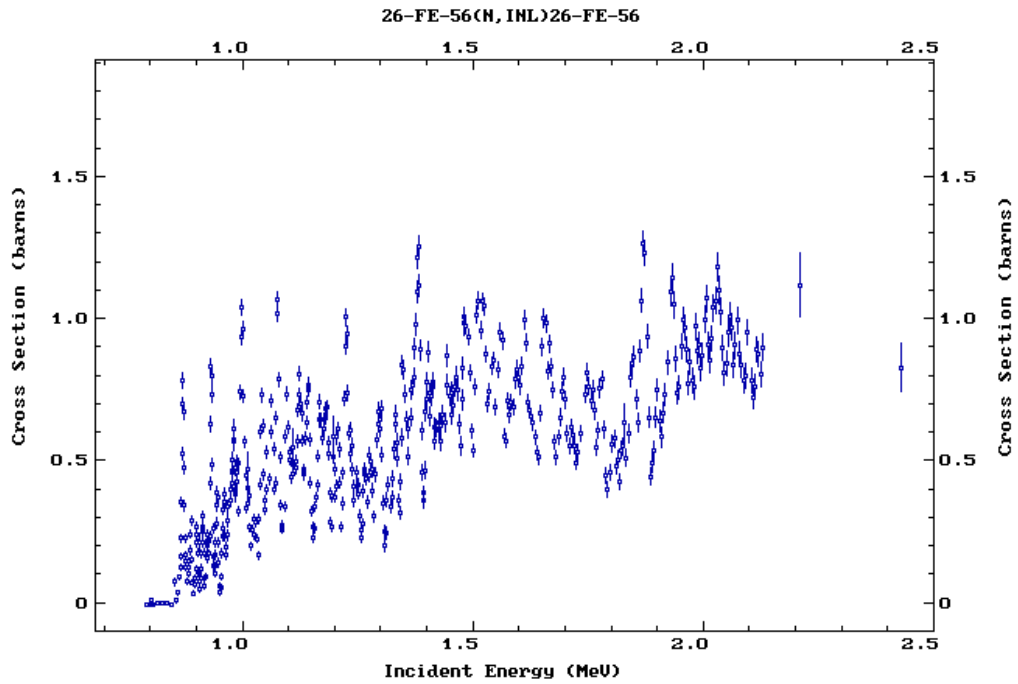
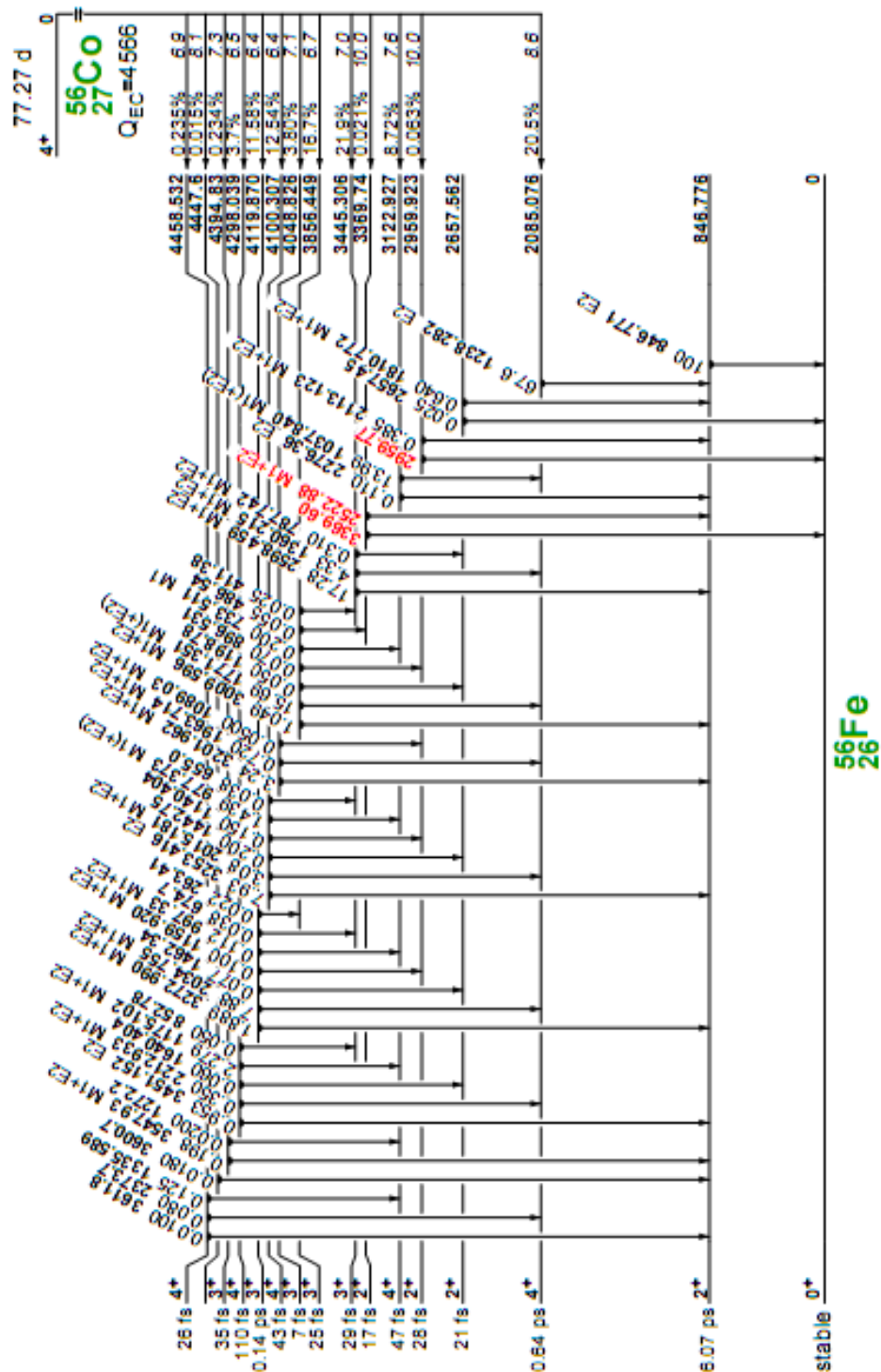


Figure 4.4.: The cross section of the $^{56}\text{Fe}(n,n\gamma)^{56}\text{Fe}$ nuclear reaction as a function of neutron energy.

Our contact in FZD (Forschungszentrum Dresden-Rossendorf), Christian Neelmeijer, corroborates our assumption. In Rossendorf, the irradiation of an iron standard with 4 MeV protons provides the expected γ -ray at 846.8 keV related to ^{56}Fe . More details, see appendix A.

4.2. Influence of the PIXE-ART modification on the proton induced background



An other γ -ray line produced inside the beamline is recorded at about 377 keV. Since there is no overlap with other γ -rays relevant for PIGE, this line is insignificant.

The origin of the fluorine and sodium lines is still unclear, but it is obviously a fact, that those elements are constituents of the PIXE-ART facility. Aluminum and iron are known components of construction material.

4.2.2. PIXE-ART modification

To upgrade the geometry and stability of the PIXE-ART facility, several components, e.g. the nozzle holder, which were suspicious to cause background γ -lines were replaced.

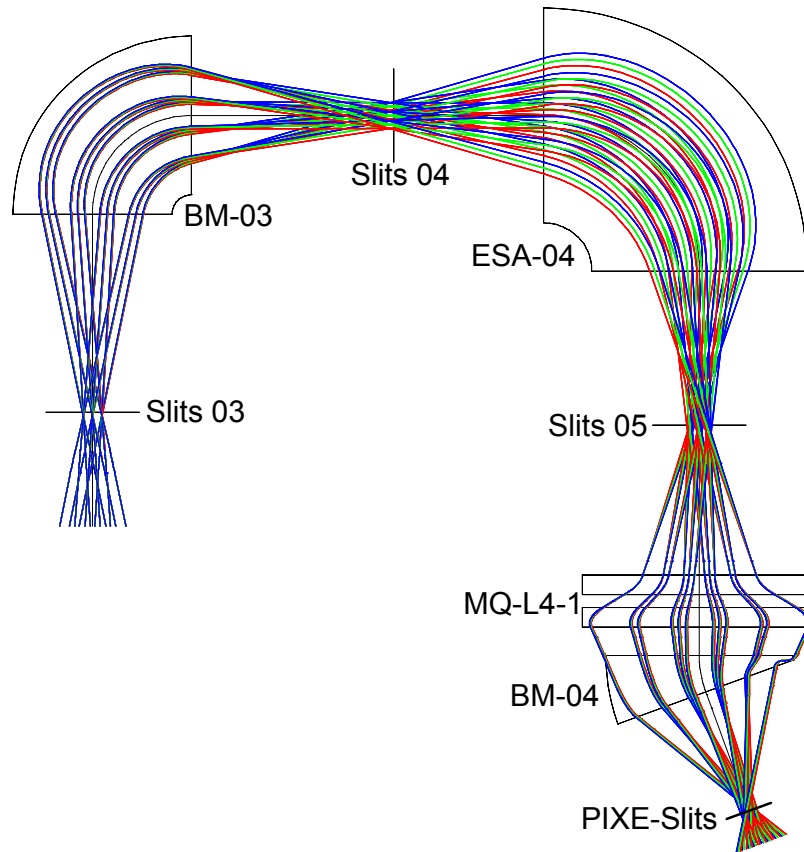


Figure 4.6.: Output of a COSY simulation of a H^+ -beam passing through the high energy side of the beamline. The plot, which is not true to scale, shows the PIXE- slits almost in the focal point. Different average proton energies are indicated as: E_p (green), $E_p + \Delta E$ (blue) and $E_p - \Delta E$ (red). Abbreviations see figure 3.1.

4.2. Influence of the PIXE-ART modification on the proton induced background

Another setup-modification was the installation of the so called PIXE-slits, to reduce the proton induced background radiation from behind the slits by pre-collimating the proton beam in XY-direction before impinging on the nozzle collimator. To test their influence on the spectrum they can also be removed. For this reason a pair of movable steel slits with a spacing of 0.5 mm were constructed. The slits were mounted between the switcher magnet (distance about 1.4 m) and the nozzle (distance about 0.45 m), see chapter 5.

With COSY INFINITY, a simulation and analyze program for particle optical systems, an ion optical calculation of the VERA focal points were performed [Makino and Berz, 2006]. Figure 4.6 shows the simulation of a proton beam accelerated along the high energy side of the beamline. As expected, the PIXE-slits are almost in the focal point.

4.2.3. Present proton induced background

The modification of the PIXE-ART facility, influenced the proton induced background.

The difference of a "proton on air" PIGE spectrum with the old and the new setup can be seen in figure 4.7. The 3 MeV proton current was about the same (8 nA).

The accumulated γ -rays are listed in table 4.4. Overlapping lines are described in column "comment".

| energy [keV] | reaction | comment |
|--------------|---|------------------------------|
| 110 197 | $\left. \begin{array}{l} {}^{19}\text{F}(\text{p},\text{p}'\gamma){}^{19}\text{F} \end{array} \right\}$ | overlap: ${}^{208}\text{Tl}$ |
| 440 | ${}^{23}\text{Na}(\text{p},\text{p}'\gamma){}^{23}\text{Na}$ | |
| 511 | annihilation | |
| 844 846.8 | $\left. \begin{array}{l} {}^{27}\text{Al}(\text{p},\text{p}'\gamma){}^{27}\text{Al} \\ {}^{56}\text{Fe}(\text{n},\text{n}'\gamma){}^{56}\text{Fe} \end{array} \right\}$ | overlap: Fe more intensive |
| 1014 | ${}^{27}\text{Al}(\text{p},\text{p}'\gamma){}^{27}\text{Al}$ | |
| 1634 1636 | $\left. \begin{array}{l} {}^{23}\text{Na}(\text{p},\alpha\gamma){}^{20}\text{Ne} \\ {}^{23}\text{Na}(\text{p},\text{p}'\gamma){}^{23}\text{Na} \end{array} \right\}$ | overlap |
| 1779 | ${}^{27}\text{Al}(\text{p},\text{p}'\gamma){}^{27}\text{Al}$ | no overlap |

Table 4.4.: By energy listed proton induced γ -rays and nuclear reactions of the "new" PIXE-ART setup. Characterization of lines is described in the right column.

4. Background

The 1779 keV γ -ray line is reduced to a size, that is consistent with the other ^{27}Al lines. Thus, the component part which caused the ^{28}Si and ^{31}P contribution had been replaced.

Moreover, protons impinging on the Si_3N_4 exit window, induce no visible nuclear reaction with Si.

The 846.8 keV line of ^{56}Fe is in the new setup more intensive. This means an enhanced interaction of the H^+ -beam with the renewed iron containing construction material.

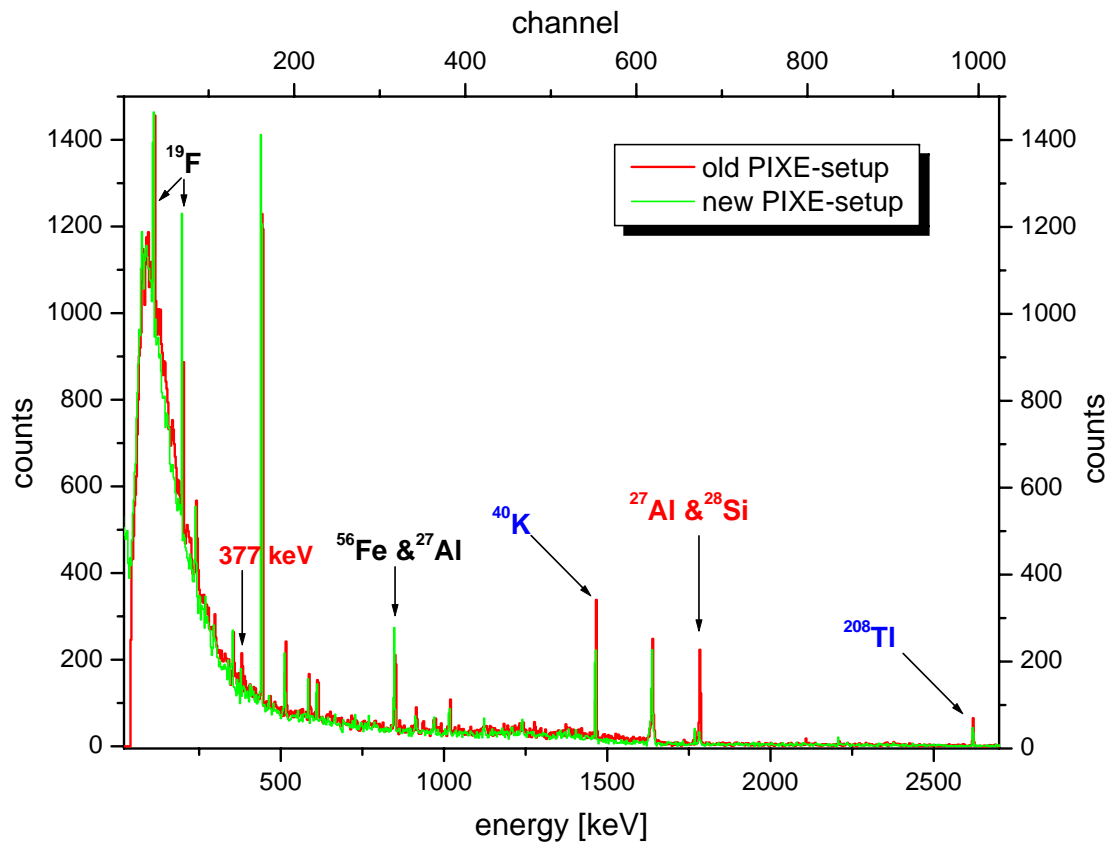


Figure 4.7.: Comparison of a "proton on air"-spectrum before and after the PIXE-ART modification. Both spectra are recorded by an unshielded HPGe-detector and without PIXE-slits. The green labeled lines correspond to the new setup, the red ones to the old setup. The calibration lines ^{40}K and ^{208}Tl are denoted blue.

To demonstrate the effect of the PIXE-slits, two "protons on air" PIGE-spectra with and without PIXE-slits are compared.

Both spectra, as shown in figure 4.8 were accumulated at the same beamtime.

With a proton current of about 7-9 nA, for 300 s.

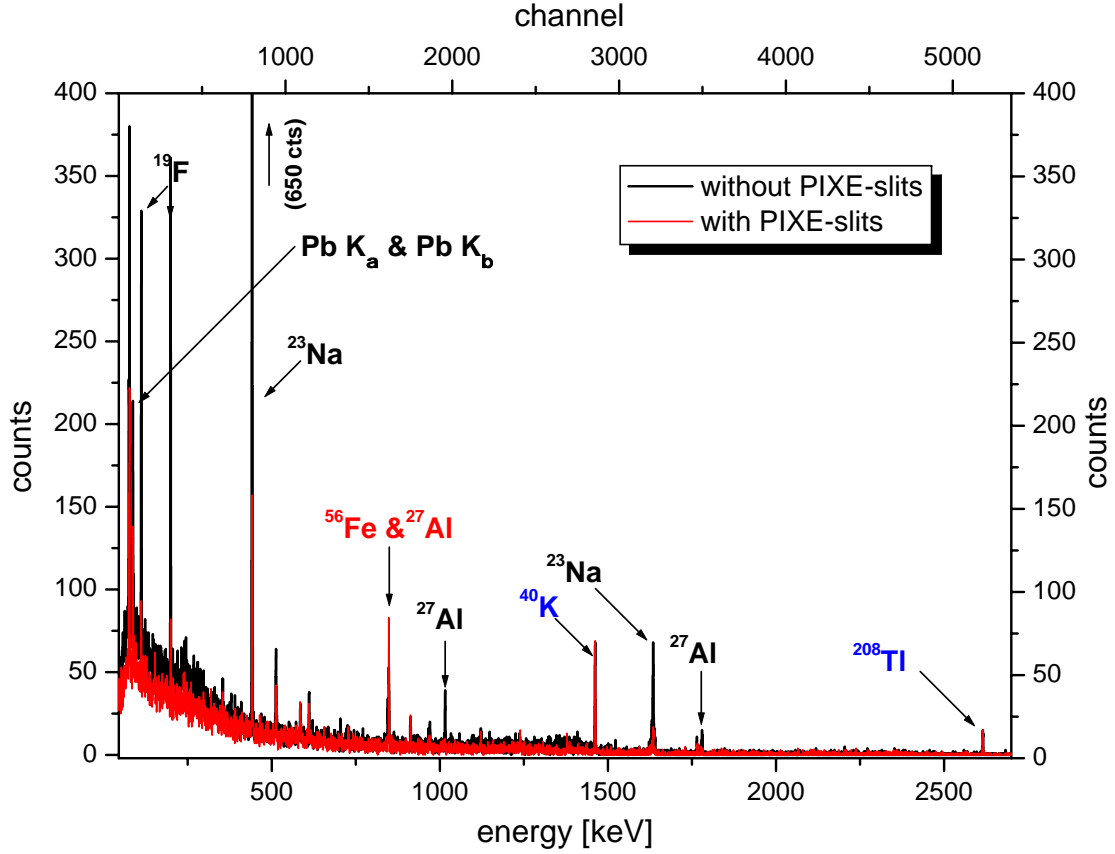


Figure 4.8.: Comparison of a "proton on air"-spectrum with and without PIXE-slits. The shielded lines are labeled in black, the intensified in red. The calibration lines ^{40}K and ^{208}Tl are labeled in blue.

The plot shows that almost all proton induced γ -rays are reduced by mean of the PIXE-slits. Additionally the Pb X-rays, emitted from the lead shielding of the HPGe-detector on air, are reduced about one-third. Hence, the PIXE-slits cut the proton beam in diameter.

Regarding the γ -rays of ^{19}F , ^{23}Na and ^{27}Al , they are reduced to 25 %. This proves, that the production inside the beamline, occurs mainly behind the PIXE-slits. Contrary to this, the 846.8 keV γ -line of ^{56}Fe , is more intensive. Thus, the corresponding nuclear reaction is more probable when the H^+ -beam impinges on the PIXE-slits.

4. Background

In table 4.5 the detected γ -rays are listed.

The intensity change of peaks, due to the PIXE-slits, is described in column "comment".

| energy [keV] | reaction | comment |
|--------------|--|--------------------------------|
| 110 197 | $\left. \begin{array}{l} \\ \end{array} \right\} {}^{19}\text{F}(\text{p},\text{p}'\gamma){}^{19}\text{F}$ | reduction: about 65 % |
| 440 | ${}^{23}\text{Na}(\text{p},\text{p}'\gamma){}^{23}\text{Na}$ | reduction: about 75 % |
| 511 | annihilation | reduction: about 30 % |
| 844 | ${}^{27}\text{Al}(\text{p},\text{p}'\gamma){}^{27}\text{Al}$ | overlap: Fe twice as intensive |
| 846.8 | ${}^{56}\text{Fe}(\text{n},\text{n}'\gamma){}^{56}\text{Fe}$ | |
| 1014 | ${}^{27}\text{Al}(\text{p},\text{p}'\gamma){}^{27}\text{Al}$ | almost vanished |
| 1634 | ${}^{23}\text{Na}(\text{p},\alpha\gamma){}^{20}\text{Ne}$ | overlap: reduction: about 75 % |
| 1636 | ${}^{23}\text{Na}(\text{p},\text{p}'\gamma){}^{23}\text{Na}$ | |
| 1779 | ${}^{27}\text{Al}(\text{p},\text{p}'\gamma){}^{27}\text{Al}$ | almost vanished |

Table 4.5.: By energy listed proton induced γ -rays of the "new" PIXE-ART setup with PIXE-slits.

In summary, the PIXE-ART modification provides a substantial reduction of the background and therefore an upgrade of the sensitivity of the PIXE-ART facility. Nevertheless the proton induced background strongly depends on the tuning of the accelerator. A focused and straight-lined proton beam produces less γ -rays inside the beamline. Figure 4.9 shows two "proton on air" PIGE-spectra accumulated on different beam times. The current was about 11 nA in June and 9.5 nA in August.

Regarding the later measurement, the ${}^{23}\text{Na}$ -lines are about a third smaller than in June. Moreover, the γ -rays of ${}^{19}\text{F}$ are hardly visible. This could be due to the lower current in August, but nevertheless the Pb X-rays and the 846.8 keV γ -ray of ${}^{56}\text{Fe}$ are in June almost as high as in August. It seems as if the intensity of the iron peak just depends on the current, whereas the γ -rays of ${}^{23}\text{Na}$ and ${}^{19}\text{F}$ depend on the tuning. From this it follows, that most protons in August pass exactly through the whole construction. Contrary, the proton beam in June hits construction components and therefore produces "background radiation".

Unfortunately, a "good" tuning is not always achievable but from the "protons on air"-PIGE-spectra the background effect of the proton beam can be determined, see chapter 6.

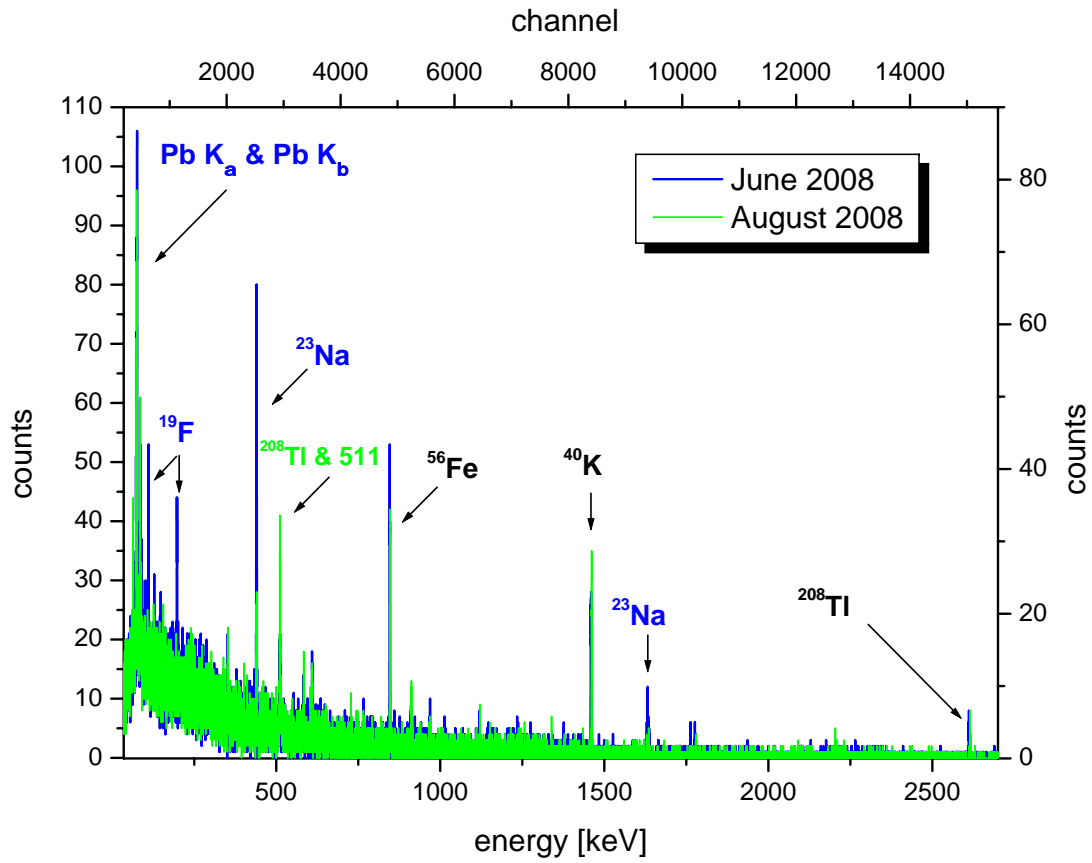


Figure 4.9.: Comparison of a "proton on air" spectrum in June and August. The blue labeled lines are in June more insensitive than in August.

4. *Background*

5. Measurements

In this chapter a complete description of the experimental conditions and their performance is given.

5.1. Experimental conditions

5.1.1. Current measurement

The proton current was measured by moving Faraday cups (FC) in the beam. Illustration 5.1 shows, that the last current measurement was with FC L5, which is arranged in 0.48 m distance to the exit window. Since the beam was collimated after FC L5, there was no possibility to measure the reduced proton fluency before leaving vacuum.

Moreover, dose measurements during irradiation was not feasible.

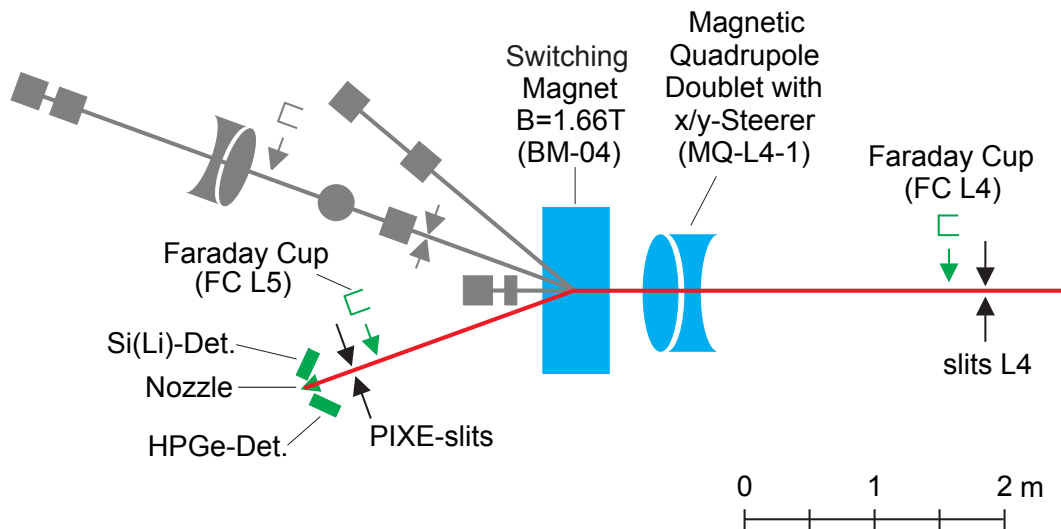


Figure 5.1.: Layout of the PIXE-ART facility at the end of the beamline.

All constituents used for PIGE analysis are colored and labeled. The illustration is true to scale.

Therefore, the proton current in air was measured indirectly.

When 3 MeV protons penetrate air, Ar X-rays are produced due to the argon content in air of about 0.9 %. The number of argon counts in every accumulated X-ray spectrum is related to the protons in air, which provides a good method to calibrate the proton current. Nevertheless, the argon count rate depends on the size of the sample and on the distance to the PIXE detector. Thus, it is necessary to assure the same geometry for targets during a sequence of measurements.

At PIXE-ART, each PIGE measurement was accompanied by a PIXE measurement.

A typical "proton on air" PIXE spectrum with Ar K_α at 2.96 keV and Ar K_β at 3.19 keV is shown in figure 5.2. The correlation between the Ar counts and the current in FC L5 is discussed in chapter 6.

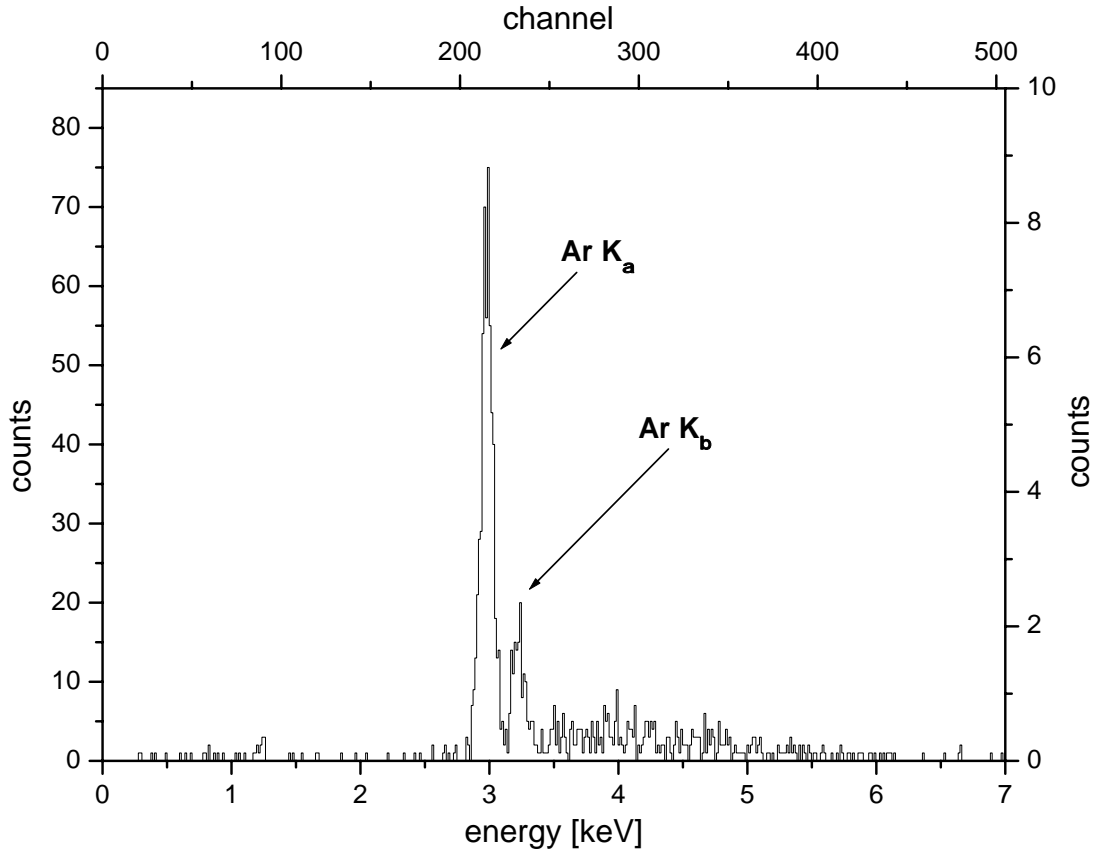


Figure 5.2.: A typical PIXE spectrum of 3 MeV protons in air without sample. Ionization of air leads to Ar K_α and Ar K_β X-rays.

5.1.2. Samples

To determine the sensitivity of the PIGE method, samples with known chemical concentrations were examined. Therefore, three types of target materials were irradiated: metrological standards, glass standards and light element-iron-mixtures.

Due to our cooperation with Silke Merchel, we could analyze samples of certified metrological standards. Some of these pulverized reference materials contain fluorine, aluminum (Al_2O_3) and sodium (Na_2O). In table 5.1 the element concentrations are tabulated, for detailed chemical composition see appendix C.

| | standard | | | |
|---------|--------------------------------|------------------------------|-------------------------------------|--------------------------------|
| element | Opal Glass NBS 91 [mg/g] | Fly Ash BCR 038 [mg/g] | Phosphate Rock BCR 032 [mg/g] | Iron Ore EZRM 681 [mg/g] |
| Al | 31.80 | - | 2.91 | 56.2 |
| F | 57.30 | - | 40.40 | 1.94 |
| Na | 41.44 | 3.74 | - | 0.68 |

Table 5.1.: Al, F and Na concentrations of metrological standards.

For experimental examination a few gramme of each powder were pressed into a target holder with 2 mm diameter. A photograph of a prepared sample is shown in figure 5.3.



Figure 5.3.: Photograph of a target holder containing pulverized standard material.

The investigation of glass standards, used at Academy of Fine Arts Vienna, was possible with help from M. Schreiner. All examined glass samples contain sodium (Na_2O_3). The sodium concentrations and the corresponding mass percentages of the sodium-oxides are summarized in table 5.2.

5. Measurements

| standard | Na ₂ O ₃ [w%] | Na [mg/g] |
|-----------|-------------------------------------|-----------|
| NIST 610 | 14.00 | 68.5 |
| NIST 620 | 14.39 | 70.4 |
| NIST 1830 | 13.75 | 65.2 |
| NIST 1831 | 13.32 | 67.3 |
| Danone N1 | 13.28 | 65.0 |
| Danone N2 | 13.25 | 64.8 |
| Danone N3 | 12.71 | 62.2 |
| Danone N4 | 12.85 | 62.9 |

Table 5.2.: Glass standards from Academy of Fine Arts Vienna. Na concentrations and mass percentages of the Na-oxides are indicated.

As shown in figure 5.4, the glass samples are melted down in bars, hence irradiation without preparation was possible.

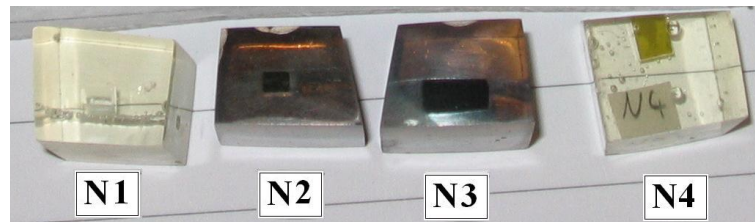


Figure 5.4.: Photograph of the Danone glass standards from the Academy of Fine Arts Vienna. The Danone samples are labeled from N1 to N4.

Samples with other light elements combined with elements from the standards were produced at our laboratory to get more informations about the sensitivity of the PIGE analysis.

Therefore, aluminum oxide (Al_2O_3), boric acid (H_3BO_3) and LiF were chosen as pulverized target materials. Different concentrations of those samples mixed with iron powder were pressed into target holders as mentioned above. All produced mixtures are listed in table 5.3 .

| mixture | labeling | molecule [w%] | element [mg/g] | |
|-------------------------------------|-------------------------------------|--------------------------------|----------------|--------|
| | | LiF | F | Li |
| LiF - Fe | 100% LiF | 100 | 732.40 | 267.60 |
| | 50% LiF | 49.92 | 365.50 | 133.54 |
| | 5% LiF | 4.94 | 36.24 | 13.27 |
| | 1% LiF | 0.99 | 7.29 | 2.64 |
| | | H ₃ BO ₃ | B | |
| H ₃ BO ₃ - Fe | 100% H ₃ BO ₃ | 100 | 174.84 | |
| | 60% H ₃ BO ₃ | 60.02 | 107.39 | |
| | 30% H ₃ BO ₃ | 29.99 | 52.45 | |
| | 6% H ₃ BO ₃ | 6.00 | 10.48 | |
| | | Al ₂ O ₃ | Al | |
| Al ₂ O ₃ - Fe | 100% Al ₂ O ₃ | 100 | 529.25 | |
| | 50% Al ₂ O ₃ | 50.01 | 264.66 | |
| | 10% Al ₂ O ₃ | 9.90 | 52.44 | |
| | 5% Al ₂ O ₃ | 4.49 | 23.82 | |

Table 5.3.: Mixtures of light elements with iron. Molecule concentrations are listed in the middle column, element concentrations in the right column.

5.1.3. Detector efficiency

The relative and absolute detector efficiency were determined due to two calibrated radioactive sources of ¹⁵²Eu and ¹³⁷Cs, placed at target position.

Relative efficiency

To ascertain the relative efficiency of the HPGe detector, a ¹⁵²Eu source was used.

After the determination of the peak areas, a , the relative efficiency ϵ_{rel} was calculated by using the emission probability per decay (P_γ) by mean of IAEA data table [IAEA, 2007]:

$$\epsilon_{rel} = \frac{aP_{\gamma,ref}}{a_{ref}P_\gamma} \quad (5.1)$$

5. Measurements

As reference line the 121.78 keV line was chosen due to the highest emission probability. a_{ref} is the corresponding peak area and $P_{\gamma,ref}$ the emission probability per decay.

The uncertainty of the peak area was derived from the counting statistics and was estimated by different background fits with WIRUK. To calculate the uncertainty of ϵ_{rel} , the law of uncertainty propagation was applied:

$$\sigma_{u(x,y)} = \sqrt{\left(\frac{\partial u}{\partial x}\right)^2 \sigma_x^2 + \left(\frac{\partial u}{\partial y}\right)^2 \sigma_y^2} \quad (5.2)$$

The calculated results consider the uncertainty of the 121.78 keV normalization line. The data used for evaluation are listed in table 5.4.

| E_γ [keV] | P_γ | P.A. [counts] | ϵ_{rel} |
|------------------|-----------------------|-----------------------|--------------------|
| 121.7817 | 0.28410 \pm 0.00130 | 37651.9 \pm 2086.29 | 1 |
| 244.6974 | 0.07550 \pm 0.00040 | 5828.6 \pm 672.66 | 0.583 \pm 0.074 |
| 344.2785 | 0.26580 \pm 0.00120 | 15260.9 \pm 1654.79 | 0.433 \pm 0.052 |
| 411.1165 | 0.02240 \pm 0.00010 | 1013.1 \pm 195.97 | 0.342 \pm 0.068 |
| 443.9650 | 0.03125 \pm 0.00013 | 1252.8 \pm 236.02 | 0.302 \pm 0.059 |
| 778.9045 | 0.12960 \pm 0.00060 | 3408.0 \pm 405.90 | 0.1980 \pm 0.026 |
| 867.3800 | 0.04241 \pm 0.00023 | 971.0 \pm 184.65 | 0.173 \pm 0.034 |
| 964.0720 | 0.14620 \pm 0.00060 | 3264.1 \pm 386.91 | 0.168 \pm 0.022 |
| 1085.8370 | 0.10130 \pm 0.00060 | 2201.5 \pm 270.75 | 0.164 \pm 0.022 |
| 1089.7370 | 0.01730 \pm 0.00010 | 360.8 \pm 79.12 | 0.157 \pm 0.035 |
| 1112.0760 | 0.13400 \pm 0.00060 | 2748.7 \pm 331.67 | 0.155 \pm 0.021 |
| 1212.9480 | 0.01415 \pm 0.00009 | 264.3 \pm 66.15 | 0.141 \pm 0.036 |
| 1299.1420 | 0.01632 \pm 0.00009 | 293.1 \pm 65.17 | 0.136 \pm 0.031 |
| 1408.0130 | 0.20850 \pm 0.00090 | 3349.2 \pm 561.08 | 0.121 \pm 0.021 |

Table 5.4.: The γ -decay lines of a ^{152}Eu source, the determined peak area (P.A.) and the calculated relative efficiency with corresponding uncertainties. E_γ is the γ -energy and P_γ is the emission probability per decay.

Figure 5.5 shows the exponential decrease of the relative efficiency with increasing γ -ray energy. The data from the corresponding fit is given in the inserts.

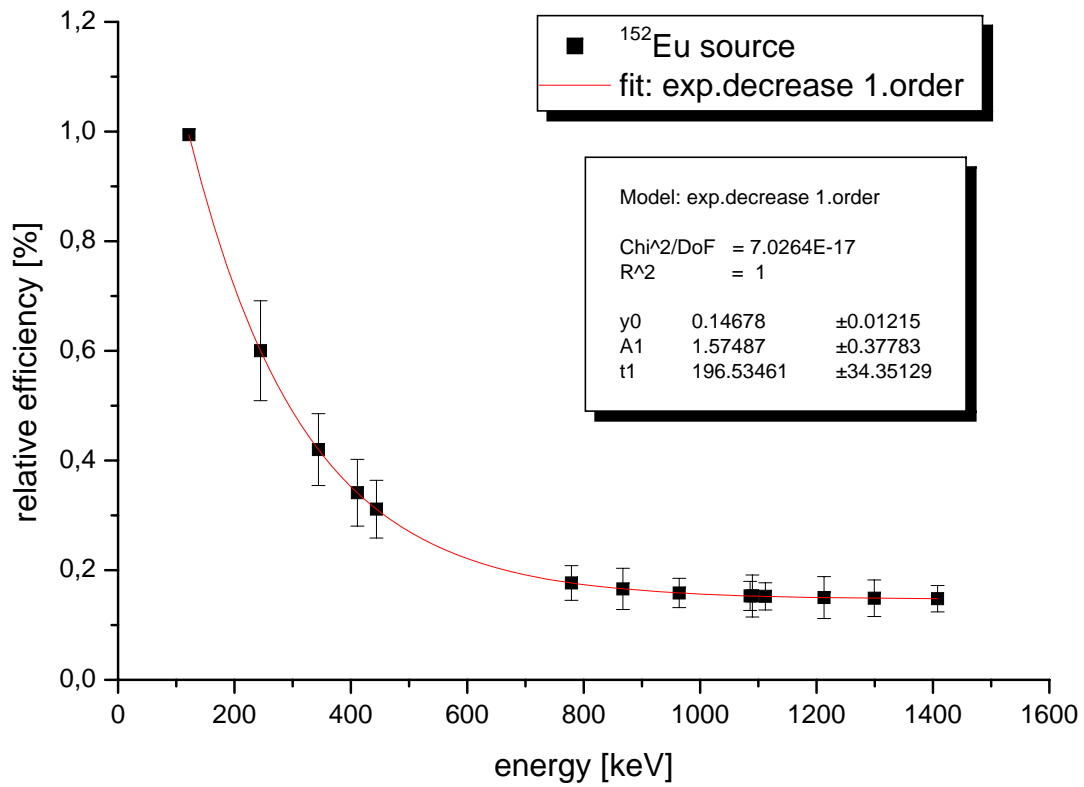


Figure 5.5.: Relative efficiency as a function of ^{152}Eu γ -ray energy.

Absolute efficiency

To determine the absolute efficiency ϵ_{abs} of the HPGe detector, a ^{137}Cs source with known activity A was used.

At the moment of measurement A was $4.88 \pm 0.18 \mu\text{Ci}$ ($= 1.8 \pm 0.06 \cdot 10^5 \text{ Bq}$). The measured peak area was $a = 538407.8 \pm 54578 \text{ cts}$ for the 661.6 keV line and the emission probability was estimated $P_{\gamma, Cs} = 85.1 \pm 0.01 \%$.

The absolute efficiency is defined as count rate $\frac{a}{t}$ per emitted photon (i.e. $A P_{\gamma}$). With the following formula

$$\epsilon_{abs} = \frac{a}{tAP_{\gamma, Cs}} \quad (5.3)$$

the absolute efficiency for the ^{137}Cs source can be calculated as $0.00292 \pm 0.00031\%$. Related to this value, the absolute efficiency curve can be determined. The results are listed in table 5.5.

| $E_{\gamma} [\text{keV}]$ | $\epsilon_{abs} [\%]$ |
|---------------------------|-----------------------|
| 121.7817 | 0.0144 ± 0.0011 |
| 244.6974 | 0.0087 ± 0.0010 |
| 344.2785 | 0.0061 ± 0.0007 |
| 411.1165 | 0.0049 ± 0.0010 |
| 443.9650 | 0.0045 ± 0.0009 |
| 661.6570 | 0.0029 ± 0.0003 |
| 778.9045 | 0.0025 ± 0.0004 |
| 867.3800 | 0.0024 ± 0.0005 |
| 964.0720 | 0.0023 ± 0.0003 |
| 1085.8370 | 0.0022 ± 0.0003 |
| 1089.7370 | 0.0022 ± 0.0005 |
| 1112.0760 | 0.0022 ± 0.0003 |
| 1212.9480 | 0.0022 ± 0.0005 |
| 1299.1420 | 0.0021 ± 0.0004 |
| 1408.0130 | 0.0021 ± 0.0003 |

Table 5.5.: Calculated absolute efficiency.

Figure 5.6 illustrates the energy dependence of the absolute efficiency, related to 661.6 keV γ -peak of ^{137}Cs . The data from an exponential fit is given in the inserts.

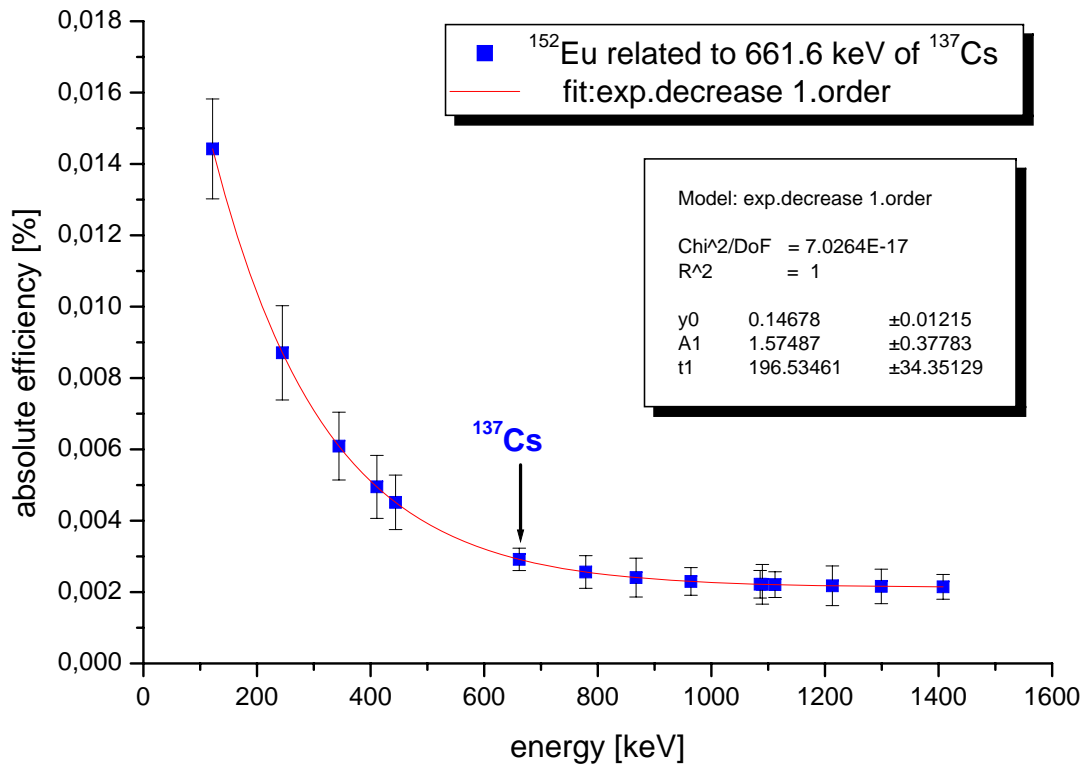


Figure 5.6.: Absolute efficiency as a function of ^{152}Eu γ -ray energy. The curve is evaluated to 661.6 keV γ -peak of ^{137}Cs .

Beamtime 080630 and beamtime 080702 were performed with the same tuning, while measurement of beamtime 080808 used an other tuning. Therefore, beamtime data are summarized in separate tables. June and July data are summarized in table 5.6 and August data in table 5.7.

| beamtime | no. | target | gain | FC L5 [nA] | Ar K $_{\alpha}$ [counts] | comment |
|----------|-----|-------------------------------------|------|----------------|---------------------------|---------|
| 080808 | 1 | background | 10 | | | |
| 080808 | 2 | p on air | 28 | 9.2 ± 1.38 | 202.3 ± 15.2 | |
| 080808 | 3 | p on air | 10 | 9.2 ± 1.38 | 200.3 ± 15.3 | |
| 080808 | 4 | 100% LiF | 28 | 8.2 ± 1.23 | 56.0 ± 9.03 | |
| 080808 | 5 | 50% LiF | 28 | 8.3 ± 1.24 | 63.3 ± 10.6 | |
| 080808 | 6 | 5% LiF | 28 | 8.3 ± 1.24 | 66.1 ± 12.0 | |
| 080808 | 7 | 1% LiF | 28 | 8.1 ± 1.22 | 46.7 ± 10.2 | |
| 080808 | 8 | NBS 91 | 28 | 8.1 ± 1.22 | 61.1 ± 10.4 | |
| 080808 | 9 | 100% H ₃ BO ₃ | 28 | 7.7 ± 1.15 | 54.4 ± 9.0 | |
| 080808 | 10 | 60% H ₃ BO ₃ | 28 | 7.6 ± 1.14 | 46.1 ± 8.9 | |
| 080808 | 11 | 30% H ₃ BO ₃ | 28 | 7.6 ± 1.14 | 66.5 ± 11.0 | |
| 080808 | 12 | 6% H ₃ BO ₃ | 28 | 7.8 ± 1.16 | 75.6 ± 11.3 | |
| 080808 | 13 | 100% Al ₂ O ₃ | 28 | 7.4 ± 1.11 | 44.2 ± 9.2 | |
| 080808 | 13 | 50% Al ₂ O ₃ | 28 | 8.3 ± 1.25 | 66.7 ± 10.3 | |
| 080808 | 15 | 10% Al ₂ O ₃ | 28 | 8.2 ± 1.23 | 68 ± 11.4 | |
| 080808 | 16 | 5% Al ₂ O ₃ | 28 | 7.7 ± 1.15 | 77.5 ± 12.4 | |

Table 5.7.: List no.2 of irradiated samples at beamtime 080808, performed with an other tuning.

To examine different energy regions of the PIGE spectrum, the amplification of the detector was varied. With "gain 28" γ -rays up to 3 MeV can be observed whereas "gain 10" ranges up to 6 MeV. Most PIGE spectra were accumulated with "gain 28".

Current was measured after each irradiation by means of FC L5. The current uncertainty, is determined as 15 % of each single current measurement, due to current fluctuations. All irradiations were accompanied by a PIXE measurement of the Ar K $_{\alpha}$ X-ray. The uncertainty of the acquired peak area derives from counting statistics. The count rate of Ar K $_{\alpha}$ during beamtime 080808 is lower, because the Si(Li) detector was positioned at a position farther away.

During all experiments with glass standards (beamtime 080702), the proton current was kept low to avoid visible beam damages.

The γ -ray spectra of protons on air without samples are marked "p on air", background accumulations with "background".

Furthermore, additional notes are entered in column "comments". In case of untypical high current fluctuations, it is labeled "fluctuations". Measurements performed without PIXE-slits are marked "no slits".

5.2.1. Energy calibration

The energy scale was calibrated (figure 5.7) by the background lines ^{40}K and ^{208}Tl (table 5.8), after the linearity was checked with a ^{152}Eu source.

| element | energy [keV] | channel |
|-------------------|--------------|---------|
| ^{40}K | 1460.8 | 8405 |
| ^{208}Tl | 2614.5 | 15051 |

Table 5.8.: Energy and channel number of ^{40}K and ^{208}Tl used for energy calibration.

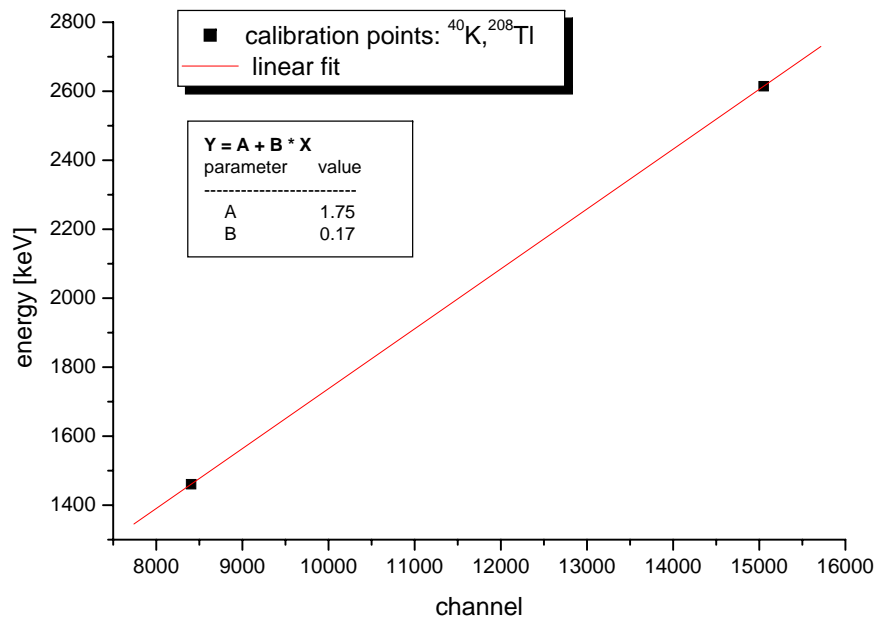


Figure 5.7.: Linear fit of the data points ^{40}K and ^{208}Tl used for energy calibration.

5.2.2. PIGE spectra

Typical PIGE spectra for referent materials containing all analyzed elements (Li, F, Al, Na, B) are shown in figures 5.11 to 5.8.

In most cases they are compared with a "proton on air" spectrum without target.

In figure 5.8 a characteristic γ -ray spectrum of a sample containing sodium is compared with a spectrum without target material. As sample, the glass standard NIST 620 with a sodium concentration of 7 % was irradiated. The ^{23}Na γ -ray lines at 440 keV and 1634 keV/1636 keV are clearly visible.

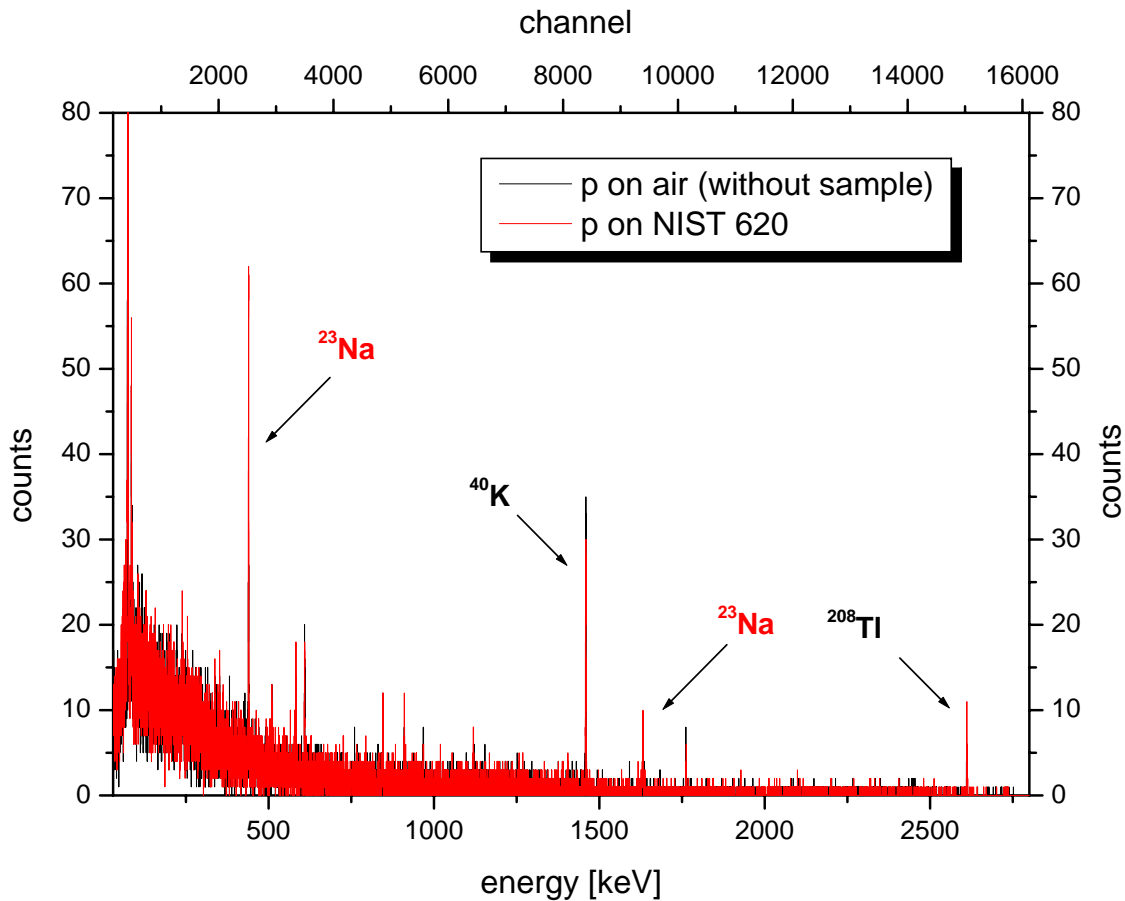


Figure 5.8.: Typical PIGE spectrum for a sample containing sodium. Both ^{23}Na γ -rays at 440 keV and 1634 keV/1636 keV are visible.

The γ -rays of ^{56}Fe at 846.8 keV and ^{27}Al at 844 keV are overlapping. By using a higher conversion gain, these peaks can be seen separately.

In figure 5.9 the relevant part of a spectrum for a sample composed of 100% Al_2O_3 is compared with a spectrum without target material. The ^{27}Al γ -ray peak just appears in the spectrum for the aluminum oxide sample.

Moreover, a ^{56}Fe peak with equal intensity can be resolved in both spectra.

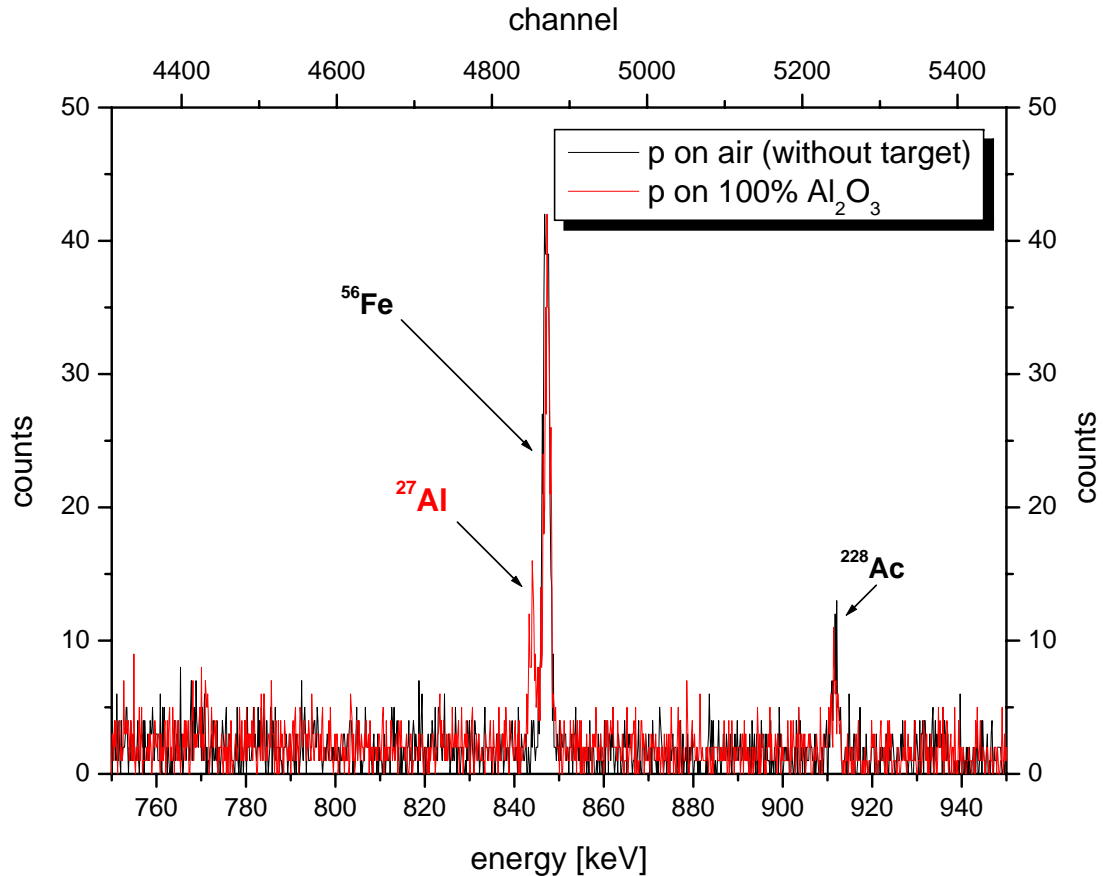


Figure 5.9.: Detailed illustration of a PIGE spectrum for a sample containing aluminum (red lines) compared with a "proton on air" spectrum without sample (black lines). The plot shows the peaks of the 846.8 keV (^{56}Fe) and 844 keV (^{27}Al) γ -rays well separated.

The emitted γ -ray line of the light isotope ^{10}B is Doppler shifted as a result of recoil motion of the nucleus caused by the proton bombardment and the subsequent deceleration in the target material.

To visualize the broadened peak, adjusted channels were summarized. For this reason, the B-spectrum is displayed in detail with PMCA, a program used for the data acquisition.

Figure 5.10 shows a detailed PMCA layout of a PIGE spectrum for a sample consisting of 100 % H_3BO_3 . The Doppler shifted γ -line at 429 keV is denoted green. This phenomenon was also corroborated from our contact Christian Neelmeijer.

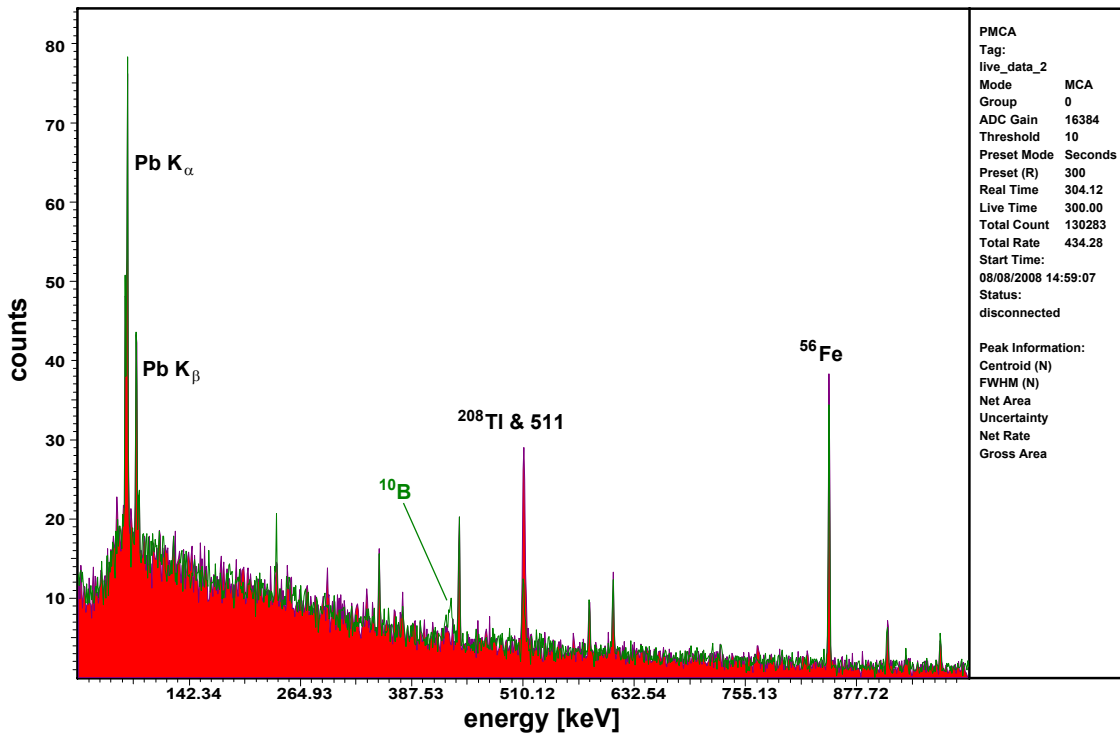


Figure 5.10.: Detailed illustration of a PIGE spectrum, accumulated with PMCA, for a sample containing boron, see text. The Doppler shifted γ -ray of ^{10}B at 429 keV is labeled green. In the right column, measurement data are indicated.

Figure 5.11 shows the PIGE spectrum of 100 % LiF.

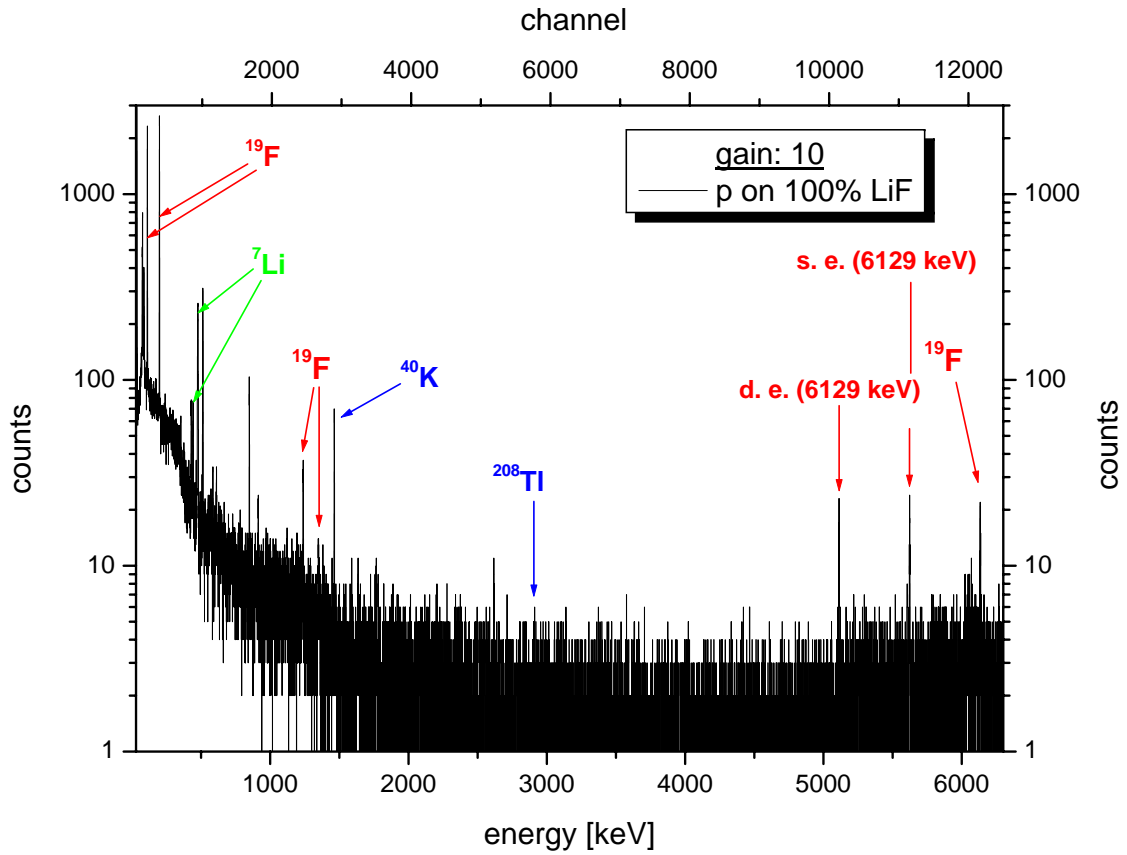


Figure 5.11.: Spectrum acquired with "gain10" for a matrix composed of lithium and fluorine. The ^{19}F γ -ray lines are labeled in red, the ^7Li γ -ray lines are labeled in green, calibration lines are indicated blue.

By using a gain factor of 10, the 6.1 MeV γ -ray and furthermore its escape and double escape peak can be seen, while for a higher amplification these lines are beyond the range of the ADC. are produced.

All expected nuclear reactions are listed in table 5.9.

Contrary to the proton induced background spectra, the 1236 keV and 1357 keV γ -rays are now visible due to the high fluorine concentration.

| element | reaction | E_γ [keV] |
|---------|---|------------------|
| Li | ${}^7\text{Li}(\text{p}, \text{n}\gamma){}^7\text{Be}$ | 429 |
| | ${}^7\text{Li}(\text{p}, \text{p}'\gamma){}^7\text{Li}$ | 478 |
| F | ${}^{19}\text{F}(\text{p}, \text{p}'\gamma){}^{19}\text{F}$ } | 110 |
| | | 197 |
| | | 1236 |
| | | 1357 |
| | ${}^{19}\text{F}(\text{p}, \alpha\gamma){}^{16}\text{O}$ | 6129 |

Table 5.9.: Typical nuclear reactions and the emitted γ -ray-energies of ${}^7\text{Li}$ and ${}^{19}\text{F}$ used in PIGE analysis.

6. Experimental Results

6.1. Current calibration and background correction

6.1.1. Correlation of Ar counts with current in FC L5

Data from "proton on air" spectra of beamtime 080702 were used to investigate the relation between the acquired Ar K_α counts in the X-ray detector and the current in FC L5. These data as well as the 846.8 keV line of ^{56}Fe are summarized in table 6.1. The ^{56}Fe γ -line is supposed to be representative from the total proton current, because the sources of the γ -rays are in the PIXE-slits closed behind FC L5.

| no. | FC L5 [nA] | Ar K_α [counts] | ^{56}Fe P.A. [counts] |
|-----|-----------------|------------------------|--------------------------------|
| 18 | 2.0 ± 0.30 | 268.4 ± 17.5 | 73.6 ± 10.9 |
| 19 | 4.3 ± 0.65 | 346.4 ± 19.8 | 178.7 ± 16.8 |
| 25 | 7.25 ± 1.09 | 548.0 ± 25.0 | 342 ± 22.5 |
| 58 | 0.85 ± 0.13 | 156.5 ± 13.4 | 44.7 ± 12.4 |
| 69 | 0.80 ± 0.12 | 137.2 ± 12.5 | 24.5 ± 11.0 |

Table 6.1.: Current data and acquired counts of Ar K_α and ^{56}Fe listed by number. Data points are taken from beamtime 080702.

Figure 6.1 shows no linear correlation of Ar K_α counts and the current measured in FC L5. The uncertainties for the current in FC L5 are assumed to be 15 %, the uncertainties for the peak areas are derived from counting statistics.

Contrary to this, the data points of ^{56}Fe are proportional to the current in FC L5, which can be seen in figure 6.2.

The beam diameter dilates with the proton current. While the main part of the proton beam hits the PIXE-slits, the relative number of protons which pass the slits and the nozzle decreases with increasing proton current. The amount of the decrease depends strongly on the tuning. Therefore, the Ar K_α counts do not rise linearly with the proton beam.

Unfortunately the nonlinearity of Ar K_α counts versus the current in FC L5 is even noticeable with a "good" tuning. As a consequence, the proton current in air can not be determined by using FC L5.

6. Experimental Results

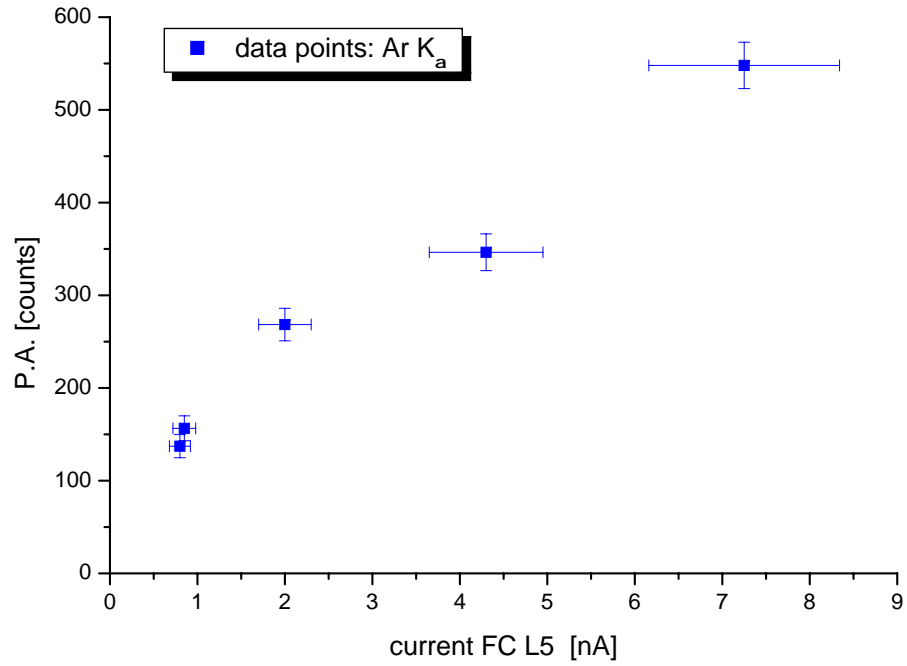


Figure 6.1.: Ar K_α peak area as versus current measured in FC L5. Data points are taken from beamtime 080702.

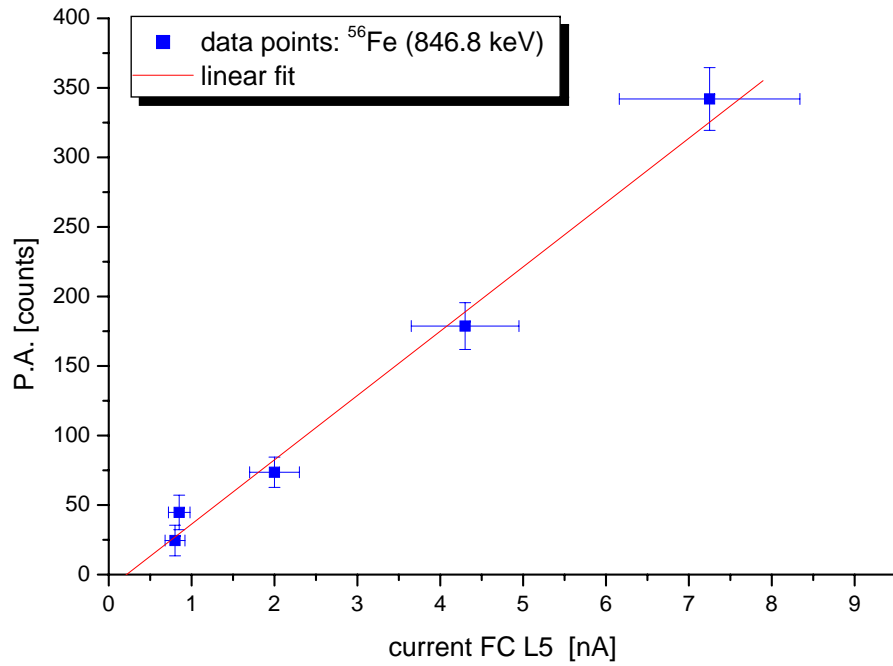


Figure 6.2.: Peak area of the ⁵⁶Fe 846.8 keV line versus current measured in FC L5. Data points are taken from beamtime 080702.

6.1.2. Background correction

The observed γ -peaks were normalized to the Ar K_α counts since no direct current measurement for a proton beam in air was possible.

The proton induced background had to be considered before a calibration for the ^{19}F , ^{23}Na and ^{27}Al peaks can be done. A linear correlation between the peak areas of these γ -lines and the current in FC L5 was observed because they are also produced inside the beamline.

For better statistics, the lines with highest count rates were examined. In particular, the 110 keV line for ^{19}F , the 440 keV line for ^{23}Na and the 1014 keV line for ^{27}Al .

The procedure for the background correction is demonstrated on the specific case of ^{23}Na .

The "proton on air" measurements of beamtime 080702 were again used to plot the current in FC L5 versus the peak area of the 440 keV line. All used values are summarized in a table at the end of the chapter.

To account for the possibility of a natural background, relevant peak areas of the background spectrum were determined and used for correction.

A linear fit weighted by the uncertainties of the peak area (P.A.) is shown in figure 6.3. Because zero current produces zero counts and the origin is within the ordinate intercept, the fit was forced through zero. The fit is shown in figure 6.3. Because zero current produces zero counts and the origin is within the ordinate intercept, the fit was forced through zero.

The uncertainties of the fit parameters given in the inserts of figure 6.3 consider only the uncertainties in the peak areas, which have to be enlarged to account on the uncertainties in the current. This can be done by using the linear correlation fit, $P.A._{fit} = B \cdot I$, between the current I and the peak area $P.A._{fit}$:

$$\sigma_{P.A.,fit} = \sqrt{(B \cdot \sigma_I)^2 + (I \cdot \sigma_B)^2} \quad (6.1)$$

with B as the slope of the line and σ_B and σ_I as the corresponding uncertainties which were derived from counting statistics.

Therefore, the overall uncertainty, $\sigma_{P.A.,total}$, of the peak area can be evaluated as follows:

$$\sigma_{P.A.,total} = \sqrt{(\sigma_{P.A.,fit})^2 + (\sigma_{P.A.})^2} \quad (6.2)$$

Since the acquired peak areas and the proton current are independently measured quantities, the uncertainties were added square.

The modified linear fit can be seen in figure 6.4 with the newly-calculated slope and its uncertainty in the inserts.

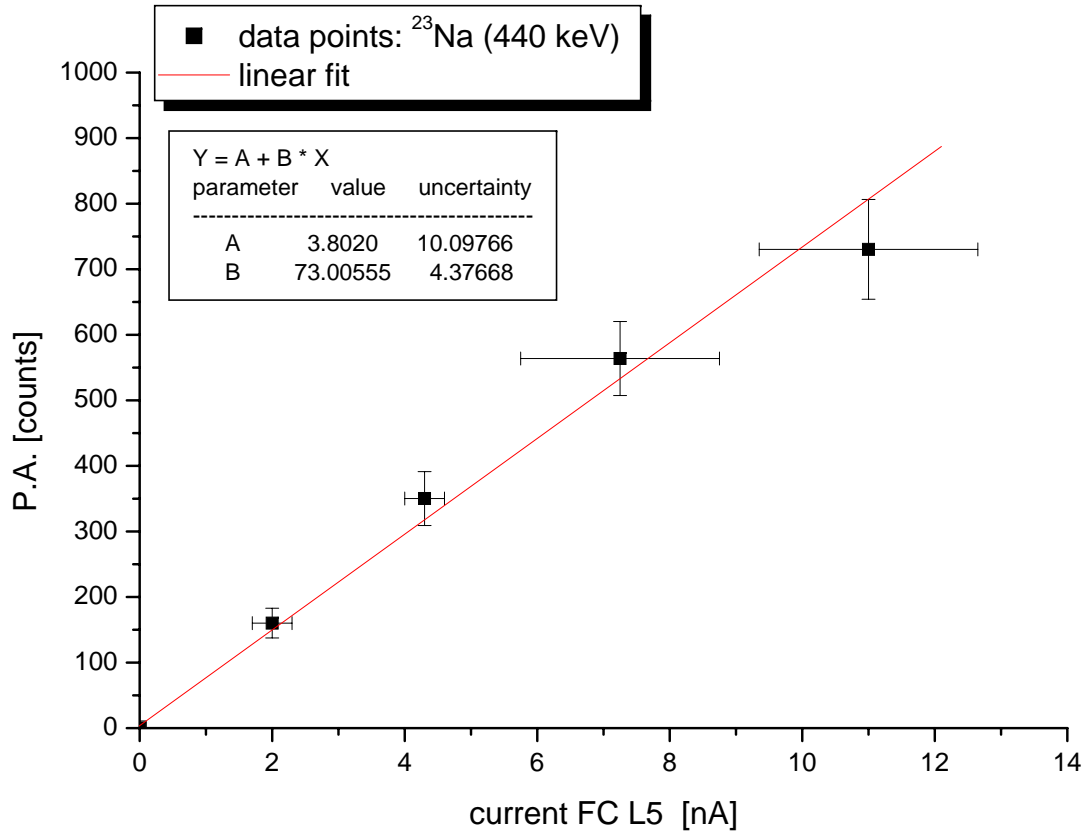


Figure 6.3.: Peak area of the 440 keV line (^{23}Na) versus the current measured in FC L5.

The same procedure was repeated for ^{19}F and ^{27}Al . The calibrations curves can be seen in figure 6.5 and figure 6.6. The data of the linear fits are given in the inserts.

Due to the evaluated linear fits any proton induced background peak area of ^{19}F , ^{23}Na and ^{27}Al can be calculated from known current. The subtraction of these "background" counts from those of the accumulated PIGE spectrum provides the net peak area, i.e. the "real" number of counts produced through proton-sample-interactions. Afterwards the net peak areas were normalized to the Ar K_α counts.

For peak which do not appear in the proton induced background, no background subtraction is needed. In these cases the peak areas were directly normalized to the Ar K_α counts (e.g. lithium and boron).

The background correction for F, Na and Al were not necessary for beamtime 080808 because the peak areas were negligible small as can be seen in figure 4.9. During this beamtime the proton current could be kept very constant at 8 nA too.

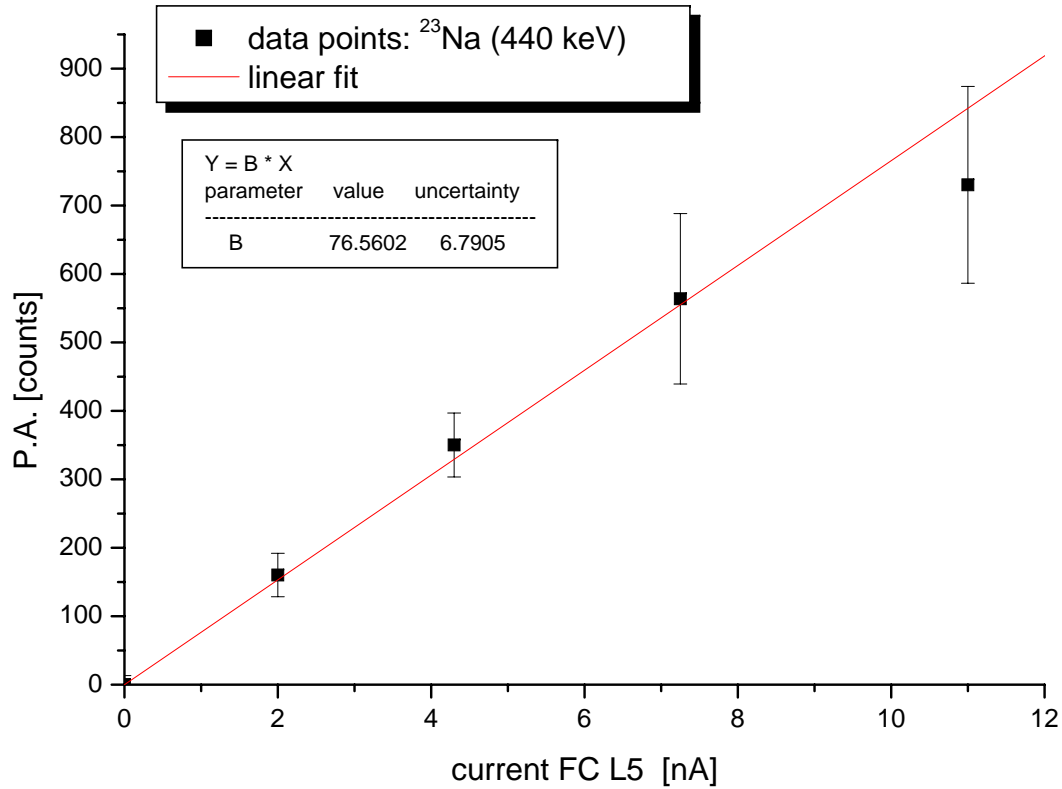


Figure 6.4.: Final fit for background correction for ^{23}Na . The plot shows the peak area of the 440 keV line versus current measured in FC L5.

In the following the results are summarized in table 6.2 to table 6.5 ordered by elements and beamtimes. The peak areas of the accumulated PIGE spectra are marked "gross". "P.A. back" means the calculated proton induced background deduced from the final fit for background correction and "P.A. net" = "P.A. gross" - "P.A. back". The net peak areas normalized to Ar K_{α} counts are indicated "P.A./Ar".

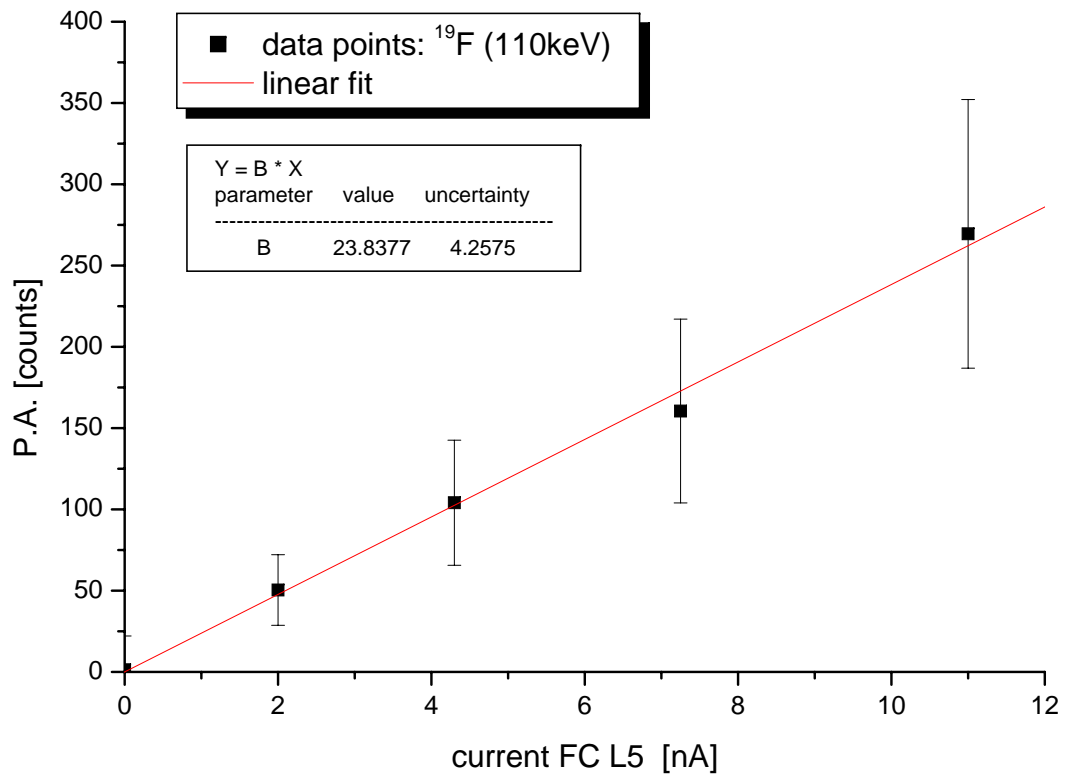


Figure 6.5.: Final fit for background correction for fluorine. The illustration shows the peak area of the 110 keV line versus current measured in FC L5.

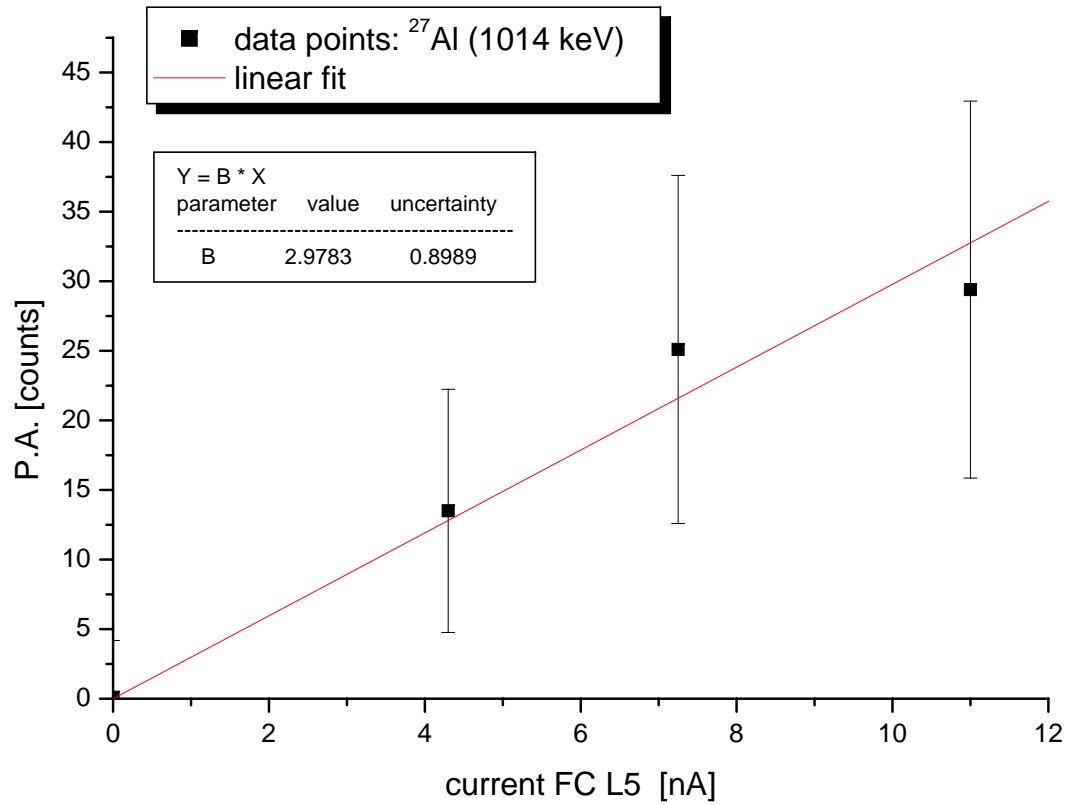


Figure 6.6.: Final fit for background correction for aluminum. The plot shows the peak area of the 1014 keV line versus current measured in FC L5.

6. Experimental Results

| F | | | | | | | |
|--------|----------|------------------------|---------------|-----------------------|----------------------|---------------------------|---------------------|
| July | | | | | | | |
| no | target | P.A. gross [counts] | FC L5 [nA] | P.A. back [counts] | P.A. net [counts] | Ar K α [counts] | P.A./Ar [counts] |
| 2 | NBS 91 | 1791.6 \pm 142.0 | 10 \pm 1.5 | 235.7 \pm 55.6 | 1555.9 \pm 152.4 | 189.7 \pm 16.0 | 8.18 \pm 1.06 |
| 3 | NBS 91 | 1488.2 \pm 123.4 | 9 \pm 1.4 | 212.4 \pm 50.0 | 1275.8 \pm 133.2 | 168.6 \pm 14.3 | 7.57 \pm 1.02 |
| 6 | BCR 32 | 1864.2 \pm 145.3 | 12 \pm 1.8 | 282.4 \pm 66.7 | 1581.7 \pm 159.9 | 363.7 \pm 22.3 | 4.43 \pm 0.51 |
| 7 | BCR 32 | 1744.1 \pm 136.5 | 14 \pm 2.1 | 329.2 \pm 77.8 | 1388.3 \pm 157.1 | 327.0 \pm 22.4 | 4.32 \pm 0.56 |
| 8 | ERZM 681 | 244.0 \pm 4.8 | 9 \pm 1.4 | 212.4 \pm 50.0 | 31.6 \pm 50.3 | 206.0 \pm 18.3 | 0.15 \pm 0.24 |
| 9 | ERZM 681 | 244.0 \pm 7.1 | 10 \pm 1.5 | 235.7 \pm 55.6 | 8.3 \pm 56.0 | 149.5 \pm 15.2 | 0.06 \pm 0.37 |
| August | | | | | | | |
| no | target | P.A. gross [counts] | FC L5 [nA] | P.A. back [counts] | P.A. net [counts] | Ar K α [counts] | P.A./Ar [counts] |
| 4 | 100% LiF | 7485.3 \pm 467.2 | | | 7485.3 \pm 467.2 | 56 \pm 9.0 | 133.67 \pm 23.11 |
| 5 | 50% LiF | 4706.2 \pm 310.8 | | | 4706.2 \pm 310.8 | 63.3 \pm 10.6 | 74.35 \pm 13.39 |
| 6 | 5% LiF | 727.8 \pm 148.3 | | | 727.8 \pm 148.3 | 66.1 \pm 12.0 | 11.01 \pm 3.00 |
| 7 | 1% LiF | 124.1 \pm 55.6 | | | 124.1 \pm 55.6 | 46.7 \pm 10.2 | 2.66 \pm 1.32 |
| 8 | NBS 91 | 609.0 \pm 61.1 | | | 609.0 \pm 61.1 | 56.5 \pm 10.4 | 10.78 \pm 2.26 |

Table 6.2.: Summarized data for normalized peak area determination for Fluorine.

| Al | | | | | | | |
|--------|-------------------------------------|------------------------|---------------|-----------------------|----------------------|---------------------------|---------------------|
| July | target | P.A. gross [counts] | FC L5 [nA] | P.A. back [counts] | P.A. net [counts] | Ar K α [counts] | P.A./Ar [counts] |
| no | | | | | | | |
| 2 | NBS 91 | 64.6 \pm 14.4 | 10 \pm 1.5 | 29.3 \pm 10.0 | 35.3 \pm 17.6 | 189.7 \pm 16.8 | 0.19 \pm 0.09 |
| 3 | NBS 91 | 44.5 \pm 13.3 | 9 \pm 1.4 | 26.4 \pm 9.0 | 18.1 \pm 16.1 | 168.6 \pm 15.0 | 0.11 \pm 0.10 |
| 6 | BCR 32 | 42.1 \pm 13.4 | 12 \pm 1.8 | 29.3 \pm 12.0 | 12.8 \pm 18.0 | 363.7 \pm 23.4 | 0.02 \pm 0.05 |
| 7 | BCR 32 | 66.6 \pm 14.1 | 14 \pm 2.1 | 43.8 \pm 14.0 | 22.8 \pm 19.9 | 327.0 \pm 22.4 | 0.08 \pm 0.06 |
| 8 | ERZM 681 | 79.5 \pm 15.7 | 9 \pm 1.4 | 32.2 \pm 9.0 | 47.3 \pm 18.1 | 206.0 \pm 18.3 | 0.26 \pm 0.09 |
| 9 | ERZM 681 | 69.2 \pm 13.9 | 10 \pm 1.5 | 43.8 \pm 10.0 | 25.4 \pm 17.1 | 149.5 \pm 15.2 | 0.27 \pm 0.11 |
| August | | | | | | | |
| no | target | P.A. gross [counts] | FC L5 [nA] | P.A. back [counts] | P.A. net [counts] | Ar K α [counts] | P.A./Ar [counts] |
| 13 | 100% Al ₂ O ₃ | 179.6 \pm 23.7 | | | 179.6 \pm 23.7 | 44.2 \pm 9.2 | 4.06 \pm 1.00 |
| 14 | 50% Al ₂ O ₃ | 117.8 \pm 17.8 | | | 117.8 \pm 17.8 | 66.7 \pm 10.3 | 1.77 \pm 0.38 |
| 15 | 10% Al ₂ O ₃ | 43.0 \pm 10.6 | | | 43.0 \pm 10.6 | 68.0 \pm 11.4 | 0.63 \pm 0.19 |
| 16 | 5% Al ₂ O ₃ | 15.6 \pm 7.5 | | | 15.6 \pm 7.5 | 77.5 \pm 12.4 | 0.20 \pm 0.10 |
| 8 | NBS 91 | 19.6 \pm 7.4 | | | 19.6 \pm 7.4 | 56.5 \pm 10.4 | 0.36 \pm 0.15 |

Table 6.3.: Summarized data for normalized peak area determination for aluminum.

| Na | | | | | | | |
|------|-----------|------------------------|---------------|-----------------------|----------------------|-------------------------------|---------------------|
| July | | | | | | | |
| no | target | P.A. gross [counts] | FC L5 [nA] | P.A. back [counts] | P.A. net [counts] | Ar K _α [counts] | P.A./Ar [counts] |
| 2 | NBS 91 | 1225.0 ± 39.4 | 10 ± 1.5 | 733.9 ± 133.4 | 491.1 ± 139.1 | 189.7 ± 16.8 | 2.59 ± 0.77 |
| 3 | NBS 91 | 1019.0 ± 36.0 | 9 ± 1.4 | 660.9 ± 120.1 | 358.1 ± 125.3 | 168.6 ± 15.0 | 2.12 ± 0.76 |
| 4 | BCR 38 | 532.8 ± 25.4 | 7.0 ± 1.1 | 733.86 ± 93.4 | 201.6 ± 96.7 | 94.0 ± 11.4 | 0.19 ± 1.05 |
| 5 | BCR 38 | 923.0 ± 33.9 | 10.5 ± 1.6 | 770.4 ± 125.9 | 152.6 ± 145.7 | 234.8 ± 18.5 | 0.65 ± 0.62 |
| 13 | NIST 610 | 652.9 ± 60.5 | 2.4 ± 0.4 | 41.9 ± 32.0 | 611.0 ± 68.5 | 97.8 ± 12.2 | 4.21 ± 1.04 |
| 15 | NIST 620 | 573.0 ± 54.7 | 2.7 ± 0.4 | 43.9 ± 36.4 | 529.1 ± 65.6 | 82.5 ± 10.1 | 4.51 ± 1.11 |
| 16 | NIST 1830 | 348.0 ± 38.1 | 2.1 ± 0.3 | 41.9 ± 28.3 | 306.1 ± 47.5 | 60.8 ± 8.5 | 3.14 ± 1.05 |
| 17 | NIST 1831 | 312.2 ± 35.4 | 1.8 ± 0.3 | 36.0 ± 24.1 | 276.2 ± 42.8 | 35.9 ± 6.6 | 3.33 ± 1.85 |
| 18 | Danone N1 | 276.8 ± 33.6 | 1.9 ± 0.3 | 38.0 ± 25.7 | 238.8 ± 42.3 | 37.2 ± 6.6 | 3.61 ± 1.61 |
| 19 | Danone N2 | 312.1 ± 35.7 | 2.4 ± 0.4 | 43.9 ± 27. | 268.2 ± 45.0 | 33.5 ± 6.6 | 3.12 ± 2.07 |
| 20 | Danone N3 | 264.5 ± 32.9 | 1.8 ± 0.3 | 43.9 ± 24.0 | 220.6 ± 40.7 | 45.8 ± 7.6 | 2.82 ± 1.19 |
| 21 | Danone N4 | 244.8 ± 30.1 | 2.0 ± 0.3 | 43.9 ± 26.7 | 200.9 ± 40.2 | 31.2 ± 6.5 | 3.04 ± 1.86 |

Table 6.4.: Summarized data for normalized peak area determination for sodium.

| Li | | | | | | | |
|--------|-------------------------------------|------------------------|---------------|-----------------------|----------------------|---------------------------|---------------------|
| August | | | | | | | |
| no | target | P.A. gross [counts] | FC L5 [nA] | P.A. back [counts] | P.A. net [counts] | Ar K α [counts] | P.A./Ar [counts] |
| 4 | 100% LiF | 2769.7 \pm 196.2 | | | 2769.7 \pm 196.2 | 56 \pm 9.0 | 49.46 \pm 8.04 |
| 5 | 50% LiF | 1845.8 \pm 141.2 | | | 1845.8 \pm 141.2 | 63.3 \pm 10.6 | 29.16 \pm 4.95 |
| 6 | 5% LiF | 281.6 \pm 68.1 | | | 281.6 \pm 68.1 | 66.1 \pm 12.0 | 4.26 \pm 0.87 |
| 7 | 1% LiF | 50 \pm 34.8 | | | 50 \pm 34.8 | 46.7 \pm 10.2 | 1.07 \pm 0.53 |
| B | | | | | | | |
| August | | | | | | | |
| no | target | P.A. gross [counts] | FC L5 [nA] | P.A. back [counts] | P.A. net [counts] | Ar K α [counts] | P.A./Ar [counts] |
| 9 | 100% H ₃ BO ₃ | 55.4 \pm 16.9 | | | 55.4 \pm 16.9 | 54.4 \pm 9.0 | 1.02 \pm 0.35 |
| 10 | 60% H ₃ BO ₃ | 33.2 \pm 15.6 | | | 33.2 \pm 15.6 | 46.1 \pm 8.9 | 0.72 \pm 0.37 |
| 11 | 30% H ₃ BO ₃ | 21.5 \pm 11.6 | | | 21.5 \pm 11.6 | 66.5 \pm 11.0 | 0.32 \pm 0.18 |
| 12 | 6% H ₃ BO ₃ | 6.9 \pm 3.8 | | | 6.9 \pm 3.8 | 75.6 \pm 11.3 | 0.09 \pm 0.05 |

Table 6.5.: Summarized data for normalized peak area determination for lithium and boron.

6.2. Calibration and uncertainties

A calibration line for the elemental concentrations was created by using all available standards applying the background correction as described in the previous chapter. From here on only the net peak areas normalized to the Ar K_α line from the X-ray detection are quoted.

Primarily, only calibration lines for samples from within the same kind of standards (metrological standards, glass standards, light element-iron-mixtures) were determined.

The used samples were similar in size which is required for Ar K_α normalization.

A combination of the July and August measurements was not accomplished due to different distances of the Si(Li) detector and consequently different efficiencies for the Ar K_α line. Therefore, all results are labeled as August (beamtime 080808) or July (beamtime 080702 and 080630) measurements.

6.2.1. Evaluation

The approach to determine the concentration calibration line is demonstrated on the specific case of ^{23}Na .

The normalized peak areas of the 440 keV line are plotted versus the sodium concentrations shown in figure 6.7. The corresponding data are summarized in table 6.6.

| no. | target | concentration [mg/g] | P.A./Ar [counts] |
|-----|----------|-------------------------|---------------------|
| 2 | NBS 91 | 41.44 | 2.59 ± 0.77 |
| 3 | NBS 91 | 41.44 | 2.12 ± 0.76 |
| 4 | BCR 38 | 3.74 | 0.19 ± 1.05 |
| 5 | BCR 38 | 3.74 | 0.65 ± 0.62 |
| 6 | EZRM 681 | 0.68 | - |

Table 6.6.: List of data used for determination of sodium concentrations in metrological standards.

The uncertainties of BCR 38 are relative high due to strong current fluctuations. Unfortunately the sodium concentration in ERZM 681 was too low to be measured.

A linear fit (drawn black) was applied to the data weighted by the inverse of the peak area uncertainties. The fit parameters are indicated in the inserts of the illustration. The fit parameters are indicated in

the inserts of the illustration.

In a second step the fit (drawn red) was forced through the origin due to the fact that the background correction was already performed and the origin is within the uncertainties of the ordinate intercept.

The relative uncertainty of the slope $\frac{\sigma_B}{B}$ is calculated to be 23 %.

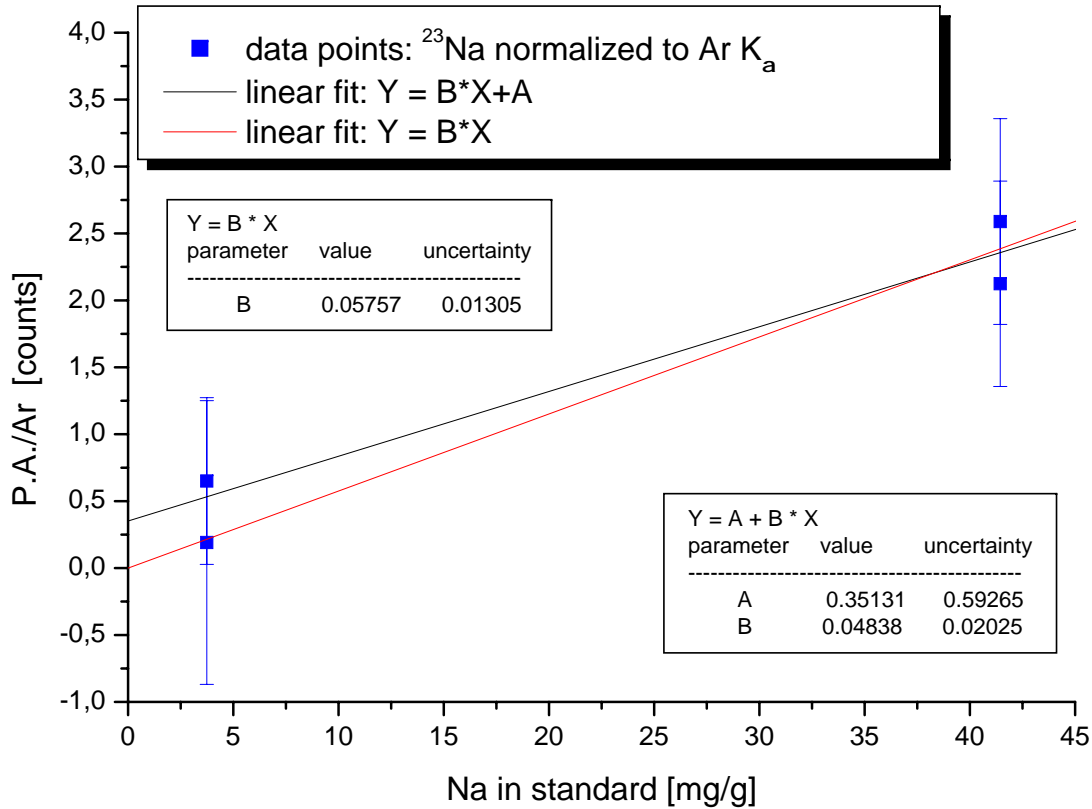


Figure 6.7.: Calibration line for sodium concentrations in metrological samples. The black colored fit is the original fit using the experimental data while the red colored line is the fit forced through the origin. The latter one is used as sodium concentration calibration line with an uncertainty of 23 %.

The ^{23}Na concentration of unknown samples can be determined by using this calibration line.

Generally, unknown concentrations can be calculated, according to the element related calibration line:

$$c_x = B_x \cdot a \quad (6.3)$$

where c_x is the concentration of element x in the sample, B_x is the slope of the calibration line and a is the normalized area of the corresponding γ -peak.

6. Experimental Results

The uncertainty of the evaluated element concentration σ_c is calculated due to the law of uncertainty propagation:

$$\sigma_{c_x} = \sqrt{a^2(\sigma_{B_x})^2 + B_x^2(\sigma_a)^2} \quad (6.4)$$

$$= B_x \sqrt{a^2 \left(\frac{\sigma_{B_x}}{B_x} \right)^2 + (\sigma_a)^2} \quad (6.5)$$

with $\frac{\sigma_{B_x}}{B_x}$ as the relative uncertainty of the slope of the calibration line.

Thus, the relative uncertainty of the element concentration is calculated according to:

$$\frac{\sigma_{c_x}}{c_x} = \sqrt{\left(\frac{\sigma_{B_x}}{B_x} \right)^2 + \left(\frac{\sigma_a}{a} \right)^2} \quad (6.6)$$

The same procedure was applied to all elements as presented below.

6.2.2. Sodium

An other calibration line was obtained for glass standards provided by M. Schreiner.

In figure 6.8 the different peak areas of the 440 keV γ -line are plotted versus the sodium concentrations. The data points are summarized in table 6.7.

The proton current during these measurement was kept below 1 nA to avoid beam spots on the glass standards. In consequence the uncertainties are high due to the low count rate and to current fluctuations.

| no. | target | concentration [mg/g] | P.A./Ar [counts] |
|-----|-----------|-------------------------|---------------------|
| 13 | NIST 610 | 68.5 | 4.21 \pm 1.04 |
| 15 | NIST 620 | 70.4 | 4.51 \pm 1.11 |
| 16 | NIST 1830 | 65.2 | 3.14 \pm 1.05 |
| 17 | NIST 1831 | 67.2 | 3.33 \pm 1.85 |
| 18 | Danone N1 | 65.0 | 3.61 \pm 1.61 |
| 19 | Danone N2 | 64.8 | 3.12 \pm 2.07 |
| 20 | Danone N3 | 62.2 | 2.82 \pm 1.19 |
| 21 | Danone N4 | 62.9 | 3.04 \pm 1.86 |

Table 6.7.: List of data used for determination of sodium concentrations in glass standards.

The fit was forced through the origin. The fit parameters are given in the inserts of the figure.

The relative uncertainty of the calibration line is evaluated to be 13 %. The slope of the calibration line fits within the uncertainties with the slope determined from the metrological samples NBS 91 and BCR 38.

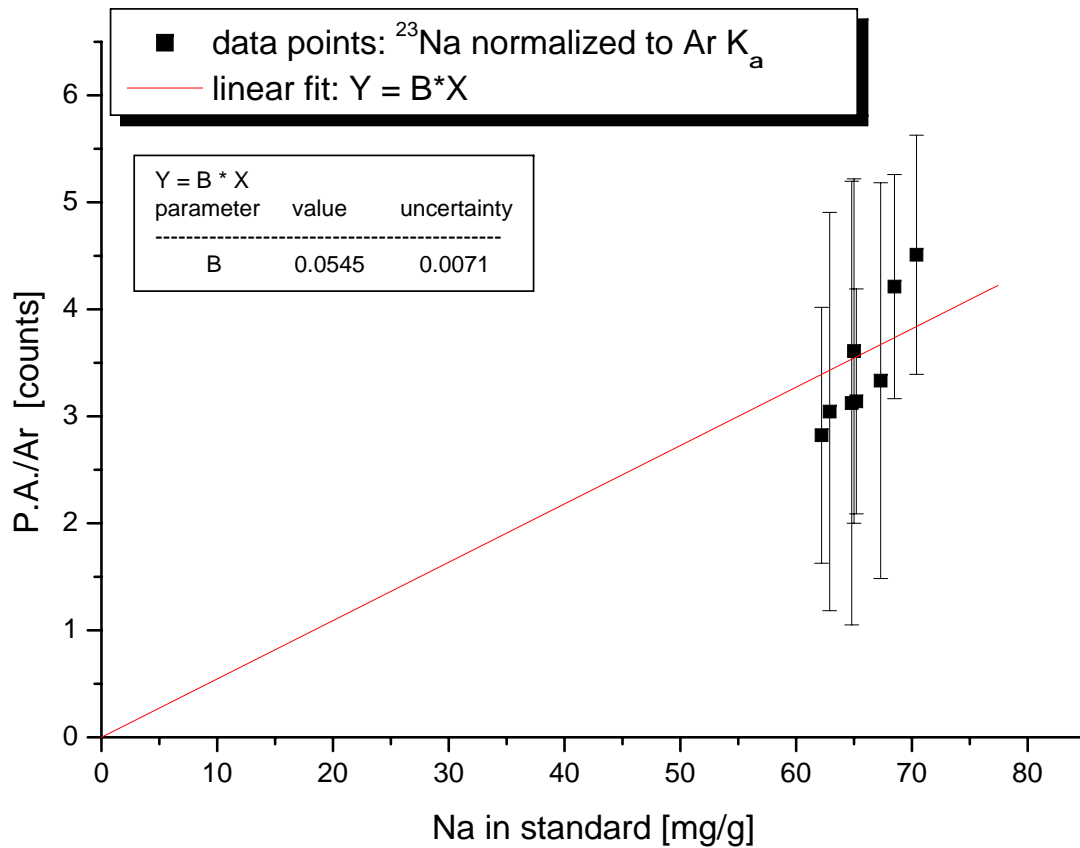


Figure 6.8.: Calibration line for sodium concentrations in glass standards.

6.2.3. Aluminum

Two calibration lines were determined for aluminum. The diagram for the metrological samples is shown in figure 6.9, that for aluminum-iron-mixtures in figure 6.10. The corresponding fit parameters are given in the inserts.

The data points used for evaluation are listed in table 6.8 for metrological target and in table 6.9 for aluminum-iron-mixtures.

The relative uncertainty of the slope in the calibration line is calculated 23% for metrological targets and 13 % for the aluminum-iron-mixtures.

The difference between these uncertainties is due to the amount of aluminum in the analyzed material. While the aluminum concentrations in the iron-mixtures are in the range from about 23 mg/g to 500 mg/g, the maximum concentration in the metrological samples is about 60 mg/g.

The metrological standard NBS 91 is plotted in both diagrams, since the pulverized reference material was pressed into similar target holders and measured in July as well as in August together with the iron-mixtures. The normalized peak area of NBS 91 in July is half of that in August. Nevertheless, it fits in both cases within the uncertainties to the calibration lines. Hence, an accurate evaluation of element content is possible with a calibration line determined during the same tuning.

The NBS 91 standard was not considered in the determination of the calibration line for the aluminum-iron-mixtures.

| no. July | target | concentration [mg/g] | P.A./Ar [counts] |
|-------------|----------|-------------------------|---------------------|
| 2 | NBS 91 | 31.80 | 0.19 ± 0.09 |
| 3 | NBS 91 | 31.80 | 0.11 ± 0.10 |
| 6 | BCR 32 | 2.91 | 0.02 ± 0.05 |
| 7 | BCR 32 | 2.91 | 0.08 ± 0.06 |
| 8 | EZRM 681 | 56.2 | 0.26 ± 0.09 |
| 9 | EZRM 681 | 56.2 | 0.27 ± 0.11 |

Table 6.8.: List of data used for determination of aluminum concentrations in metrological standards.

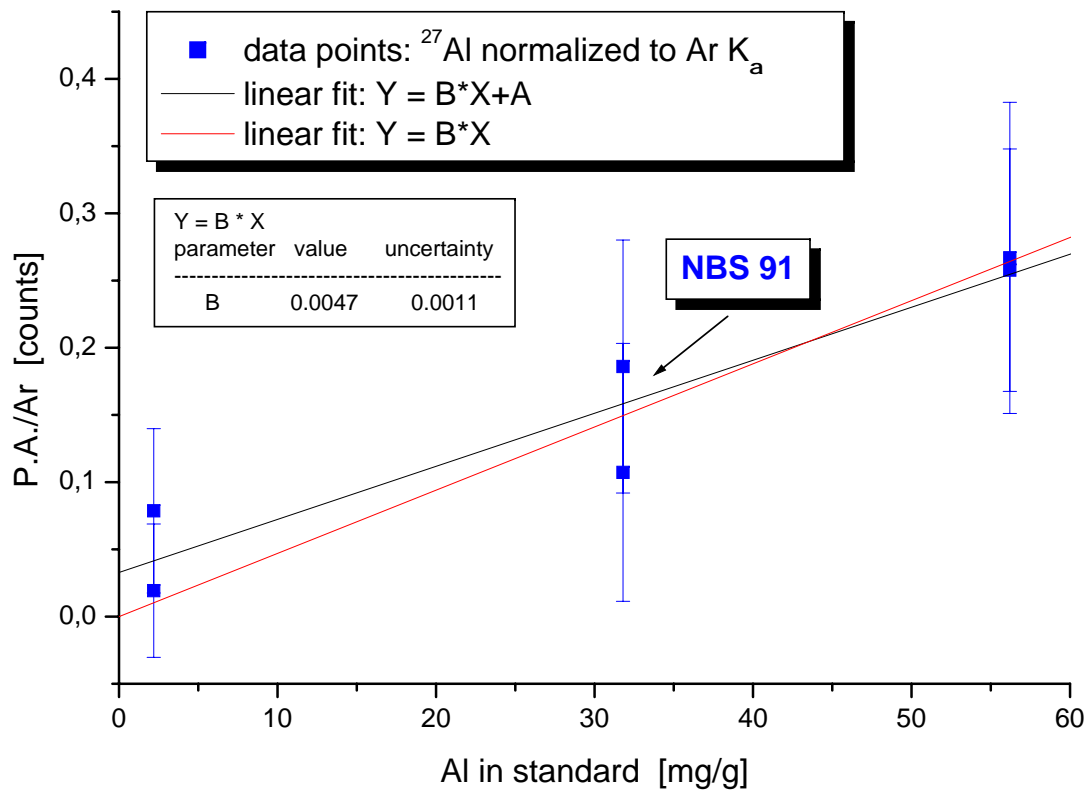


Figure 6.9.: Linear fit and calibration line for aluminum concentrations in metrological samples (July).

6. Experimental Results

| no. August | target | concentration [mg/g] | P.A./Ar [counts] |
|---------------|-------------------------------------|-------------------------|---------------------|
| 13 | 100% Al ₂ O ₃ | 529.25 | 4.06 ±1.00 |
| 14 | 50% Al ₂ O ₃ | 264.66 | 1.77 ±0.38 |
| 15 | 10% Al ₂ O ₃ | 52.44 | 0.63 ±0.19 |
| 16 | 5% Al ₂ O ₃ | 23.82 | 0.20 ±0.10 |
| 8 | NBS 91 | 31.80 | 0.36 ±0.15 |

Table 6.9.: List of data used for determination of aluminum concentrations in glass standards.

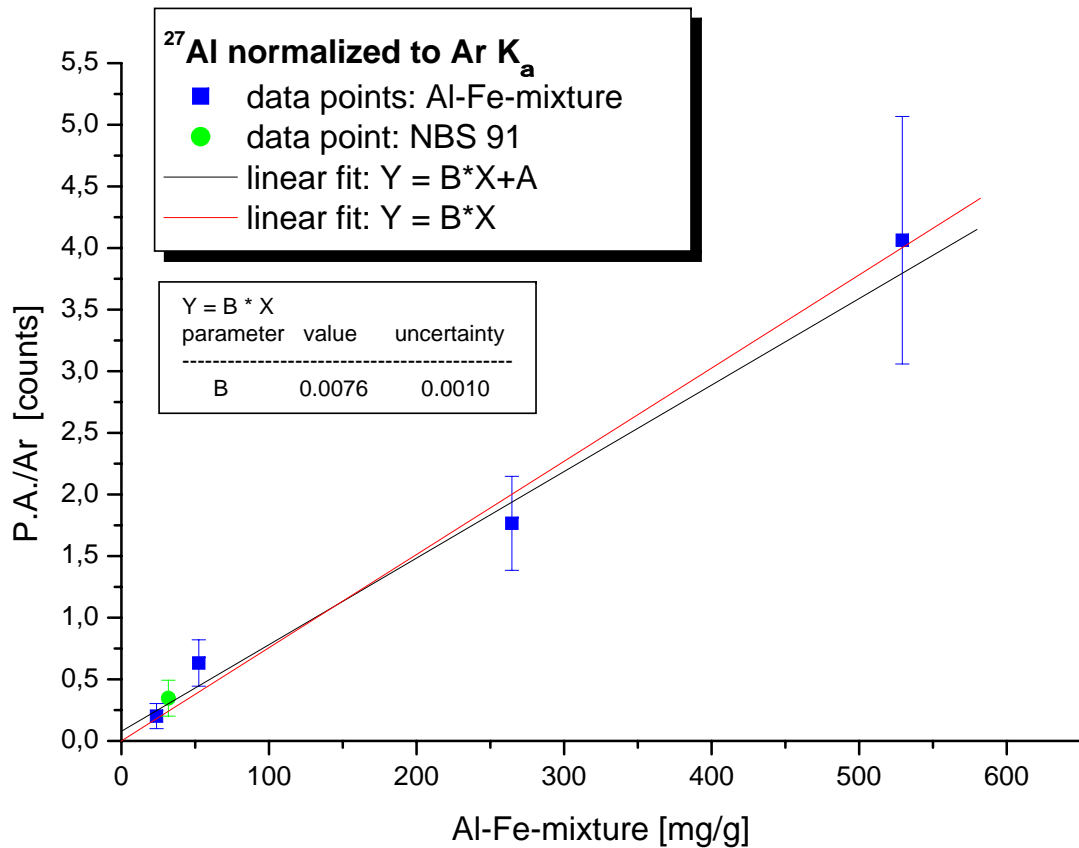


Figure 6.10.: Linear fit and calibration line for aluminum concentrations in aluminum-iron-mixtures (August).

6.2.4. Fluorine

For fluorine the metrological sample data summarized in table 6.10 and of LiF-iron-mixtures listed in table 6.11 were separately fitted. The evaluated calibration lines are shown in figure 6.11 and 6.12, the fit parameter are indicated in the inserts.

Due to the low uncertainties, 6.4 % for metrological standards and 11 % for LiF-iron-mixtures, fluorine comes out to be the best determinable element for PIGE analysis at VERA. A comparison of the NBS 91 standard in both calibration lines provided the same phenomena as for aluminum.

Thus, the calibration line strongly depends on the tuning.

| no. July | target | concentration [mg/g] | P.A./Ar [counts] |
|-------------|----------|-------------------------|---------------------|
| 2 | NBS 91 | 57.30 | 8.18 ± 1.06 |
| 3 | NBS 91 | 57.30 | 7.57 ± 1.02 |
| 6 | BCR 32 | 40.40 | 4.43 ± 0.51 |
| 7 | BCR 32 | 40.40 | 4.32 ± 0.56 |
| 8 | EZRM 681 | 1.94 | 0.15 ± 0.24 |
| 9 | EZRM 681 | 1.94 | 0.06 ± 0.37 |

Table 6.10.: List of data used for determination of fluorine concentrations in metrological standards.

| no. August | target | concentration [mg/g] | P.A./Ar [counts] |
|---------------|----------|-------------------------|---------------------|
| 4 | 100% LiF | 732.40 | 133.67 ± 23.11 |
| 5 | 50% LiF | 365.50 | 74.35 ± 13.39 |
| 6 | 5% LiF | 36.24 | 11.01 ± 3.00 |
| 7 | 1% LiF | 7.29 | 2.66 ± 1.32 |
| 8 | NBS 91 | 57.30 | 10.78 ± 2.26 |

Table 6.11.: List of data used for determination of fluorine concentrations in LiF-iron-mixtures.

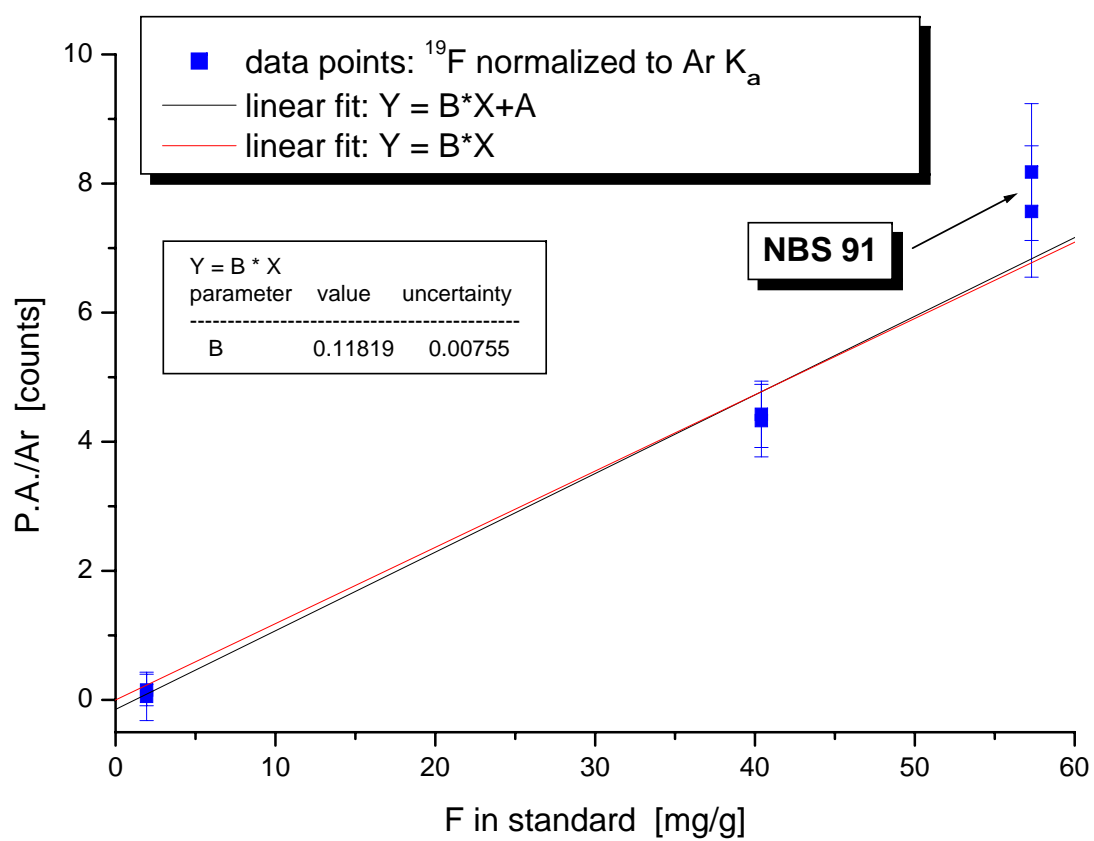


Figure 6.11.: Linear fit and calibration line for fluorine concentrations in metrological samples (July).

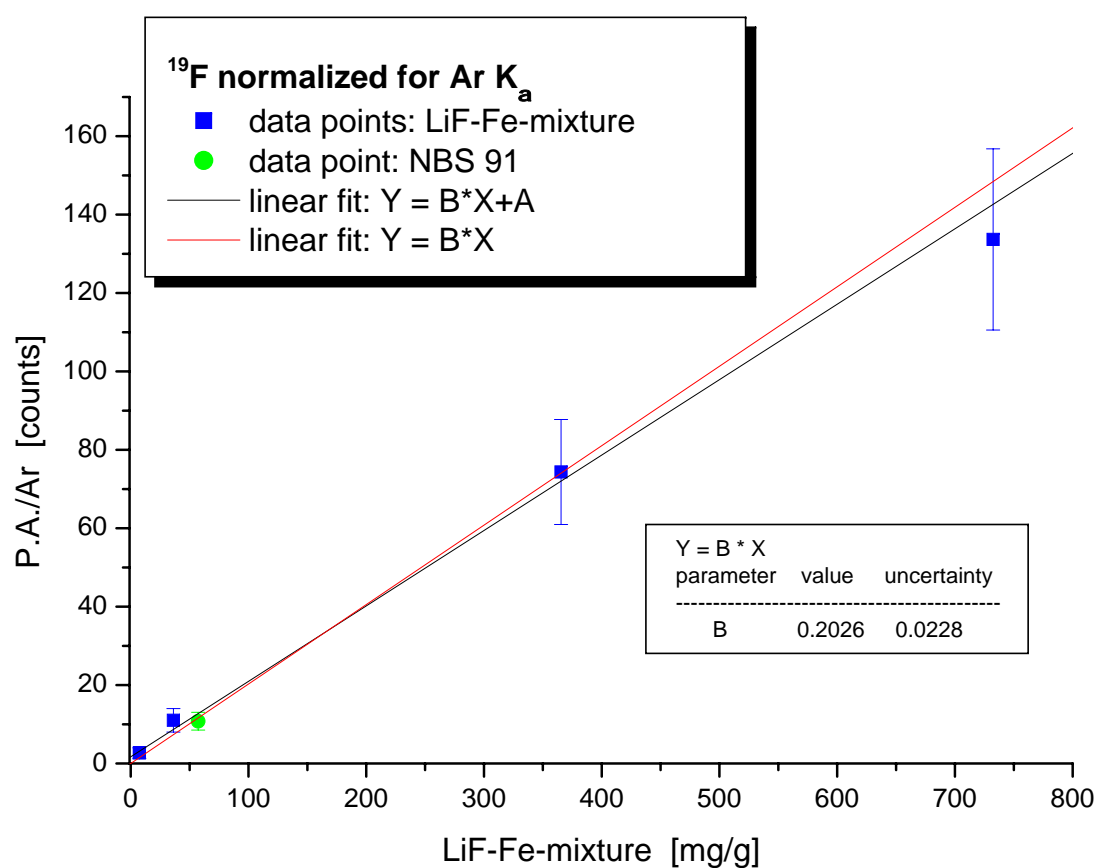


Figure 6.12.: Linear fit and calibration line for fluorine concentrations in LiF-iron-mixtures (August).

6.2.5. Boron

The normalized peak areas were fitted versus the boron concentrations of boron-iron-mixtures to provide a calibration curve for sample containing boron as shown in figure 6.13. The plotted data are summarized in table 6.13, the fit parameters are indicated in the inserts.

The uncertainties of the peak areas are higher than usual. This is partly due to the Doppler broadening of the peak and partly due to the low count rate. The relative uncertainty of 24 % is the biggest uncertainty of all calibration curves.

| no. August | target | concentration [mg/g] | P.A./Ar [counts] |
|---------------|-------------------------------------|-------------------------|---------------------|
| 9 | 100% H ₃ BO ₃ | 174.84 | 1.02 ±0.35 |
| 10 | 60% H ₃ BO ₃ | 107.39 | 0.72 ±0.37 |
| 11 | 10% H ₃ BO ₃ | 52.45 | 0.32 ±0.18 |
| 12 | 6% H ₃ BO ₃ | 10.48 | 0.09 ±0.05 |

Table 6.12.: List of data used for determination of boron concentrations in boron-iron-mixtures.

6.2.6. Lithium

In figure 6.14 the normalized peak areas are plotted versus the lithium concentrations, listed in table 6.13. The fit parameters are given in the inserts.

The relative uncertainty of the calibration line was calculated to be 10 %. Therefore, lithium is, besides fluorine, one of the best quantitatively determinable elements with PIGE at the VERA facility.

| no. August | target | concentration [mg/g] | P.A./Ar [counts] |
|---------------|----------|-------------------------|---------------------|
| 4 | 100% LiF | 267.60 | 49.46 ±8.04 |
| 5 | 500% LiF | 133.54 | 29.16 ±4.95 |
| 6 | 5% LiF | 13.27 | 4.26 ±0.87 |
| 7 | 1% LiF | 2.64 | 1.07 ±0.53 |

Table 6.13.: List of data used for determination of lithium concentrations in LiF-iron-mixtures.

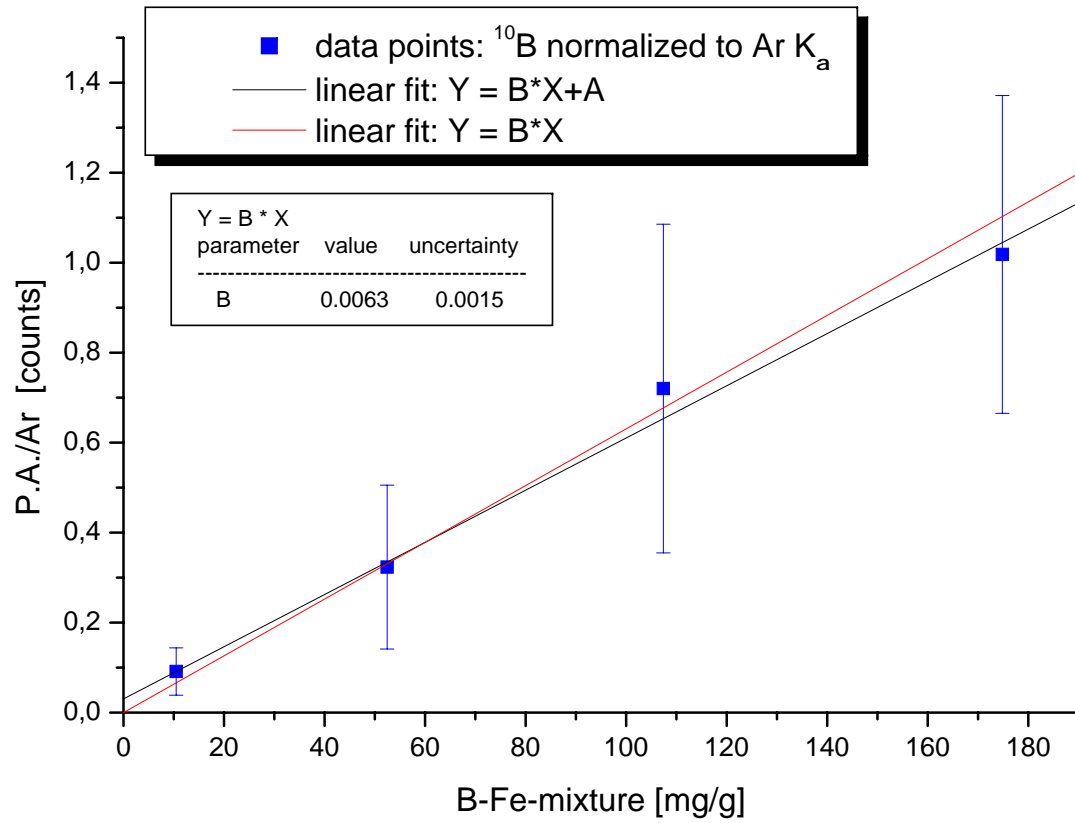


Figure 6.13.: Linear fit and calibration line for boron concentrations in boron-iron-mixtures.

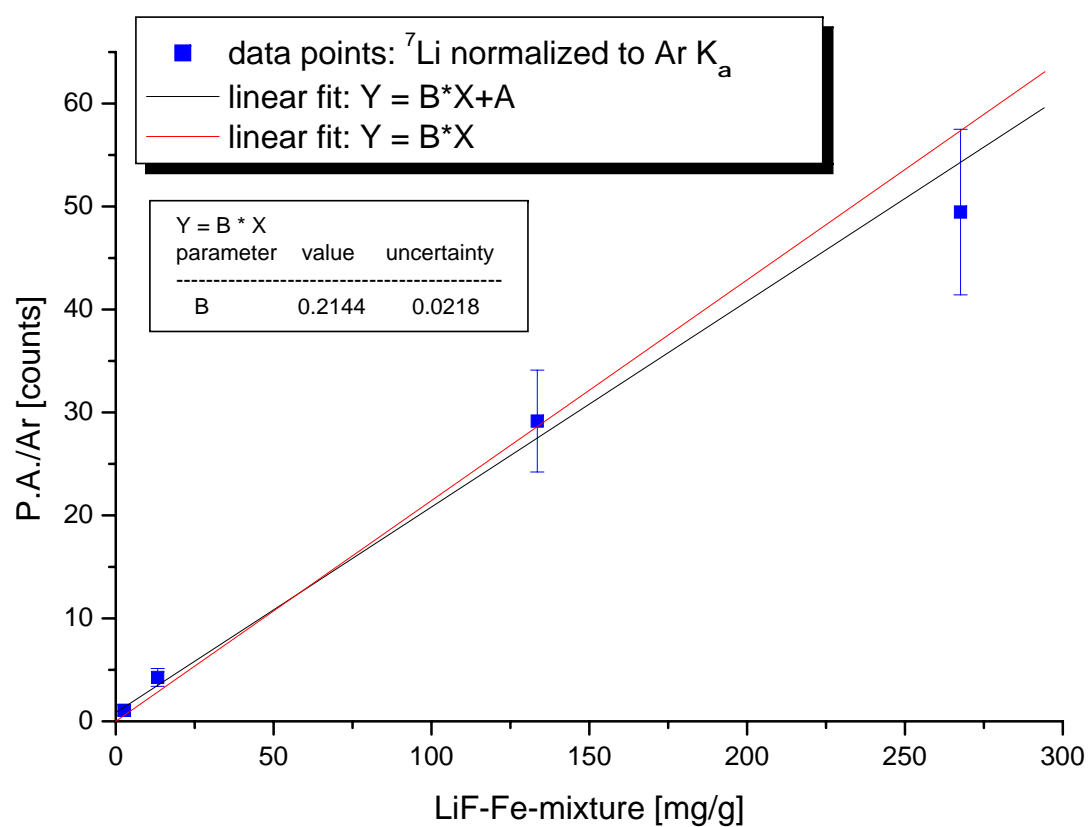


Figure 6.14.: Linear fit and calibration line for lithium concentrations in LiF-iron-mixtures.

7. Conclusion and Outlook

The PIGE analysis of several reference materials of known composition with 3 MeV protons has been performed with the external-beam PIXE-ART setup at VERA.

The main goal was to establish the PIGE application at the VERA facility and the determination of calibration lines for light element concentrations. This is especially important for multi-elemental material ion beam analysis. Since the PIXE method mainly detects heavy elements, the PIGE analysis is an ideal complementary technique to determine light element concentration in target materials. For such samples the PIGE analysis proved to be generally applicable at VERA. Table 7.1 summarizes the results of irradiated samples.

| element | standard | beamtime | concentration [mg/g] | σ_{cali} [%] |
|---------|------------------------------|----------------|----------------------------|------------------------|
| Na | metrological glass | July July | 62.2 - 70.4 3.7 - 41.4 | 13 22.66 |
| Al | metrological iron-mixture | July August | 2.9 - 56.2 23.8 - 529.2 | 23 13.16 |
| F | metrological iron-mixture | July August | 1.9 - 57.3 7.2 - 732.4 | 6.4 11.24 |
| Li | iron-mixture | August | 2.6 - 267.6 | 10 |
| B | iron-mixture | August | 10.4 - 174.8 | 23 |

Table 7.1.: The evaluated uncertainties of the calibration curves, σ_{cali} , for light element concentrations. Beamtimes are classified to July and August tunings.

Even the best lowest uncertainties of 6.4 % (F) and 10 % (Li) with this setup is for many applications still too high.

Despite many improvements, the irradiation conditions apply particularly to the present PIXE-ART setup and the uncertainties are primarily due to the proton induced γ -ray background and the current calibration. A principal problem is the

7. Conclusion and Outlook

current measurement which strongly depends on the experimental constituents, such as Faraday Cup, geometry of PIXE-slits, beam geometry, etc. An approach to solve this problem would be a current measurement shortly before the exit window which would result in a total modification of the PIXE-ART setup.

At VERA, the current was determined by the indirect method of a Ar K_α measurement.

For the determination of light element concentrations (e.g. art objects) in the present setup, an indispensable condition is the determination of calibrations lines of each analyzed element before and after a beamtime sequence. Therefore an amount of suitable standard samples is necessary.

Moreover, with the current setup it might be also worth to try ion beam analysis with higher proton energies.

Appendix

A. Measurement of an iron standard at FZD

As mentioned in chapter 4, our contact in FZD (Forschungszentrum Dresden-Rossendorf), Christian Neelmeijer, gave us the opportunity to examine PIGE spectra accumulated at the IBA facility in Rossendorf.

The experiment was performed with 4 MeV protons, accelerated by a 5 MV Van de Graff Tandem. After penetrating through a 0.2 μm thick Havar foil, the proton beam hit on the sample in 3 mm distance from the exit window of 1 mm diameter.

The γ -ray spectra were collected using a HPGe detector with a nominal efficiency of 60 % (compared with a 3" x 3" NaI detector) for the 1.33 MeV peak of a ^{60}Co source, placed at an angle of 45° to the beam axis.

Irradiation of 4 MeV protons was performed with 200 pA for 300 s.

In figure A.1 the "proton on air" spectrum and the γ -ray spectrum, obtained for an iron standard used as sample, are compared. The intensive γ -ray line at 846.8 keV in the "proton on iron standard" spectrum, verifies our hypothesis of the $^{56}\text{Fe}(\text{n},\text{n}\gamma)^{56}\text{Fe}$ reaction.

Moreover, no proton induced γ -ray lines of ^{19}F , ^{23}Na and ^{27}Al are visible.

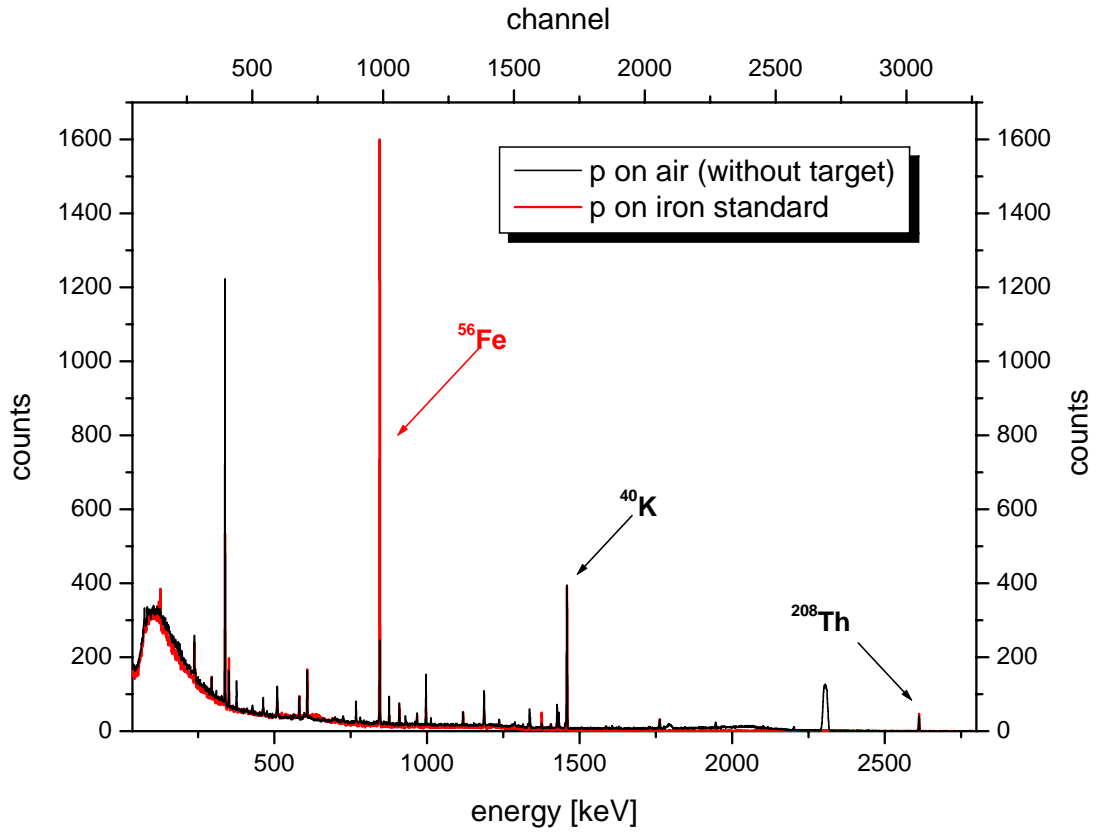


Figure A.1.: Comparison of a "proton on air" spectrum and a γ -ray spectrum of an iron standard, accumulated at the IBA facility in FZD. The intensive line corresponding to 846.8 keV line of the $^{56}\text{Fe}(n,n\gamma)^{56}\text{Fe}$ reaction is labeled red. The black labeled calibration lines of ^{40}K (1460.8 keV) and ^{208}Tl (2614.5 keV) are not visible because they overlap with the "proton on air" spectrum.

B. Determination of the beam width

As shown in figure 2.1 the proton beam expands in air, surrounded by a so called halo.

To determine the size of the H^+ -beam at target position, a $20\ \mu\text{m}$ Au-W-wire was mounted in 1 cm distance to the exit window. The wire was moved from initial point, which is (0/0) in the beam axis, in μm steps horizontal (x) and vertical (y) with the PIXE manipulator. Each position was irradiated 100 s (life time). The produced X-rays Ar K_α (2.96 keV) and W L_α (8.40 keV) were accumulated simultaneously with the Si(Li) detector and an other X-ray detector (Amptek) which replaced the HPGe-detector at same angular position. The decrease of the recorded counts within the peak areas, gave informations about the width of the proton beam.

The X-ray peak areas for both detectors for different horizontal and vertical positions are listed in table B.2 and table B.3 at the end of the chapter. The uncertainty of each peak area is derived from counting statistics.

For current calibration the peak area of W L_α was normalized to Ar K_α counts because proton current measurement at PIXE-ART is not feasible. The evaluated values in for horizontal and vertical wire positions are listed in table B.4 and B.5 at the end of the chapter. The uncertainty of the normalized W L_α peak area, σ_{Wn} , was calculated due to the law of uncertainty propagation. Figure B.1 and B.2 show a bell-shaped decrease of the X-ray intensity with distance to the beam center. Due to a Gaussian fit, the FWHM (full width at half maximum) was calculated, the values are summarized in table B.1.

| | x FWHM [μm] | y FWHM [μm] |
|--------------------------|--------------------------|--------------------------|
| Si(Li) | 149.4 \pm 2.5 | 156.3 \pm 5.2 |
| Amptek | 156.5 \pm 3.1 | 148.2 \pm 2.7 |
| $\overline{\text{FWHM}}$ | 153.0 \pm 3.7 | 152.2 \pm 4.7 |

Table B.1.: FWHM calculated from the fitted Gaussian distributions. The average of both detectors is entered in the last row.

To characterize the beam size, the beam edge is defined by the intensity drops to a tenth. Therefore, the horizontal beam width is calculated to be $288.5 \pm 7.1\ \mu\text{m}$ and the vertical beam width to be $288.7 \pm 8.1\ \mu\text{m}$. Thus, a 3 MeV proton beam, collimated to $150\ \mu\text{m}$, symmetrically expands in 1 cm air to double width.

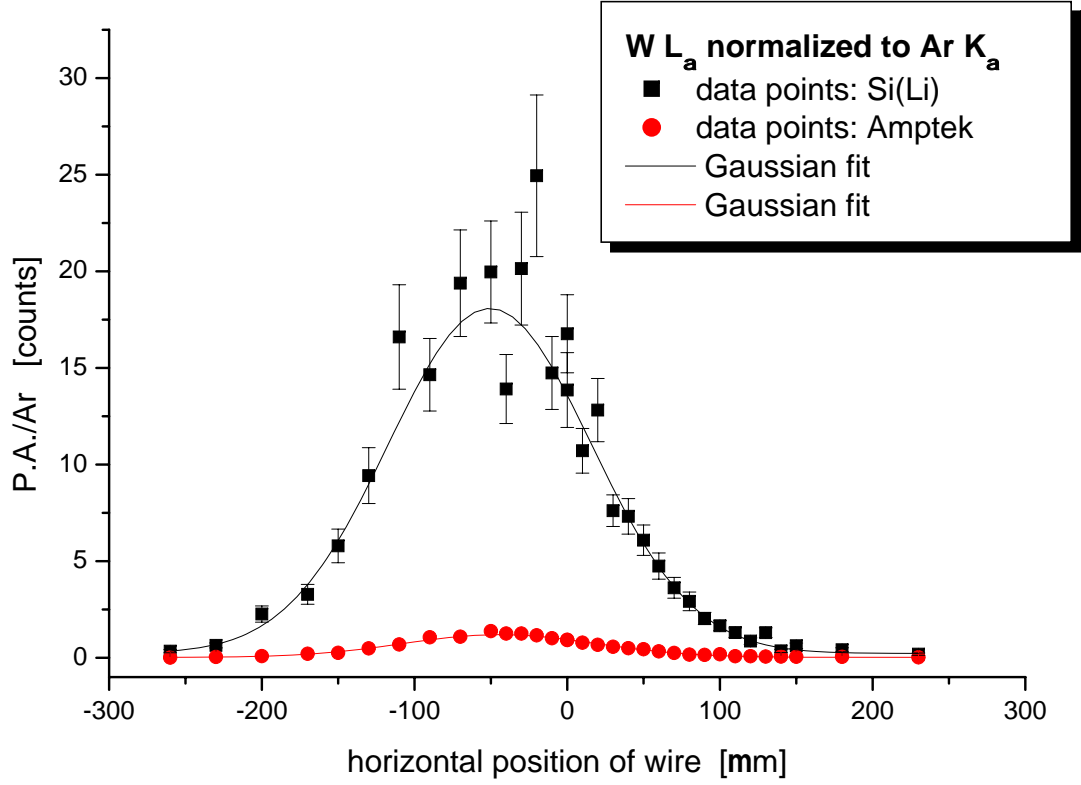


Figure B.1.: Normalized W L_α peak areas plotted as a function of horizontal wire position for both detectors. Data points acquired with the Si(Li) detector are labeled in black, with the Amptek detector in red. The decrease of intensity follows a Gaussian distribution curve with a calculated beam width of 288.5 μm.

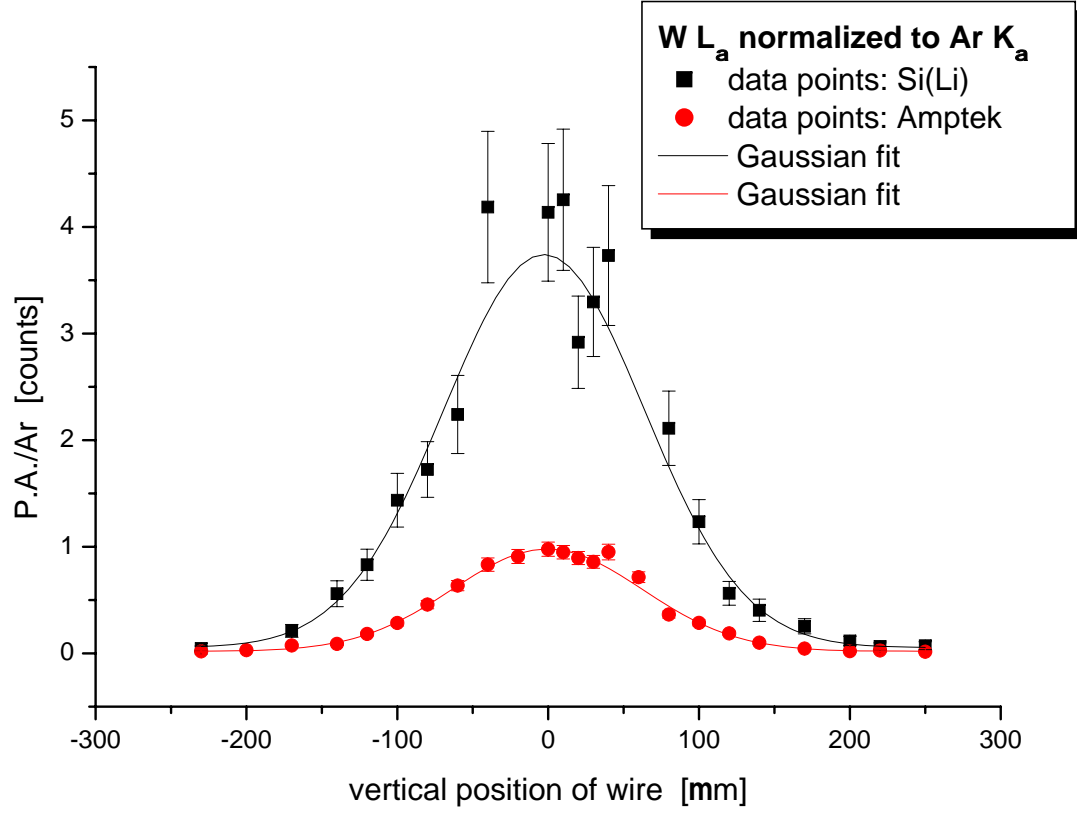


Figure B.2.: Normalized $W L_{\alpha}$ peak areas plotted as a function of vertical wire position for both detectors. Data points acquired with the Si(Li) detector are labeled in black, with the Amptek detector in red. The decrease of intensity follows a Gaussian distribution curve with a calculated beam width of $288.7 \mu\text{m}$.

| | Si(Li) | | | | Amptek | | | |
|-----------------------|---------------------------|---------------------|--------------------------|---------------------|---------------------------|---------------------|--------------------------|---------------------|
| x-pos. [μm] | Ar K_α [counts] | σ_{K_α} | W L_α [counts] | σ_{L_α} | Ar K_α [counts] | σ_{K_α} | W L_α [counts] | σ_{L_α} |
| 0 | 73 | 8.54 | 1224 | 34.99 | 622 | 24.94 | 580 | 24.08 |
| 10 | 94 | 9.70 | 1007 | 31.73 | 588 | 24.25 | 458 | 21.40 |
| 20 | 66 | 8.12 | 846 | 29.09 | 583 | 24.15 | 391 | 19.77 |
| 30 | 98 | 9.90 | 746 | 27.31 | 582 | 24.12 | 332 | 18.22 |
| 40 | 72 | 8.49 | 527 | 22.06 | 575 | 23.98 | 286 | 16.91 |
| 50 | 70 | 8.37 | 426 | 20.64 | 525 | 22.91 | 232 | 15.23 |
| 60 | 59 | 7.68 | 280 | 16.73 | 473 | 21.75 | 156 | 12.49 |
| 70 | 58 | 7.62 | 210 | 14.49 | 388 | 19.70 | 97 | 9.85 |
| 80 | 49 | 7 | 143 | 11.96 | 370 | 19.23 | 60 | 7.75 |
| 90 | 61 | 7.81 | 124 | 11.14 | 410 | 20.25 | 60 | 7.75 |
| 100 | 67 | 8.19 | 111 | 10.54 | 365 | 19.10 | 67 | 8.19 |
| 110 | 50 | 7.07 | 65 | 8.06 | 385 | 19.62 | 31 | 5.57 |
| 120 | 58 | 7.62 | 50 | 7.07 | 381 | 19.52 | 31 | 5.57 |
| 130 | 47 | 6.86 | 61 | 7.81 | 366 | 19.13 | 22 | 4.69 |
| 140 | 65 | 8.06 | 23 | 4.80 | 386 | 19.65 | 23 | 4.80 |
| 150 | 50 | 7.07 | 31 | 5.57 | 371 | 19.26 | 20 | 4.47 |
| 180 | 58 | 7.62 | 24 | 4.90 | 376 | 19.39 | 17 | 4.12 |
| 230 | 69 | 8.31 | 13 | 3.61 | 423 | 20.57 | 9 | 3 |
| 0 | 55 | 7.42 | 762 | 27.60 | 416 | 20.40 | 381 | 19.52 |
| -10 | 65 | 8.06 | 958 | 30.95 | 429 | 20.71 | 435 | 20.86 |
| -20 | 37 | 6.08 | 923 | 30.38 | 388 | 19.70 | 451 | 21.24 |
| -30 | 50 | 7.07 | 1007 | 31.73 | 359 | 18.95 | 451 | 21.24 |
| -40 | 65 | 8.06 | 904 | 30.07 | 325 | 18.03 | 408 | 20.20 |
| -50 | 60 | 7.75 | 1198 | 34.61 | 393 | 19.82 | 543 | 23.30 |
| -70 | 52 | 7.21 | 1008 | 31.75 | 393 | 19.82 | 428 | 20.69 |
| -90 | 65 | 8.06 | 952 | 30.85 | 371 | 19.26 | 394 | 19.85 |
| -110 | 40 | 6.32 | 664 | 25.77 | 392 | 19.80 | 270 | 16.43 |
| -130 | 47 | 6.86 | 443 | 21.05 | 353 | 18.79 | 172 | 13.11 |
| -150 | 52 | 7.21 | 301 | 17.35 | 388 | 19.70 | 98 | 9.90 |
| -170 | 53 | 7.28 | 174 | 13.19 | 370 | 19.24 | 77 | 8.77 |
| -200 | 42 | 6.48 | 95 | 9.75 | 397 | 19.92 | 34 | 5.83 |
| -230 | 64 | 8 | 41 | 6.40 | 394 | 19.85 | 17 | 4.12 |
| -260 | 70 | 8.37 | 24 | 4.90 | 363 | 19.05 | 3 | 1.73 |

Table B.2.: Acquired Ar K_α and W L_α X-rays at different horizontal wire positions.

| | Si(Li) | | | | Amptek | | | |
|-----------------------|---------------------------|---------------------|--------------------------|---------------------|---------------------------|---------------------|--------------------------|---------------------|
| y-pos. [μm] | Ar K_α [counts] | σ_{K_α} | W L_α [counts] | σ_{L_α} | Ar K_α [counts] | σ_{K_α} | W L_α [counts] | σ_{L_α} |
| 250 | 56 | 7.48 | 4 | 2 | 456 | 21.35 | 7 | 2.65 |
| 220 | 62 | 7.87 | 4 | 2 | 479 | 21.89 | 13 | 3.61 |
| 200 | 69 | 8.31 | 8 | 2.83 | 445 | 21.10 | 9 | 3 |
| 170 | 63 | 7.94 | 16 | 4 | 514 | 22.67 | 23 | 4.80 |
| 140 | 52 | 7.21 | 21 | 4.58 | 469 | 21.66 | 47 | 6.86 |
| 120 | 71 | 8.43 | 40 | 6.32 | 480 | 21.91 | 90 | 9.49 |
| 100 | 64 | 8 | 79 | 8.89 | 479 | 21.89 | 137 | 11.70 |
| 80 | 54 | 7.35 | 114 | 10.68 | 478 | 21.86 | 174 | 13.19 |
| 60 | - | 0 | - | 0 | 483 | 21.98 | 345 | 18.57 |
| 40 | 41 | 6.40 | 153 | 12.37 | 343 | 18.52 | 326 | 18.06 |
| 30 | 54 | 7.35 | 178 | 13.34 | 444 | 21.07 | 381 | 19.52 |
| 20 | 61 | 7.81 | 178 | 13.34 | 444 | 21.07 | 397 | 19.92 |
| 10 | 51 | 7.14 | 217 | 14.73 | 466 | 21.59 | 442 | 21.02 |
| 0 | 51 | 7.14 | 211 | 14.53 | 437 | 20.90 | 427 | 20.66 |
| -20 | - | 0 | - | 0 | 406 | 20.15 | 369 | 19.21 |
| -40 | 43 | 6.56 | 180 | 13.42 | 388 | 19.70 | 323 | 17.97 |
| -60 | 54 | 7.35 | 121 | 11 | 447 | 21.14 | 284 | 16.85 |
| -80 | 69 | 8.31 | 119 | 10.91 | 435 | 20.86 | 199 | 14.12 |
| -100 | 55 | 7.42 | 79 | 8.89 | 499 | 22.34 | 142 | 11.92 |
| -120 | 71 | 8.43 | 59 | 7.68 | 610 | 24.70 | 111 | 10.54 |
| -140 | 59 | 7.68 | 33 | 5.74 | 641 | 25.32 | 57 | 7.55 |
| -170 | 71 | 8.43 | 15 | 3.87 | 513 | 22.65 | 38 | 6.16 |
| -200 | - | 0 | - | 0 | 567 | 23.81 | 17 | 4.12 |
| -230 | 88 | 9.38 | 4 | 2 | 651 | 25.51 | 12 | 3.46 |

Table B.3.: Acquired Ar K_α and W L_α X-rays at different vertical wire positions.

| | Si(Li) | | Amptek | |
|----------------------|---|---------------|---|---------------|
| x-pos [μm] | W L_α /Ar K_α [counts] | σ_{Wn} | W L_α /Ar K_α [counts] | σ_{Wn} |
| 0 | 16.77 | 2.02 | 0.93 | 0.05 |
| 10 | 10.71 | 1.16 | 0.78 | 0.05 |
| 20 | 12.82 | 1.64 | 0.67 | 0.04 |
| 30 | 7.61 | 0.82 | 0.57 | 0.04 |
| 40 | 7.32 | 0.92 | 0.50 | 0.04 |
| 50 | 6.09 | 0.78 | 0.44 | 0.03 |
| 60 | 4.75 | 0.68 | 0.33 | 0.03 |
| 70 | 3.62 | 0.54 | 0.25 | 0.03 |
| 80 | 2.92 | 0.48 | 0.16 | 0.02 |
| 90 | 2.03 | 0.32 | 0.15 | 0.02 |
| 100 | 1.66 | 0.26 | 0.18 | 0.02 |
| 110 | 1.30 | 0.24 | 0.08 | 0.02 |
| 120 | 0.86 | 0.17 | 0.08 | 0.02 |
| 130 | 1.30 | 0.25 | 0.06 | 0.01 |
| 140 | 0.35 | 0.09 | 0.06 | 0.01 |
| 150 | 0.62 | 0.14 | 0.05 | 0.01 |
| 180 | 0.43 | 0.10 | 0.05 | 0.01 |
| 230 | 0.19 | 0.06 | 0.02 | 0.01 |
| 0 | 13.85 | 1.93 | 0.92 | 0.06 |
| -10 | 14.74 | 1.89 | 1.01 | 0.07 |
| -20 | 24.95 | 4.18 | 1.16 | 0.08 |
| -30 | 20.14 | 2.92 | 1.26 | 0.09 |
| -40 | 13.91 | 1.79 | 1.26 | 0.09 |
| -50 | 19.97 | 2.64 | 1.38 | 0.09 |
| -70 | 19.38 | 2.76 | 1.09 | 0.08 |
| -90 | 14.65 | 1.88 | 1.06 | 0.08 |
| -110 | 16.60 | 2.70 | 0.69 | 0.05 |
| -130 | 9.43 | 1.44 | 0.49 | 0.05 |
| -150 | 5.79 | 0.87 | 0.25 | 0.03 |
| -170 | 3.28 | 0.52 | 0.21 | 0.03 |
| -200 | 2.26 | 0.42 | 0.09 | 0.02 |
| -230 | 0.64 | 0.13 | 0.04 | 0.01 |
| -260 | 0.34 | 0.08 | 0.01 | 0.01 |

Table B.4.: To Ar K_α normalized W L_α peak area for horizontal wire position.

| | Si(Li) | | Amptek | |
|----------------------|---|---------------|---|---------------|
| y-pos [μm] | W L $_{\alpha}$ /Ar K $_{\alpha}$ [counts] | σ_{Wn} | W L $_{\alpha}$ /Ar K $_{\alpha}$ [counts] | σ_{Wn} |
| 250 | 0.07 | 0.04 | 0.02 | 0.01 |
| 220 | 0.06 | 0.03 | 0.03 | 0.01 |
| 200 | 0.12 | 0.04 | 0.02 | 0.01 |
| 170 | 0.25 | 0.07 | 0.04 | 0.01 |
| 140 | 0.40 | 0.10 | 0.10 | 0.02 |
| 120 | 0.56 | 0.11 | 0.19 | 0.02 |
| 100 | 1.23 | 0.21 | 0.29 | 0.03 |
| 80 | 2.11 | 0.35 | 0.36 | 0.03 |
| 60 | - | - | 0.71 | 0.05 |
| 40 | 3.73 | 0.66 | 0.95 | 0.07 |
| 30 | 3.30 | 0.51 | 0.86 | 0.06 |
| 20 | 2.92 | 0.43 | 0.89 | 0.06 |
| 10 | 4.25 | 0.66 | 0.95 | 0.06 |
| 0 | 4.14 | 0.65 | 0.98 | 0.07 |
| -20 | - | - | 0.91 | 0.07 |
| -40 | 4.19 | 0.71 | 0.83 | 0.06 |
| -60 | 2.24 | 0.37 | 0.64 | 0.05 |
| -80 | 1.72 | 0.26 | 0.46 | 0.04 |
| -100 | 1.44 | 0.25 | 0.28 | 0.03 |
| -120 | 0.83 | 0.15 | 0.18 | 0.02 |
| -140 | 0.56 | 0.12 | 0.09 | 0.01 |
| -170 | 0.21 | 0.06 | 0.07 | 0.01 |
| -200 | - | - | 0.03 | 0.01 |
| -230 | 0.05 | 0.02 | 0.02 | 0.01 |

Table B.5.: To Ar K $_{\alpha}$ normalized W L $_{\alpha}$ peak area for vertical wire position.

C. Chemical composition of standards used for evaluation

In the following the five included data sheets from M. Schreiner and Silke Merchel are shown.

| | NIST SRM | | | | Danone | | | |
|------------------------------------|----------|-------|-------|-------|--------|-------|-------|-------|
| | 610** | 620 | 1830 | 1831 | N1 | N2 | N3 | N4 |
| Na₂O₃ | 14,0* | 14,39 | 13,75 | 13,32 | 13,28 | 13,25 | 12,71 | 12,85 |
| MgO | | 3,69 | 3,9 | 3,51 | 1,23 | 0,75 | 1,14 | 1,44 |
| Al₂O₃ | 2,0* | 1,8 | 0,12 | 1,21 | 1,53 | 2,15 | 1,57 | 1,23 |
| SiO₂ | 72,0* | 72,08 | 73,07 | 73,08 | 72,4 | 71,1 | 72,1 | 71,8 |
| SO₃ | | 0,28 | 0,26 | 0,25 | 0,152 | 0,077 | 0,056 | 0,033 |
| K₂O | 0,0555* | 0,41 | 0,04 | 0,33 | 0,29 | 1,14 | 0,54 | 0,42 |
| CaO | 12,0* | 7,11 | 8,56 | 8,2 | 10,92 | 11,11 | 10,98 | 11,77 |
| TiO₂ | 0,062* | 0,018 | 0,01 | 0,019 | 0,01 | 0,068 | 0,046 | 0,038 |
| Cr₂O₃ | | | | | | 0,016 | 0,212 | 0,068 |
| MnO | 0,0626 | | | | 0,003 | 0,025 | 0,024 | 0,02 |
| Fe₂O₃ | 0,0655 | 0,043 | 0,121 | 0,087 | 0,047 | 0,178 | 0,462 | 0,167 |
| NiO | 0,0584 | | | | 0,001 | 0,001 | 0,004 | 0,002 |
| CoO | 0,0496* | | | | | | | |
| CuO | 0,0556* | | | | | | | |
| ZnO | 0,0539* | | | | | | | |
| As₂O₃ | | 0,056 | | | | | | |
| RbO | 0,0506 | | | | | | | |
| SrO | 0,0610 | | | | | | | |
| BaO | | | | | 0,001 | 0,02 | 0,034 | 0,029 |
| PbO | 0,0280 | | | | 0,002 | 0,005 | 0,018 | 0,016 |

Figure C.1.: Included data sheet from M. Schreiner. The chemical composition of glass standards in mass percentage (w%) is indicated.

Not certified values are labeled "**".

Certified element concentrations are indicated as oxides and labeled "***".

BCR-CRM 038

Fly Ash

Unit size: 5g

Producer: BCR

Min. Wt.:

Certifying Body: Institute for Reference Materials and Measurements

Unit Price: Euro140 Date Issued:

Values are quoted as mg/kg unless noted in column "Remarks".

| MEASURAND | VALUE TYPE | VALUE | ASS. UNC. [%] | REMARKS |
|-----------|------------|-------|---------------|---------|
| As | C | 48 | 5 | |
| Cd | C | 4.6 | 6 | |
| Co | C | 53.8 | 4 | |
| Cu | C | 176 | 5 | |
| Fe | C | 33800 | 2 | |
| Hg | C | 2.1 | 7 | |
| Mn | C | 479 | 3 | |
| Na | C | 3740 | 4 | |
| Pb | C | 262 | 4 | |
| Zn | C | 581 | 6 | |
| Cr | N | 178 | | |
| Ni | N | 194 | | |
| Th | N | 17.3 | | |
| V | N | 334 | | |

Figure C.2.: Included data sheet from Silke Merchel. The certified composition of fly ash, BCR 038 is indicated.

Certified element concentrations were indicated "C" in column "value type". Not certified element concentrations were indicated "N" in column "value type".

BCR-CRM 032**Natural Moroccan Phosphate Rock**

Unit size: 100g Producer: BCR
 Min. Wt.: Certifying Institute for Reference Materials and
 body: Measurements
 Unit price: Euro170 Date issued:

Values are quoted as mg/kg unless noted in column "Remarks".

| Measurand | Value type | Value | Ass. unc. [%] | Remarks |
|---------------|------------|--------|---------------|---------|
| Al, oxide | C | 5500 | 11 | |
| As | C | 9.5 | 5 | |
| B | C | 22.6 | 10 | |
| C, dioxide | C | 51000 | 2 | |
| Ca, oxide | C | 517600 | 1 | |
| Cd | C | 20.8 | 3 | |
| Co | C | 0.59 | 10 | |
| Cr | C | 257 | 6 | |
| Cu | C | 33.7 | 4 | |
| F | C | 40400 | 1 | |
| Fe(III) oxide | C | 2300 | 4 | |
| Hg | C | 0.055 | 20 | |
| Mg, oxide | C | 4000 | 3 | |
| Mn | C | 18.8 | 7 | |
| Ni | C | 34.6 | 5 | |
| P, pentoxide | C | 329800 | 1 | |
| S, trioxide | C | 18400 | 4 | |
| Si, dioxide | C | 20900 | 6 | |
| Ti | C | 171 | 6 | |
| V | C | 153 | 5 | |
| Zn | C | 253 | 2 | |

Figure C.3.: Included data sheet from Silke Merchel. The certified composition of natural Moroccan phosphate rock, BCR 032 is tabulated. Certified element concentrations were indicated "C" in column "value type".

NISTSRM91 (opal glass, powder) [National Institute of Standards and Technology,
100 Bureau Drive, Gaithersburg, MD 20899, USA]

| | |
|------------------------------------|--------------------------------------|
| Al ₂ O ₃ | 6.01 %m/m compiled |
| As ₂ O ₃ | 0.09 %m/m compiled |
| As ₂ O ₅ | 0.1 %m/m compiled |
| CaO | 10.49 %m/m compiled |
| Cl | 150 µg/g compiled |
| F | 57300 - 57300 µg/g 2 values compiled |
| Fe ₂ O ₃ | 0.079 %m/m compiled |
| Fe ₂ O ₃ (t) | 0.079 %m/m compiled |
| K ₂ O | 3.24 %m/m compiled |
| MgO | ()0.008 %m/m , uncertain compiled |
| MnO | ()0.008 %m/m , uncertain compiled |
| Na ₂ O | 8.47 %m/m compiled |
| P ₂ O ₅ | 0.023 %m/m compiled |
| Pb | 928 µg/g compiled |
| PbO | 0.1 %m/m compiled |
| SiO ₂ | 67.5 %m/m compiled |
| TiO ₂ | 0.019 %m/m compiled |
| Zn | 643 µg/g compiled |
| ZnO | 0.08 %m/m compiled |
| Zr | 67 µg/g compiled |
| ZrO ₂ | 0.009 %m/m compiled |

Figure C.4.: Included data sheet from Silke Merchel. The chemical composition of opal glass, NBS 91 is listed.

| ZRM-Nr. | B 681-1* |
|------------------------------------|---------------|
| Material | Eisenerz |
| Fe_{gesamt} | 33,21 ± 0,13 |
| Fe(II) | — |
| Fe_{met} | — |
| Si | 8,32 ± 0,08 |
| SiO₂ | 17,79 |
| Al | 5,62 ± 0,10 |
| Al₂O₃ | 10,61 |
| Ca | 2,80 ± 0,10 |
| CaO | 3,92 |
| Mg | 0,89 ± 0,02 |
| MgO | 1,47 |
| Mn | 0,22 ± 0,01 |
| MnO | 0,29 |
| P | 0,88 ± 0,02 |
| P₂O₅ | 2,01 |
| S | 0,103 ± 0,006 |
| Na | 0,068 ± 0,008 |
| Na₂O | 0,092 |
| K | 0,49 ± 0,01 |
| K₂O | 0,59 |
| Cl | — |
| As | (0,0109) |
| C | 1,80 ± 0,04 |
| Co | — |
| Cr | 0,041 ± 0,002 |
| Cr₂O₃ | 0,060 |
| Cu | — |
| F | 0,19 ± 0,01 |
| Mo | — |
| Ni | 0,016 ± 0,001 |
| Pb | (0,0072) |
| Sn | — |
| Ti | 0,29 ± 0,01 |
| TiO₂ | 0,48 |
| V | 0,077 ± 0,004 |
| V₂O₅ | 0,138 |
| Zn | — |

Figure C.5.: Included data sheet from Silke Merchel. The certified composition of iron ore, EZRM 681 is listed. Values in bracket are not certified.

D. Natural decay series

In the three illustrations below, the three natural decay series: ^{232}Th , ^{238}U and ^{235}U are shown.

| Thorium series ($A = 4n$) | | | | | | | | | | | | |
|-----------------------------|---|---|--|--|-----------------------------|--|-----------------------------|--|--|--|----------------------------|--|
| | | | | | | | | | ^{228}Ra 5.75y \rightarrow | 100% $\leftarrow \alpha$ | ^{232}Th 14E9y | |
| | | | | | | | | | | ^{228}Ac 6.13h \rightarrow | | |
| | | ^{212}Pb 10.6h \rightarrow | 100% $\leftarrow \alpha$ | ^{216}Po 0.15s $\leftarrow \alpha$ | 100% $\leftarrow \alpha$ | ^{220}Rn 55.6s $\leftarrow \alpha$ | 100% $\leftarrow \alpha$ | ^{224}Ra 3.66d $\leftarrow \alpha$ | 100% $\leftarrow \alpha$ | ^{228}Th 1.91y | | |
| | ^{208}Tl 3.1m \rightarrow | 36.2% $\leftarrow \alpha$ | ^{212}Bi 60.6m \rightarrow | | | | | | | | | |
| | | ^{208}Pb stable $\leftarrow \alpha$ | 100% $\leftarrow \alpha$ | ^{212}Po 0.3E-6s | | | | | | | | |

Figure D.1.: Thorium series

| Uranium series ($A = 4n + 2$) | | | | | | | | | | | | |
|--|--|---|--|--|-----------------------------|---|-----------------------------|--|-----------------------------|---|--|----------------------------|
| | | | | | | | | | | ^{234}Th 24.1d \rightarrow | 100% $\leftarrow \alpha$ | ^{238}U 4.5E9y |
| | | | | | | | | | | | ^{234}Pa 1.2m+ \rightarrow | |
| | | ^{214}Pb 26.8m \rightarrow | 99.98% $\leftarrow \alpha$ | ^{218}Po 3.05m \rightarrow | 100% $\leftarrow \alpha$ | ^{222}Rn 3.825d $\leftarrow \alpha$ | 100% $\leftarrow \alpha$ | ^{226}Ra 1600y $\leftarrow \alpha$ | 100% $\leftarrow \alpha$ | ^{230}Th 7.5E4y $\leftarrow \alpha$ | 100% $\leftarrow \alpha$ | ^{234}U 2.5E5y |
| | ^{210}Tl 1.30m \rightarrow | 0.4% $\leftarrow \alpha$ | ^{214}Bi 19.9m \rightarrow | 100% $\leftarrow \alpha$ | ^{218}At 2s | | | | | | | |
| ^{206}Hg 8.15m \rightarrow | 75E-6% $\leftarrow \alpha$ | ^{210}Pb 22.3y \rightarrow | 100% $\leftarrow \alpha$ | ^{214}Po 0.16ms | | | | | | | | |
| | ^{206}Tl 4.2m \rightarrow | 5E-5% $\leftarrow \alpha$ | ^{210}Bi 5.0d \rightarrow | | | | | | | | | |
| | | ^{206}Pb stable $\leftarrow \alpha$ | 100% $\leftarrow \alpha$ | ^{210}Po 138.4d | | | | | | | | |

Figure D.2.: Uranium-Radium series

| Actinium series ($A = 4n + 3$) | | | | | | | | | | ^{231}Th 25.5h \rightarrow | 100% $\leftarrow \alpha$ | ^{235}U 7E8y |
|----------------------------------|---|--|--|--|---|------------------------------|--|-----------------------------|--|--|-----------------------------|--------------------------|
| | | | ^{215}Bi 7.4m \rightarrow | 97% $\leftarrow \alpha$ | ^{219}At 0.9m \rightarrow | 4E-3% $\leftarrow \alpha$ | ^{223}Fr 21.8m \rightarrow | 1.2% $\leftarrow \alpha$ | ^{227}Ac 21.8y \rightarrow | 100% $\leftarrow \alpha$ | ^{231}Pa 3.3E4y | |
| | | ^{211}Pb 36.1m \rightarrow | >99.9% $\leftarrow \alpha$ | ^{215}Po 1.8ms \rightarrow | 100% $\leftarrow \alpha$ | ^{219}Rn 3.96s | 100% $\leftarrow \alpha$ | ^{223}Ra 11.4d | 100% $\leftarrow \alpha$ | ^{227}Th 18.7d | | |
| | ^{207}Tl 4.8m \rightarrow | 99.68% $\leftarrow \alpha$ | ^{211}Bi 2.13m \rightarrow | 100% $\leftarrow \alpha$ | ^{215}At 0.1ms | | | | | | | |
| | | ^{207}Pb stable | 100% $\leftarrow \alpha$ | ^{211}Po 0.52s | | | | | | | | |

Figure D.3.: Actinium series

Bibliography

- F. Calastrini, P. Del Carmine, F. Lucarelli, P. Mandò, P. Prati, and A. Zucchiatti. External-beam PIGE for fluorine determination in atmospheric aerosol. *Nuclear Instruments and Methods in Physics Research B.*, 136-138:975–980, 1998. 4
- S. F.G. Perey, Simakov, S. Xia-Min, Y. Kozyr, and B. T.W. Inelastic cross section for ^{56}Fe . *Database for experimental nuclear reaction data (EXFOR) Version of September 09, 2008*, 2008. URL <http://www-nds.iaea.org/exfor>. 24
- R. Firestone, V. S. S. (Editor), S. F. C. C.-R. Editor), C. M. Baglin, and J. Z. A. Editors). *Table of isotopes-CD ROM Edition*. 1996. 25
- R. Golser. Fundamental aspects of ion electron interactions. *Application of Particles and Laser Beams in Material*, pages 1–20, 1995. 3
- IAEA. Experimental nuclear reaction data (EXFOR). database for experimental nuclear reaction data, September 09 2008. URL <http://www-nds.iaea.org/exfor>. 24
- IAEA. *Update of X Ray and Gamma Ray Decay Data Standards for Detector Calibration and Other Applications (Volume 1)*. International Atomic Energy Agency (IAEA), 2007. 37
- B. W. Klaus Bethge, Gertrude Walter. *Kernphysik*. Springer Publishing Company, Heidelberg, second edition, 2001. 6
- W. Kutschera, P. Collon, H. Friedmann, R. Golser, P. Hille, A. Priller, W. Rom, P. Steier, S. Tagesen, A. Wallner, E.-M. Wild, and G. Winkler. Vera: A new AMS facility in Vienna. *Nuclear Instruments and Methods in Physics Research B*, 123: 47–50, 1997. 13
- K. Makino and M. Berz. COSY infinity version 9.0. *Nuclear Instruments and Methods in Physics Research A.*, 558:346–350, 2006. 27
- P. Milota, I. Reiche, O. Duval, A. Oliver Forstner, H. Guicharnaud, W. Walter Kutschera, S. Merchel, A. Priller, M. Schreiner, P. Steier, E. Thobois, A. Wallner, and R. Wünschek, B. Golser. PIXE measurements of renaissance silverpoint drawings at VERA. *Nuclear Instruments and Methods in Physics Research B.*, 266:2279–2285, 2008. 15

- N. National Nuclear Data Center. Nudat 2.4. nuclear database, March,18 2008. URL <http://www.nndc.bnl.gov/nudat2>. 20
- B. Povh, K. Rith, C. Scholz, and F. Zetsche. *Teilchen und Kerne*. Springer Publishing Company, Heidelberg, sixth edition, 2004. 7
- A. Priller, R. Golser, P. Hille, W. Kutschera, W. Rom, P. Steier, A. Wallner, and E. Wild. First performance test of VERA. *Nuclear Instruments and Methods in Physics Research B.*, 123:193–198, 1997. 13
- P. Steier, R. Golser, W. Kutschera, A. Priller, C. Vockenhuber, and S. Winkler. VERA, an AMS facility for "all" isotopes. *Nuclear Instruments and Methods in Physics Research B.*, 223-224:67–71, 2004. 13
- E. Steinbauer. Fundamentals of ion-solid interactions: atomic collision. *Application of Particles and Laser Beams in Material*, pages 21–36, 1995. 3
- J. Tesmer and M. Nastasi. *Handbook of modern ion beam material analysis*. Materials Research Society, 1995. 11, 23
- H. R. Verma. *Atomic and Nuclear Analytical Methods*. Springer Publishing Company, Heidelberg, 2007. 9
- C. Vockenhuber, I. Ahmad, R. Golser, W. Kutschera, V. Liechtenstein, A. Priller, P. Steier, and S. Winkler. Accelerator mass spectrometry of heavy long-lived radionuclides. *International Journal of Mass Spectrometry*, 223-224:713–732, 2003. 13
- B. Wünschek. A study of proton irradiation of paper to assess its influence on PIXE analysis of art objects. Master's thesis, University of Vienna, 2007.
- M. Ziegler and J. Biersack. Srim-2008.01 - the stopping and range of ions in matter. program package, 2008. URL <http://www.srim.org>. 4

Acknowledgments

First I want to thank Prof. Harry Friedman for giving me the unique opportunity to make my Master thesis at the VERA institut, for his supervision and his patient support.

In addition, I want to express my thanks to Prof. Robin Golser for being "my supervisor in law".

Furthermore I would like to thank:

The whole VERA stuff and working shop for helping me in various situationen.

Christian Neelmeijer (FZD) for the wonderful Dresden excursions and the introduction to an unique IBA facility.

Silke Merchel (FZD) for being our "force carrier".

M. Schreiner (Akadamie der bildenden Künste, Vienna)

The "PIXELinge", especially Lea Reichhart and Philipp Müllner for the great cooperation and for unforgettable beam times

Martin Martschini for giving me a "COSY" introduction.

Many thanks to the $\varphi\alpha\kappa$ (Claudia Lederer, Silvia Pabisch, Gabriele Schätzel, Daniela Wimmer and Barbara Wünschek) for being ...what we are :-).

Above all, I want to thank my parents and my boyfriend Philipp. My mom for being my best friend, my dad for believing in me and making my dreams come true and Philipp for his neverending support.

Curriculum vitae

Name: Fabienne Maria Eder

Date of birth: February 6st, 1984

Place of birth: Oberndorf

Nationality: Austria

Marital status: single

1998-2002: Gymnasium BORG Nonntal, Salzburg

May 2002: Matura *mit ausgezeichnetem Erfolg*

since 2002: Diploma study of *physics* at the University of Vienna

student association representative from 2003-2005

since October 2007: Diploma theses at VERA, Isotopenforschung, Fakultät für Physik, University of Vienna (supervisor: Prof. Harry Friedmann): Development and evaluation of a proton induced gamma emission (PIGE)-setup at VERA

Lebenslauf

Name: Fabienne Maria Eder

Geburtsdatum: 06. Februar 1984

Geburtsort: Oberndorf

Staatsbürgerschaft: Österreich

Familienstand: ledig

1998-2002: Gymnasium BORG Nonntal, Salzburg

Mai 2002: Matura *mit ausgezeichnetem Erfolg*

seit 2002: Studium *Physik Diplom* an der Universität Wien

Studienrichtungsvertreterin von 2003-2005

seit Oktober 2007: Diplomarbeit bei VERA, Isotopenforschung, Fakultät für Physik, Universität Wien (Betreuer: Prof. Harry Friedmann) mit dem Thema: Development and evaluation of a proton induced gamma emission (PIGE)-setup at VERA

